3 1176 00155 1192

NASA CR-159,052

NASA Contractor Report 159052

NASA-CR-159052
19790023050

HELICOPTER HIGH GAIN CONTROL

Thomas B. Cunningham
Edwin C. Nunn

HONEYWELL SYSTEMS AND RESEARCH CENTER
2600 RIDGWAY PARKWAY
MINNEAPOLIS, MN 55413

CONTRACT NAS1–14789

JULY 1979

LIBRARY COPY

OCT 4 1979

LANGLEY RESEARCH CENTER
LIBRARY, NASA
HAMPTON, VIRGINIA

NASA
National Aeronautics and
Space Administration

Langley Research Center
Hampton, Virginia 23665
AC 804 827-3966

NASA CR-159,052

1. Report No.	2. Government Accession No.	3. Recipient's Catalog No.
4. Title and Subtitle Helicopter High Gain Control		5. Report Date July 1979 6. Performing Organization Code
7. Author(s) Thomas B. Cunningham Edwin C. Nunn		8. Performing Organization Report No. 79SRC33 10. Work Unit No.
9. Performing Organization Name and Address Honeywell Systems and Research Center 2600 Ridgway Parkway Minneapolis, Minnesota 55413		11. Contract or Grant No. NAS1-14789 13. Type of Report and Period Covered Final Report
12. Sponsoring Agency Name and Address National Aeronautics and Space Administration Langley Research Center Hampton, Virginia 23665		14. Sponsoring Agency Code
15. Supplementary Notes		

16. Abstract

Realization of high gain control is explored through a design study for the NASA/Army/Boeing Vertol CH-47B helicopter. The plans are designed to obtain the maximum bandwidth possible given the hardware constraints. Extensive modeling of rigid body dynamics, actuators, rotors, and flight control sensors is necessary to derive realistic restraints. Controls are designed with modal control theory to specific bandwidths and closed loop mode shapes. Comparisons are made to an earlier "complementary filter" approach. Bandwidth improvement by removal of limitations is explored, in order to establish new hardware and mechanization options. Results indicate improvements are desired in the pitch axis control system and in the rate gyro sensor noise characteristics in all axes before ultimate benefits can be realized. The benefits of using rotor state feedback are also assessed.

N79-31221 #

17. Key Words (Suggested by Author(s))		18. Distribution Statement
Flight control High gain High bandwidth Rotor modeling	CH-47B actuator modeling Modal control Rotor feedback	Distribution unlimited.

19. Security Classif. (of this report)	20. Security Classif. (of this page)	21. No. of Pages	22. Price*
UNCLASSIFIED	Unclassified	171	

* For sale by the National Technical Information Service, Springfield, Virginia 22151

NASA-C-168 (Rev. 6-71)

CONTENTS

Section		Page
1	INTRODUCTION AND OVERVIEW	1
	Introduction	1
	Benefits	2
	Overview	2
	Modeling	3
	Control Design	4
	Report Organization	6
2	MODELING	7
	Introduction	7
	CH-47B Rigid Body Model	10
	Rigid Body Model Validation	12
	Rotor Models	12
	Rotor Flapping Equations of Motion	20
	Transfer Function Rotor Model	22
	Actuator Models	26
	Sensor Models	26
3	CONTROL DESIGN	33
	Design Objectives	33
	Benefits	33
	Specific Design Goals	34
	Modal Control Design Approach	35
	Compensation	36
	Notch Filters	36
	Complementary Filtering	37
	Proportion Plus Integral Control	37
	Feedback Control Design Verification	39
	Pitch Axis Design Results	39
	Pitch Angle--Low Passed Pitch Rate Design	
	Pitch Axis Designs with Unfiltered Feedback	46
	Rotor Feedback	46
	Lateral-Directional Axes Design Results	48
	Langley Complementary Filter	51

CONTENTS (concluded)

Section		Page
3	Filtered Roll Rate Design	55
	Lateral-Direction Design Without Filtering	57
	Rotor Feedback	62
	Gain Scheduling	62
4	SUMMARY AND CONCLUSIONS	66
	Modeling	66
	Control Designs	68
Appendix		
A	ROTOR DYNAMICS	70
B	MODAL CONTROL DESIGN TECHNIQUES	110
C	CH-47 MODEL TESTS	131

LIST OF ILLUSTRATIONS

Figure		Page
1.	NASA/Army/Boeing Vertol CH-47B	11
2.	CH-47B Rigid Body Model, Taken from Reference 2, p. 89	13
3.	CH-47B Open Loop Characteristics	14
4.	Analytical Versus Flight Test Frequency Response (q/δ_B) Hover	15
5.	Analytical Versus Flight Test Frequency Response (p/δ_S) Hover	16
6.	Analytical Versus Flight Test Frequency Response (r/δ_R) Hover	17
7.	Analytical Versus Flight Test Frequency Response (p/δ_S) U_0 = 41.18 m/s (80 kn)	18
8.	Analytical Versus Flight Test Frequency Response (r/δ_R) U_0 = 41.18 m/s (80 kn)	19
9.	Analytical Model Rotor Frequency Response (q/δ_B) Hover	23
10.	Analytical Model Rotor Frequency Response (p/δ_S) Hover	24
11.	Transfer Function Rotor Models	25
12.	CH-47B Actuator Models	27
13.	Hysteresis Model	28
14.	Pitch Rate Spectral Analysis (Hover)	29
15.	Roll Rate Spectral Analysis (Hover)	30
16.	Yaw Rate Spectral Analysis (Hover)	31

LIST OF ILLUSTRATIONS (continued)

Figure		Page
17.	Rate Gyro Sensor Models	32
18.	High Gain Model Following	34
19.	Control Response Design Goals	35
20.	Complementary Filter Logic	38
21.	Pitch Axis Design Goal	40
22.	Pitch Axis Design Results, Low-Pass Filter	42
23.	Pitch Axis Design W_D = 5.0 rad/sec	44
24.	Pitch Axis Design W_D = 7.0 rad/sec	45
25.	Pitch Axis Design Root Locus for Clean Sensors	47
26.	Pitch Axis Rotor Feedback Implementation	49
27.	Pitch Axis Design with Rotor Feedback	50
28.	Langley Complementary Filter[1]	52
29.	Complementary Filter Root Locus Versus W_c	53
30.	Complementary Filter Response to Step δ_R	54
31.	Eigenvalue-Eigenvector Placement Technique	56
32.	Roll Axis Root Locus, Filter Rate Gyros	58
33.	Lateral-Directional Control Laws, Hover Flight Condition	59
34.	Roll Transient Response, Filtered Rate Gyros	60

LIST OF ILLUSTRATIONS (concluded)

Figure		Page
35.	Yaw Rate Transient Response, Filtered Rate Gyros	61
36.	Lateral-Directional Root Locus, Clean Sensors	63
37.	Lateral-Directional Root Locus, Rotor Feedback	64

LIST OF TABLES

Table		Page
1.	High Gain Control Design Results	69

LIST OF SYMBOLS

a	Rotor blade lift slope (5.75)
B	Pertaining to blade coordinate system
c	Rotor blade chord length
c_t or C_T	Thrust coefficient
D	Control to response coupler matrix
e	Rotor hinge offset from hub (.203m)
F	State dynamic matrix
G	Control to state coupler matrix
H	State to response coupler matrix, compensation element; angular momentum; hub coordinate frame
h	Rotor vertical offset from C.G. (h_F = 2.093m, h_R = 3.527m)
I	Inertial coordinate frame
I_{xx}, I_{yy}, I_{zz}	Mass moment of inertias for X, Y, and Z axes, respectively
I_{xy}, I_{xz}	Mass product of inertias for X-Y and X-Z planes, respectively
k	Gain elements and matrix
l	Rotor forward offset from c.g. (l_F = 6.425m, l_R = -5.450m)
M	Moment
m	Mass, control vector dimension
n	State vector dimension
n_x, n_y, n_z	Accelerations along X, Y, Z body axes, respectively
P, Q, R	Body axes angular rate for roll, pitch, and yaw, respectively
p, q, r	Body axes perturbated angular rates for roll, pitch, and yaw, respectively
R	Rotor blade length (9.144m); rotor coordinate frame
r	Response vector, rotor blade length variable
S	Laplace variable, shaft coordinate frame

T	Dynamic compensation element, coordinate rotation matrix
T_c	Normalized rotor thrust
TF	Transfer function
TFR	Rotor transfer function
u	Control vector
U, V, W	Velocities along X, Y, and Z body axes, respectively
u, v, w	Perturbated velocities along X, Y, and Z body axes, respectively
U_T, U_P	Velocities tangential and perpendicular to rotor blade element
x	State vector
X, Y, Z	Orthogonal axis system

GREEK

α	Blade angle of attack
β	Rotor blade flap angle, flapping coordinate frame
$\beta_o, \beta_c, \beta_s$	Rotor coning, longitudinal flapping, and lateral flapping angles
β'	Vehicle sideslip angle
$\delta_B, \delta_C, \delta_S, \delta_R$	Control inputs for differential collective, gang collective, gang lateral cyclic, and differential lateral cyclic, respectively
ζ	Rotor blade lag angle
η	Blade C.G. lateral offset from hinge point
θ	Rotor blade pitch angle
$\theta_o, \theta_c, \theta_s$	Rotor blade collective, lateral cyclic, and longitudinal cyclic inputs, respectively
λ	In-flow ratio
μ	Advance ratio
ν	Interference parameter

ρ	Density of air
ρ_B	Blade density
σ	Solidity ratio (0.067)
ψ	Rotor angular position
Ω	Rotor angular rate
Ω_o	Rotor governor rate (24 rad/sec)
ω	Frequency

SUBSCRIPTS

a	Aircraft
c	Commanded value
D	Drag
F	Fuselage
H	Hub
I	Inertial
L	Lift
m	Measured
o	Nominal or trim
R,r	Rotor

HELICOPTER HIGH GAIN CONTROL

Thomas B. Cunningham, Edwin C. Nunn

SECTION 1

INTRODUCTION AND OVERVIEW

Introduction

For most helicopters, some form of feedback stability augmentation is required to obtain acceptable flying qualities over the flight envelope. Recent designs include the use of model-following designs to meet certain mission requirements. Various command modes (such as attitude or velocity) can be designed with a model-following approach. Large feedback gains are desirable to improve tolerance of variations in mass and aerodynamic parameters, rejection of disturbances, and compliance with pilot commands. Whether these model-following designs are constructed using classical or modern control methodology, practical constraints limit feedback gain levels.

Recognition of achievable gain levels must be part of the design process if high gain feedback is to be implemented. If gain limitations are known and are considered during the design, signal shaping and feedforward signals can be employed to compensate for some gain and bandwidth limitations. Neglecting these constraints during design will result in flight test problems forcing gain reductions which may seriously degrade overall system performance.

Benefits

The primary benefit of high gain design is improved performance of VTOL aircraft through improved control. The prospect of reduced sensitivity to parameter variations is extremely important in the terminal area.

Near-term benefits are:

- Maximum bandwidth achievement of the three axis augmentation loops consistent with adequate stability margins
- Identification of parameters limiting the bandwidth (such as actuator nonlinearity, rotor dynamics, etc.)
- Indication of ways of accommodating the gain limitations in control law synthesis to obtain satisfactory performance

Overview

The design study had two phases, modeling and design. Modeling was performed on the dynamics representing all gain-phase shaping elements of the vehicle and its control hardware. Hardware anomolies of gain limiting importance, such as control nonlinearities and sensor noise, were also examined. The control design effort was based upon successive eliminations of limiting factors imposed by modeled hardware constraints. In designs for the lateral-directional axes, comparisons to similar efforts performed at NASA Langley Research Center[1] were made. Finally, sensitivity was examined at numerous portions of the flight envelope for necessary gain changing to achieve a consistent response in all regimes of flight.

Modeling

The NASA/Army/Boeing Vertol CH-97B helicopter and its current control hardware mechanization were modeled in four areas.

Rigid Body. - The aerodynamic data necessary to model the rigid body motion of the CH-47B aircraft were supplied by NASA LRC.[2] Results from a model verification flight test conducted as part of the study effort demonstrated close comparisons with the provided data.

Actuator Dynamics. - Hangar and flight tests were conducted to identify actuator dynamics and nonlinearities and verify rigid body representations. Discussed in detail in Section 2 and Appendix C, these tests led to the development of dynamic models for the Electronic Control System (ECS) actuator and the lower and upper boost actuation systems. Also, important nonlinearities were examined and modeled. These included ECS rate limits and primary flight control system hysteresis. The pitch axis control hysteresis was extensive and eventually was the bandwidth limiting factor. Dynamic response impact was greatest from the upper boost roll-off characteristics. Second-order models for pitch, roll, and yaw upper boost actuators featured natural frequencies of 46, 50, and 37 rad/sec, respectively.

Rotor Dynamics. - Flapping modes were modeled for each of the two rotors in tandem. Models were derived through multiblade coordinate representation[3,4] and structured in state space to be appropriately mated to the rigid body model. Rotor interaction, an important consideration,[5] was modeled through empirically derived transcendental relationships.[2] A twelfth-order dynamic model resulted, which allowed examination of rotor

feedback control. The model can be simplified to reduced order representations. Coning for pitch axis control design reduced to a realization resembling a notch filter. Lateral and differential cyclic transfer through rotor dynamics reduced to fourth-order models.

Sensor Models.- Rate and attitude gyro sensors were used for the rigid body feedback designs. Rate gyros displayed parasitic outputs at multiples of the rotor governor frequency (24 rad/sec). The magnitudes of these outputs had to be reduced in all implementable feedback designs to avoid excessive actuator activity. Roll rate gyro noise, in particular, was high in magnitude. This proved to be the gain limiting factor in the roll control design. Verification and magnitudes for one- and three-per-rev noise models were derived from flight test results conducted as part of the contract effort and additional data supplied by NASA.

Control Design

High gain control allows design confidence in feed forward compensation to result in desired vehicle response characteristics. The specific goals used were high bandwidth second-order dominated responses for pitch and roll attitudes and first-order dominated response for yaw rate.

Modal control, a new multiple input control design technique,[6,7] was used to carry out the design goals. This technique is based on eigenvalue-eigenvector placement of the closed loop system. Therefore, the specific design goals can be embedded into the control design algorithm.

Pitch axis designs resulted in a closed loop control bandwidth which was limited by control hysteresis. Elimination of this will produce results only slightly better because of a pitch rate gyro attenuation filter needed to eliminate the one- and three-per-rev sensor noise. Eliminating the noise source or allowing higher actuator activity will allow higher bandwidth. This was examined by assuming no filtering on the pitch rate gyro. Rotor feedback allows higher bandwidth designs to be possible, but results in rigid body feedback gains too high to accommodate current sensor noise and actuator nonlinear characteristics.

Roll and yaw control designs were conducted simultaneously with the modal control software. When using this approach, limitations were experienced only in the roll axis. Further expansion of yaw axis bandwidths for the cases studied was not tried.

The fundamental limitation in the roll axis control is the one- and three-per-rev sensor noises on the roll rate gyro. Successful attenuation of these noises was achieved using notch filters at the dominant rotor frequencies, 24 and 72 rad/sec. Although very limited band notches were used, the resulting phase losses resulted in little improvement over the complementary filter approach used at NASA.[1] Further increases in the allowable bandwidth resulted from elimination of the gyro filtering. Rotor feedback again demonstrated benefits but again with extremely high rigid body feedback gains which would be impractical because of sensor noise.

Gain scheduling to assure consistent response over the flight envelope will require simple airspeed schedules on series integral gains.

Throughout the design process, it was recognized that ECS rate limiting was a potential limitation. Evaluation of this would involve more detailed analysis of the feed forward input model. This effect was included in simulation models for transient response evaluation. Large input command steps resulted in system instability; therefore, rate limiting the feed forward commands would be required.

Report Organization

The report is organized to emphasize the most important results of the effort in the main body of the report, with detailed model analysis and testing and control design theory presented in the appendixes.

Section 2 discusses the four modeling areas used: rigid body, actuator, rotor, and sensors. Section 3 contains the results for all control designs and evaluations. The effort is summarized and conclusions are drawn in Section 4.

Appendix A contains modeling details for the tandem rotor flapping model. Appendix B discusses useful techniques for using modal control design theory. Appendix C contains details of the model verification flight test procedures and subsequent model construction.

SECTION 2

MODELING

Introduction

Feedback control design typically involves designing to uncertainties. The designer performs a tradeoff between closed loop performance versus sensitivity to model uncertainty. Performance can be either transient response, external disturbance rejection, or a combination of these. Model uncertainty can arise from a number of interacting sources: errors, variations, or omissions in the design models. A partial list for an aircraft would be:

1. Rigid body model parameter uncertainty
2. Known rigid body model parameter variations
3. Control hardware uncertainties
    - bandwidth
    - nonlinearities
4. Unmodeled dynamics
    - flexure modes
    - flutter (more common to fixed wing aircraft)
    - rotor dynamics (for rotary aircraft)

5. Sensor constraints

- bandwidth
- parasitic anamolies, such as noise

Rigid body model parameter uncertainty results from errors in accounting for aerodynamic characteristics. As a new vehicle design evolves, aerodynamic data undergo continual upgrading from analytical models, through wind tunnel testing, to flight test results. A vehicle such as the CH-47 helicopter has undergone periodic parameter identification throughout its lifetime. Uncertainty in its rigid body parameters, however, will never be zero, establishing one source of need for stability margins in the feedback control design.

Known rigid body model parameter variations result from identifiable changes in a vehicle's characteristics over its operating region. These characteristics can be complex nonlinear functions, but successful control designs have traditionally resulted using quasilinear approximations throughout a given vehicle's flight envelope. Some adaptation is usually required to obtain desired performance over the range of known variations. Gain schedules on low frequency vehicle states are most common. Dynamic pressure, for example, is commonly used for fixed wing aircraft and forward speed for rotary wing vehicles. More elaborate schemes utilizing the basic flight control sensors have been successful.[10,11]

Control hardware for aircraft usually refers to servo-actuator dynamics. Characteristics such as bandwidth and nonlinearities are usually known with greater precision than aerodynamic parameters. Hardware constraints are

the most common source of bandwidth limitation (academicians are notorious for ignoring these constraints). High gain control design in particular requires accurate modeling with respect to actuator dynamic characteristics.

Unmodeled dynamics are referred to here as higher frequency vehicle characteristics. Flexure modes, flutter modes, and rotor dynamics are examples. Models exist for these dynamics but they can usually be characterized as 1) very complicated, 2) not very good, or 3) both. The easiest control design approach is to avoid these regions by low pass filtering, if possible, or by notch filtering to eliminate an uncertain band in frequency. Both techniques reduce the allowable bandwidth of the closed loop design. Active control approaches such as high frequency dynamic measurement and control are currently popular research topics.

Rotor dynamic models for low advance ratio helicopters are in better form than either flexure or flutter representations. The reason for this is simply that rotors are more precisely fixed in operation by the vehicle designer. They are usually governed to operate at a constant rate throughout a vehicle's flight envelope. This also affects greatly the vehicle's rigid body characteristics because low frequency aerodynamic characteristics are dominated by the rotor aerodynamics.

Sensor modeling can usually be a secondary consideration because 1) the sensor bandwidth is typically very high relative to the desired design bandwidth (an order of magnitude in frequency is not unusual) and 2) wide and flat band low magnitude noise usually presents few problems. The sensors on the CH-47, however, contain very well defined high magnitude spikes at

multiples of the rotor frequency. These spikes produce one of the major obstacles to high gain control.

CH-47B Rigid Body Model

The NASA/Army/Boeing Vertol CH-47B helicopter is shown in Figure 1. Linear rigid body model parameters were supplied by NASA Langley Research Center. These were derived from nonlinear equations of motion which included vertical and rotor trim and rigid body state and control perturbations from the nominal trim values. Performed using a nonlinear model called HELCOP,[2] the perturbation-derived stability coefficients can be written in state space form:

$$\begin{aligned} \dot{x}_a &= \hat{F}x_a + \hat{G}u \\ r_a &= \hat{H}x_a + \hat{D}u \end{aligned} \qquad (1)$$

where

x_a is the aircraft rigid body state vector

$$x_a^T = (u, v, w, p, q, r, \phi, \theta)$$

u is the control input vector

$$u^T = (\delta_B, \delta_C, \delta_S, \delta_R)$$

r_a is the response vector, in other words, typically all states and controls plus other responses such as body accelerations

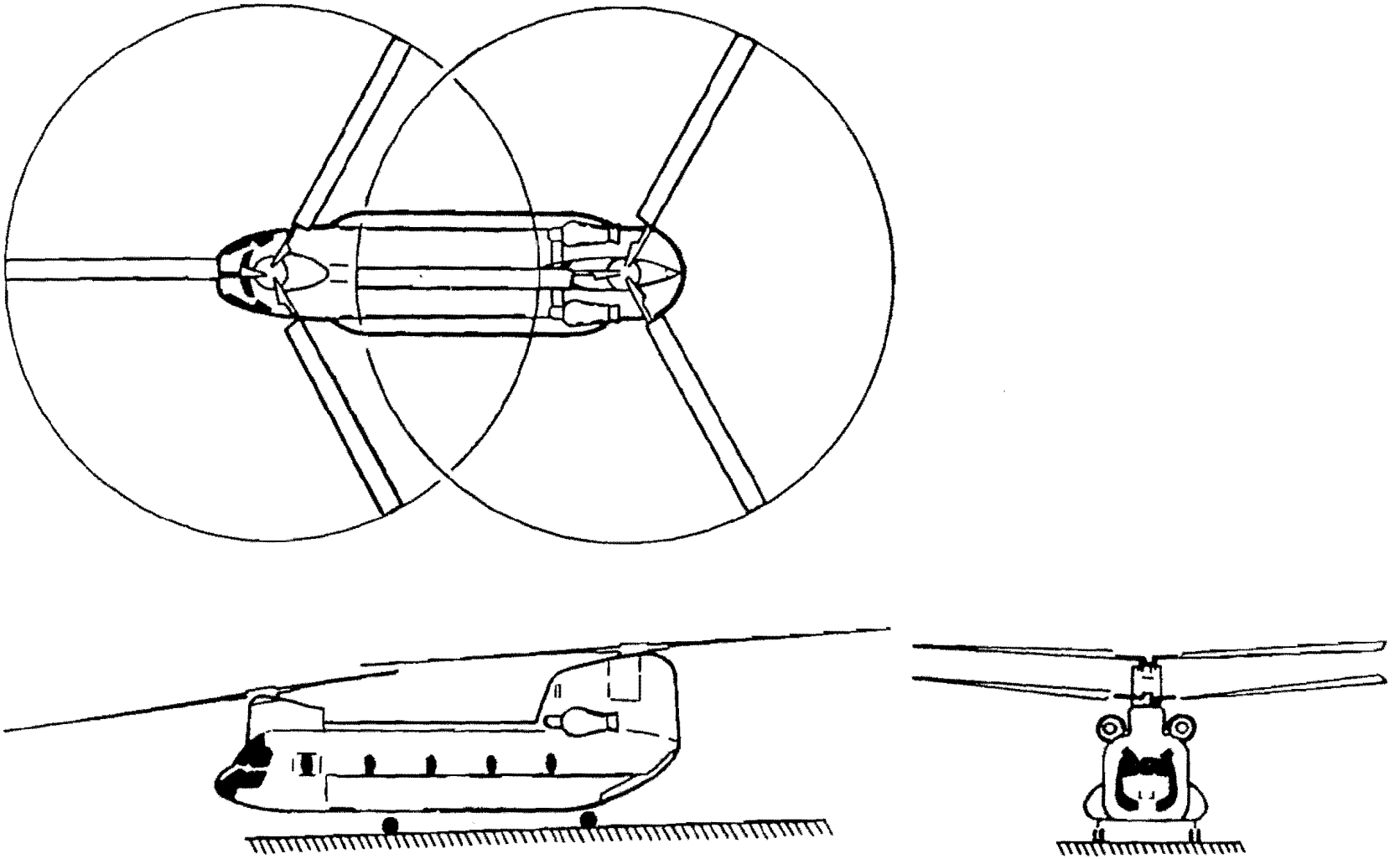

Figure 1. NASA/Army/Boeing Vertol CH-47B

$\hat{F}$ is the state compler matrix

$\hat{G}$ is the control input coupler

$\hat{H}$ is the response state coupler

$\hat{D}$ is the response control coupler

Linear coefficient values for the rigid body are listed in Appendix E of Reference 2 for 99 trim points. The rigid body model is summarized in Figure 2. Some typical open loop performance numbers are shown in Figure 3 for various flight conditions.

Rigid Body Model Validation

As part of the study a flight test was conducted to determine actuator characteristics and validate rigid body model representations from HELCOP. Discussed in more detail in Appendix C, these tests included vehicle frequency responses at hover and 41.18 m/s (80 kn) forward speed. Selected results from the flight tests were compared with HELCOP-derived frequency responses. These are shown in Figures 4-8. The agreement for data points less than 4 Hz is good. Beyond this point, however, the flight test data is corrupted by high magnitude sensor anomolies at multiples of rotor frequencies.

Rotor Models

The CH-47B rotor dynamics effect the high gain design limitations directly and indirectly. Direct impact results from the rotor physics producing attenuation. Indirectly, the impact is a result of noise spikes on sensors at

$$
\begin{bmatrix} \dot{u} \\ \dot{v} \\ \dot{w} \\ \dot{p} \\ \dot{a} \\ \dot{r} \\ \dot{\theta} \\ \dot{\phi} \end{bmatrix}
=
\begin{bmatrix}
\frac{X_U}{m} & \frac{X_V}{m} & \frac{X_W}{m} & \frac{X_P}{m} & \left(\frac{X_Q}{m} - W_0\right) & \left(\frac{X_R}{m} + V_0\right) & -g\cos\theta_0 & 0 \\
\frac{Y_U}{m} & \frac{Y_V}{m} & \frac{Y_W}{m} & \left(\frac{Y_P}{m} + W_0\right) & \frac{Y_Q}{m} & \left(\frac{Y_R}{m} - U_0\right) & -g\sin\theta_0\sin\phi_0 & g\cos\phi_0\cos\theta_0 \\
\frac{Z_U}{m} & \frac{Z_V}{m} & \frac{Z_W}{m} & \left(\frac{Z_P}{m} - V\right) & \left(\frac{Z_Q}{m} + U\right) & \frac{Z_R}{m} & -g\sin\theta_0\cos\phi_0 & -g\cos\phi_0\sin\phi_0 \\
\left(\frac{I_1L_U}{I_{XX}} + \frac{I_3N_U}{I_{ZZ}}\right) & \left(\frac{I_1L_V}{I_{XX}} + \frac{I_3N_V}{I_{ZZ}}\right) & \left(\frac{I_1L_W}{I_{XX}} + \frac{I_3N_W}{I_{ZZ}}\right) & \left(\frac{I_1L_P}{I_{XX}} + \frac{I_3N_P}{I_{ZZ}}\right) & \left(\frac{I_1L_Q}{I_{XX}} + \frac{I_3N_Q}{I_{ZZ}}\right) & \left(\frac{I_1L_R}{I_{XX}} + \frac{I_3N_R}{I_{ZZ}}\right) & 0 & 0 \\
\frac{M_U}{I_{YY}} & \frac{M_V}{I_{YY}} & \frac{M_W}{I_{YY}} & \frac{M_P}{I_{YY}} & \frac{M_Q}{I_{YY}} & \frac{M_R}{I_{YY}} & 0 & 0 \\
\left(\frac{I_2L_U}{I_{XX}} + \frac{I_1N_U}{I_{ZZ}}\right) & \left(\frac{I_2L_V}{I_{XX}} + \frac{I_1N_V}{I_{ZZ}}\right) & \left(\frac{I_2L_W}{I_{XX}} + \frac{I_1N_W}{I_{ZZ}}\right) & \left(\frac{I_2L_P}{I_{XX}} + \frac{I_1N_P}{I_{ZZ}}\right) & \left(\frac{I_2L_Q}{I_{XX}} + \frac{I_1N_Q}{I_{ZZ}}\right) & \left(\frac{I_2L_R}{I_{XX}} + \frac{I_1N_R}{I_{ZZ}}\right) & 0 & 0 \\
0 & 0 & 0 & 0 & \cos\phi_0 & -\sin\phi_0 & 0 & 0 \\
0 & 0 & 0 & 1 & \sin\phi_0\tan\theta_0 & \cos\phi_0\tan\theta_0 & 0 & 0
\end{bmatrix}
\begin{bmatrix} u \\ v \\ w \\ p \\ a \\ r \\ \theta \\ \phi \end{bmatrix}
$$

$$
+
\begin{bmatrix}
\frac{X_{\delta_B}}{m} & \frac{X_{\delta_C}}{m} & \frac{X_{\delta_S}}{m} & \frac{X_{\delta_R}}{m} \\
\frac{Y_{\delta_B}}{m} & \frac{Y_{\delta_C}}{m} & \frac{Y_{\delta_S}}{m} & \frac{Y_{\delta_R}}{m} \\
\left(\frac{I_1L_{\delta_B}}{I_{XX}} + \frac{I_3N_{\delta_B}}{I_{ZZ}}\right) & \left(\frac{I_1L_{\delta_C}}{I_{XX}} + \frac{I_3N_{\delta_S}}{I_{ZZ}}\right) & \left(\frac{I_1L_{\delta_S}}{I_{XX}} + \frac{I_3N_{\delta_S}}{I_{ZZ}}\right) & \left(\frac{I_1L_{\delta_R}}{I_{XX}} + \frac{I_3N_{\delta_R}}{I_{ZZ}}\right) \\
\frac{M_{\delta_B}}{I_{YY}} & \frac{M_{\delta_C}}{I_{YY}} & \frac{M_{\delta_S}}{I_{YY}} & \frac{M_{\delta_R}}{I_{YY}} \\
\left(\frac{I_2L_{\delta_B}}{I_{XX}} + \frac{I_1N_{\delta_B}}{I_{ZZ}}\right) & \left(\frac{I_2L_{\delta_C}}{I_{XX}} + \frac{I_1N_{\delta_C}}{I_{ZZ}}\right) & \left(\frac{I_2L_{\delta_S}}{I_{XX}} + \frac{I_1N_{\delta_S}}{I_{ZZ}}\right) & \left(\frac{I_2L_{\delta_R}}{I_{XX}} + \frac{I_1N_{\delta_R}}{I_{ZZ}}\right) \\
0 & 0 & 0 & 0 \\
0 & 0 & 0 & 0
\end{bmatrix}
\begin{bmatrix} \delta_B \\ \delta_C \\ \delta_S \\ \delta_R \end{bmatrix}
$$

WHERE

$$I_1 = \frac{I_{XX}I_{ZZ}}{I_{XX}I_{ZZ} - I_{XZ}^2}$$

$$I_2 = \frac{I_{XX}I_{XZ}}{I_{XX}I_{ZZ} - I_{XZ}^2}$$

$$I_3 = \frac{I_{ZZ}I_{XZ}}{I_{XX}I_{ZZ} - I_{XZ}^2}$$

Figure 2. CH-47B Rigid Body Model, Taken from Reference 2, p. 89

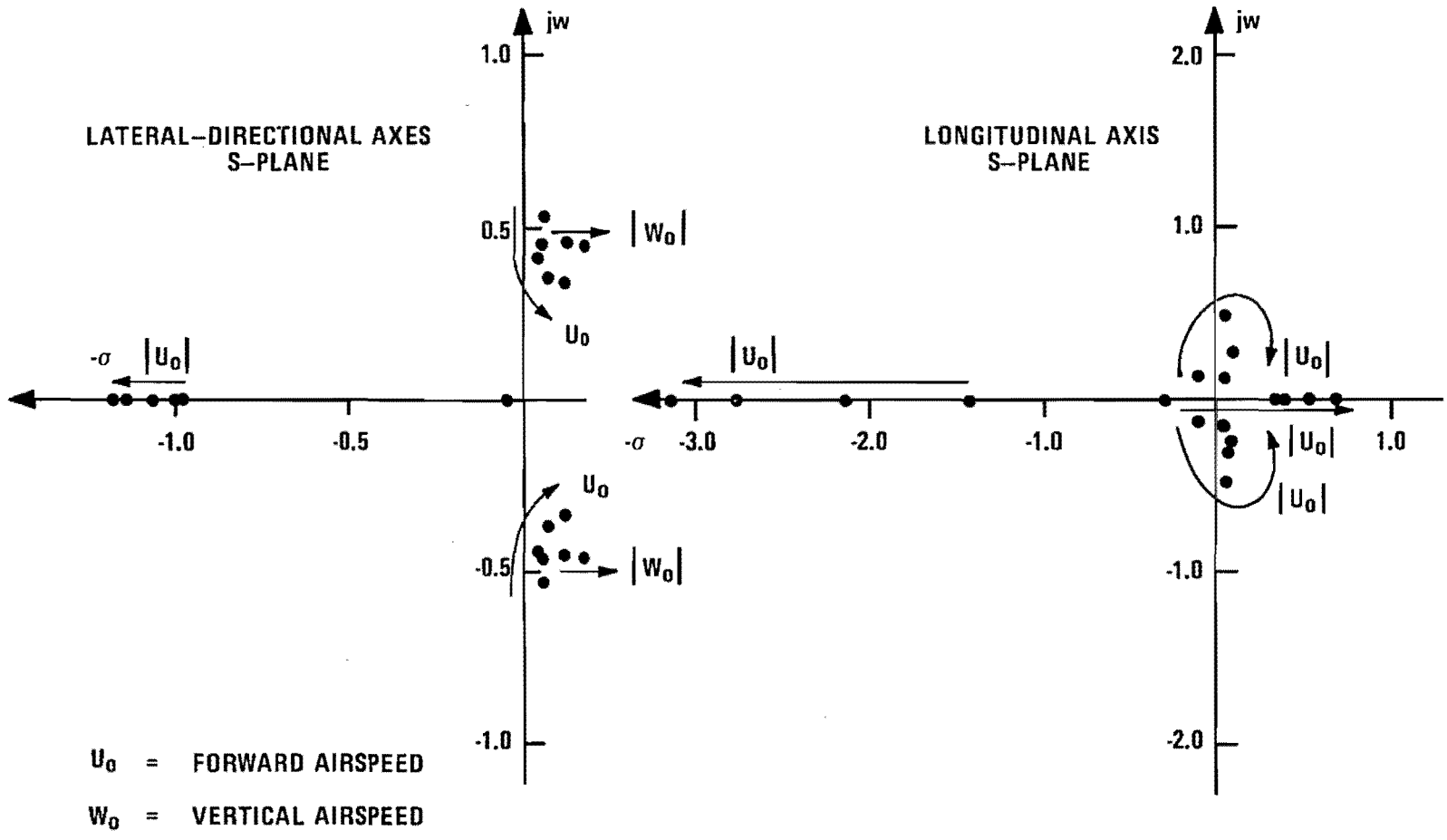

Figure 3. CH-47B Open Loop Characteristics

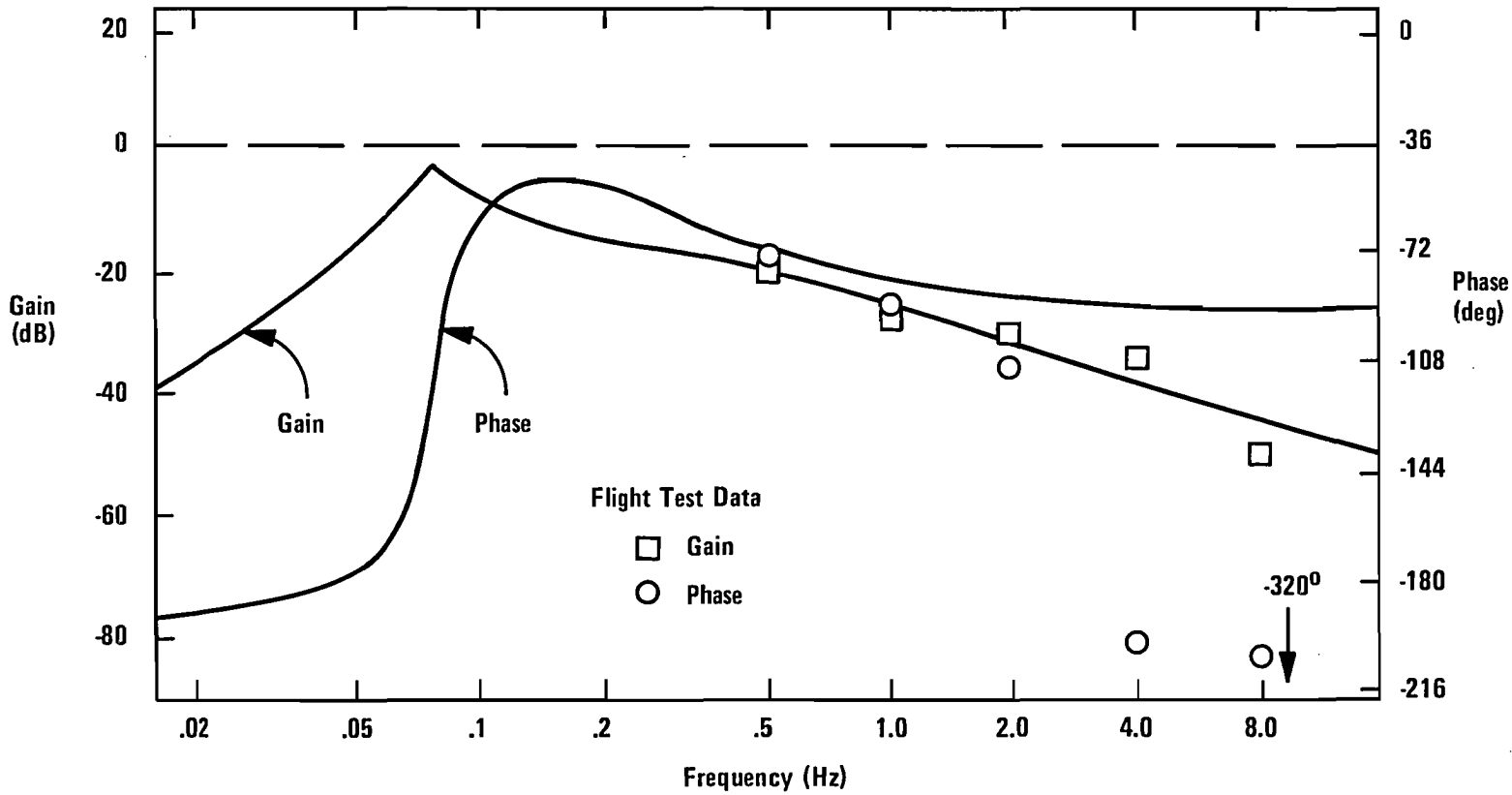

Figure 4. Analytical Versus Flight Test Frequency Response (q/δ_B) Hover

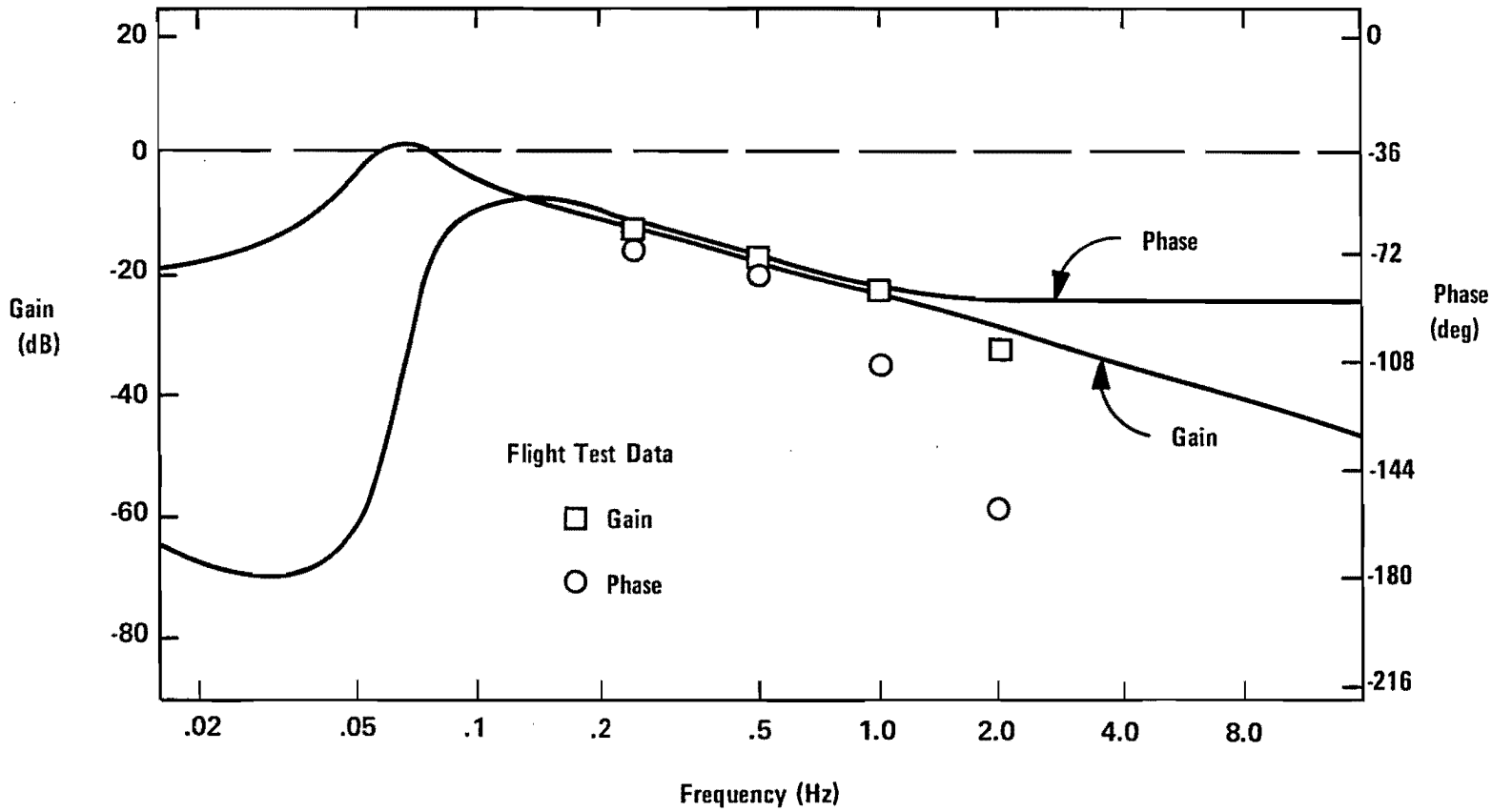

Figure 5. Analytical Versus Flight Test Frequency Response (p/δ_S) Hover

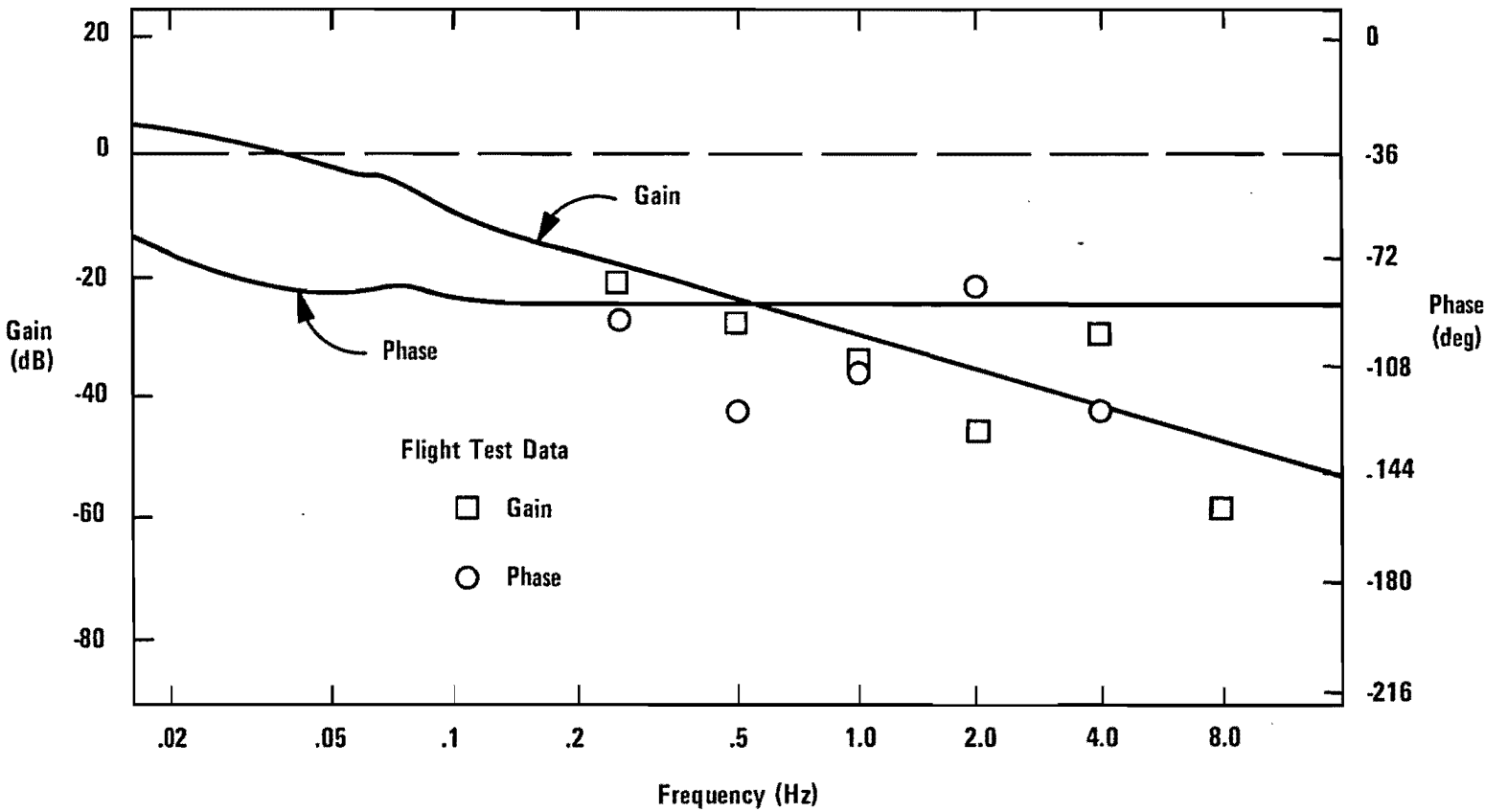

Figure 6. Analytical Versus Flight Test Frequency Response (r/δ_R) Hover

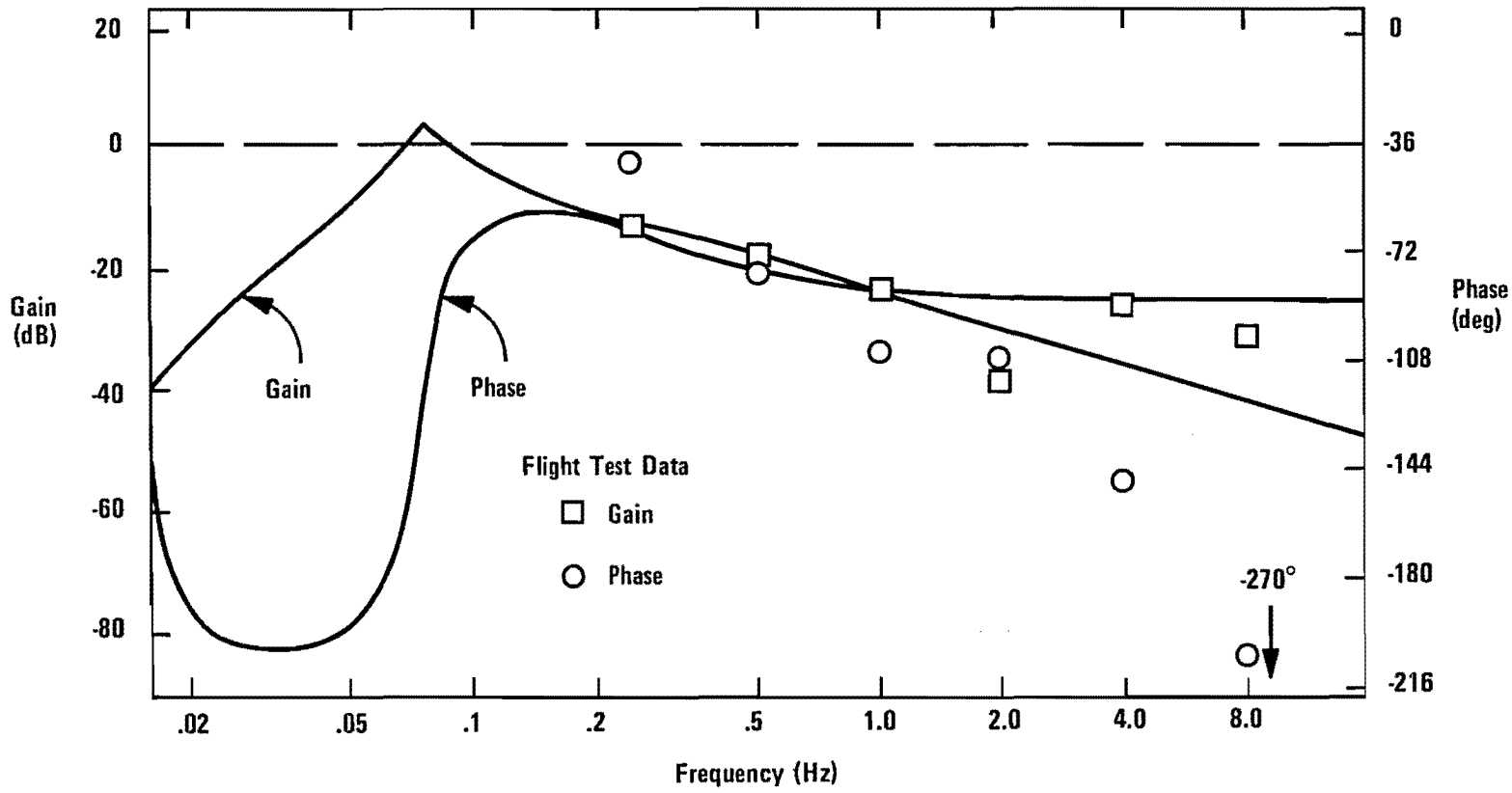

Figure 7. Analytical Versus Flight Test Frequency Response
(p/δ_S) U_0 = 41.18 m/s (80 kn)

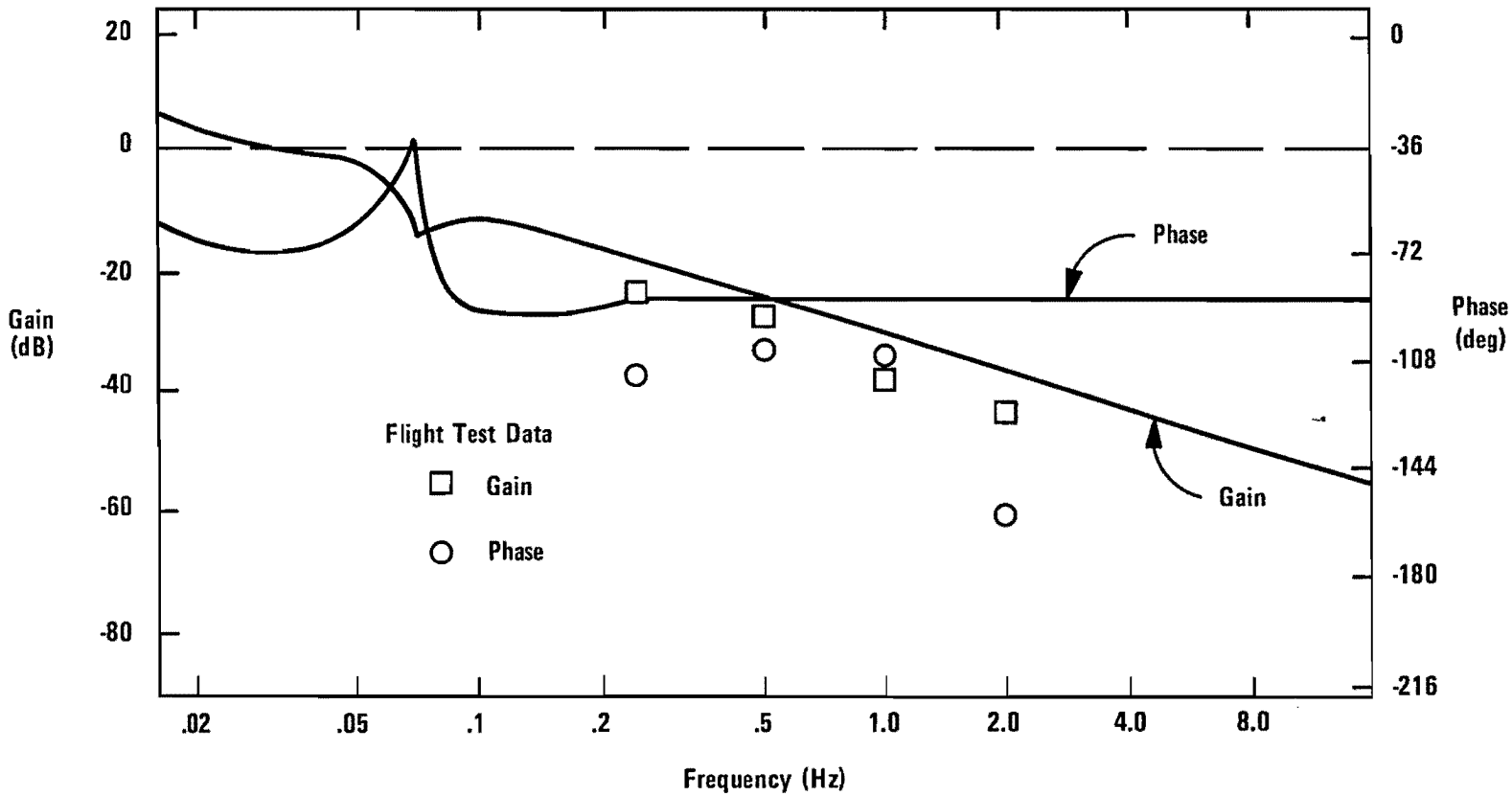

Figure 8. Analytical Versus Flight Test Frequency Response
(r/δ_R) U_0 = 41.18 m/s (80 kn)

multiples of the rotor frequency (24 rad/sec). This latter difficulty is discussed later.

Rotor Flapping Equations of Motion

Appendix A contains a complete description of the derivation of the coupled rigid body/rotor flapping dynamics for the CH-47B vehicle. Summarizing this development, the rigid body/rotor flapping dynamics can be modeled in state space

$$\begin{aligned} \dot{x} &= Fx + Gu \\ r &= Hx + Du \end{aligned} \tag{2}$$

where:

x is the rigid body/rotor state vector

$$x^T = (x_a{}^T, x_r{}^T)$$

x_a is the aircraft state

$$x_a{}^T = (u, v, w, p, q, r, \theta, \phi)$$

x_r is the rotor state

$$x_r{}^T = (\beta_{OF}, \beta_{OF}, \beta_{CF}, \beta_{CF}, \beta_{SF}, \beta_{SF}, \beta_{OR}, \beta_{OR}, \beta_{CR}, \beta_{CR}, \beta_{SR}, \beta_{SR})$$

u is the control input vector [same as (1)]

r is the response vector

$$r^T = (r_a^T, r_r^T)$$

$$r_r^T = \text{rotor states}$$

F is the state coupler

$$F = \begin{bmatrix} F_{a,a} & F_{a,r} \\ F_{r,a} & F_{r,r} \end{bmatrix}$$

$F_{a,a}$ is the state coupler from aircraft states to aircraft equations*

$F_{a,r}$ is the state coupler from rotor states to aircraft equations

$F_{r,a}$ is the state coupler from aircraft states to rotor equations

$F_{r,r}$ is the state coupler from rotor states to rotor equations

G is the control coupler

$$G = \begin{bmatrix} G_a \\ G_r \end{bmatrix}$$

G_a is the control coupler to the aircraft equations*

---

*$F_{a,a} \neq \hat{F}$ and $G_a \neq \hat{G}$. $\hat{F}$ and $\hat{G}$ are derived by residualizing the rotor dynamics of equation (2) as explained in Appendix A.

G_r is the control coupler to the rotor equations

H and D are the response coupler matrixes from the state and control respectively. Equation (1) is augmented with rotor states to complete this.

Transfer Function Rotor Model

Although a twelfth-order model is necessary for individual rotor dynamic observance and (as discussed in Section 3) rotor feedback control, this model can be simplified without loss in validity for inclusion of rotor frequency impact on individual transfer functions. Figures 9 and 10 show the frequency responses of key transfer functions for the CH-47B.

Pole-zero calculations yield the transfer function models shown in Figure 11. These can be appended to existing rigid body model transfer functions and will produce results very close to the state space models. Some observations can also be made about the flapping model used.

- The collective model (blade coning) is a notch filter at the rotor frequency. This is supported by intuition, since coning has equal portions of up flap and down flap over one revolution of an input frequency at 24 rad/sec. The average value is therefore zero.
- The models do not contain high frequency attenuation.
- The transfer functions are almost invariant through the flight envelope. This is true despite significant changes in some rotor model parameters. The dynamics, however, are dominated by rotor frequency terms.

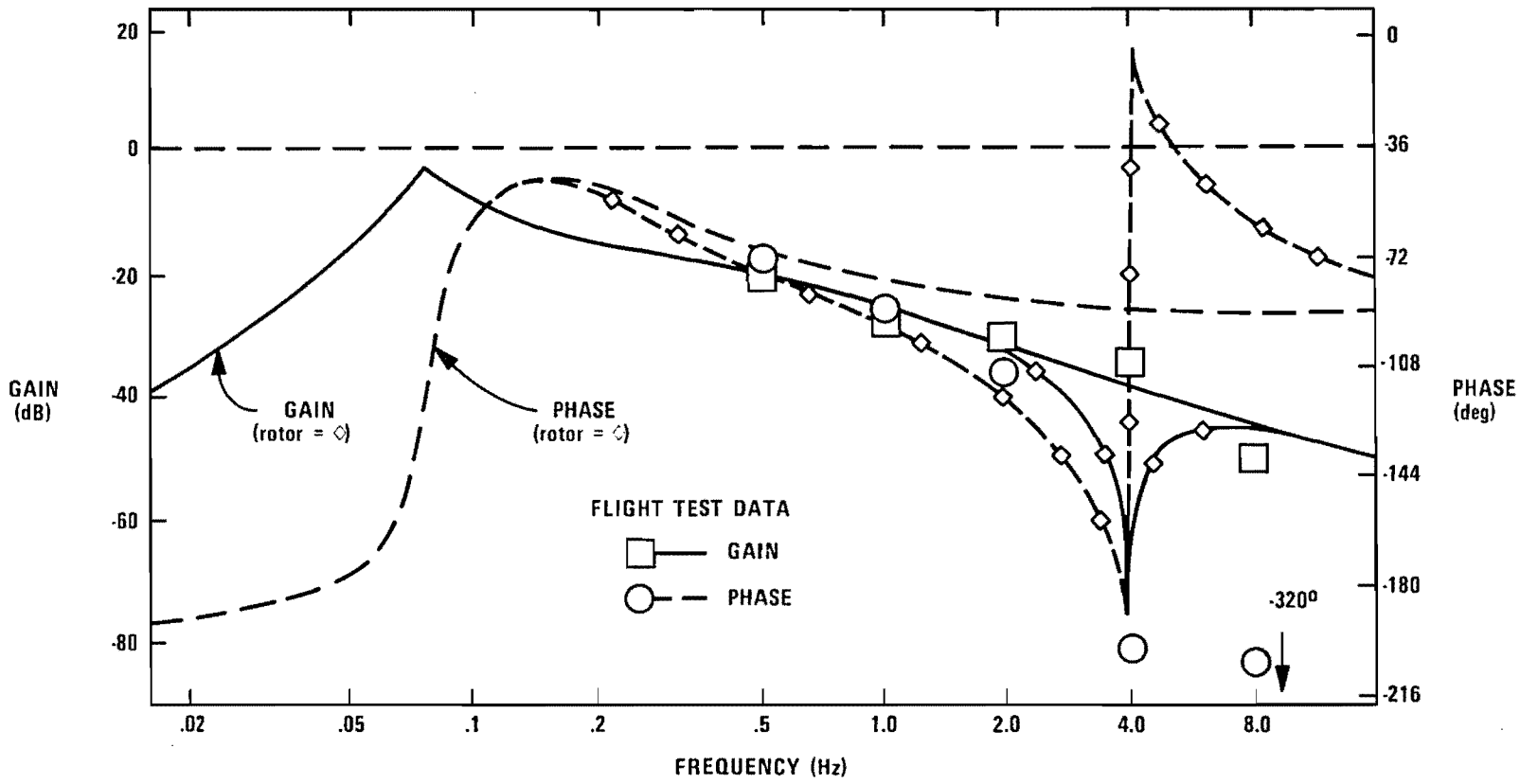

Figure 9. Analytical Model With Rotor Frequency Response (q/δ_B) Hover

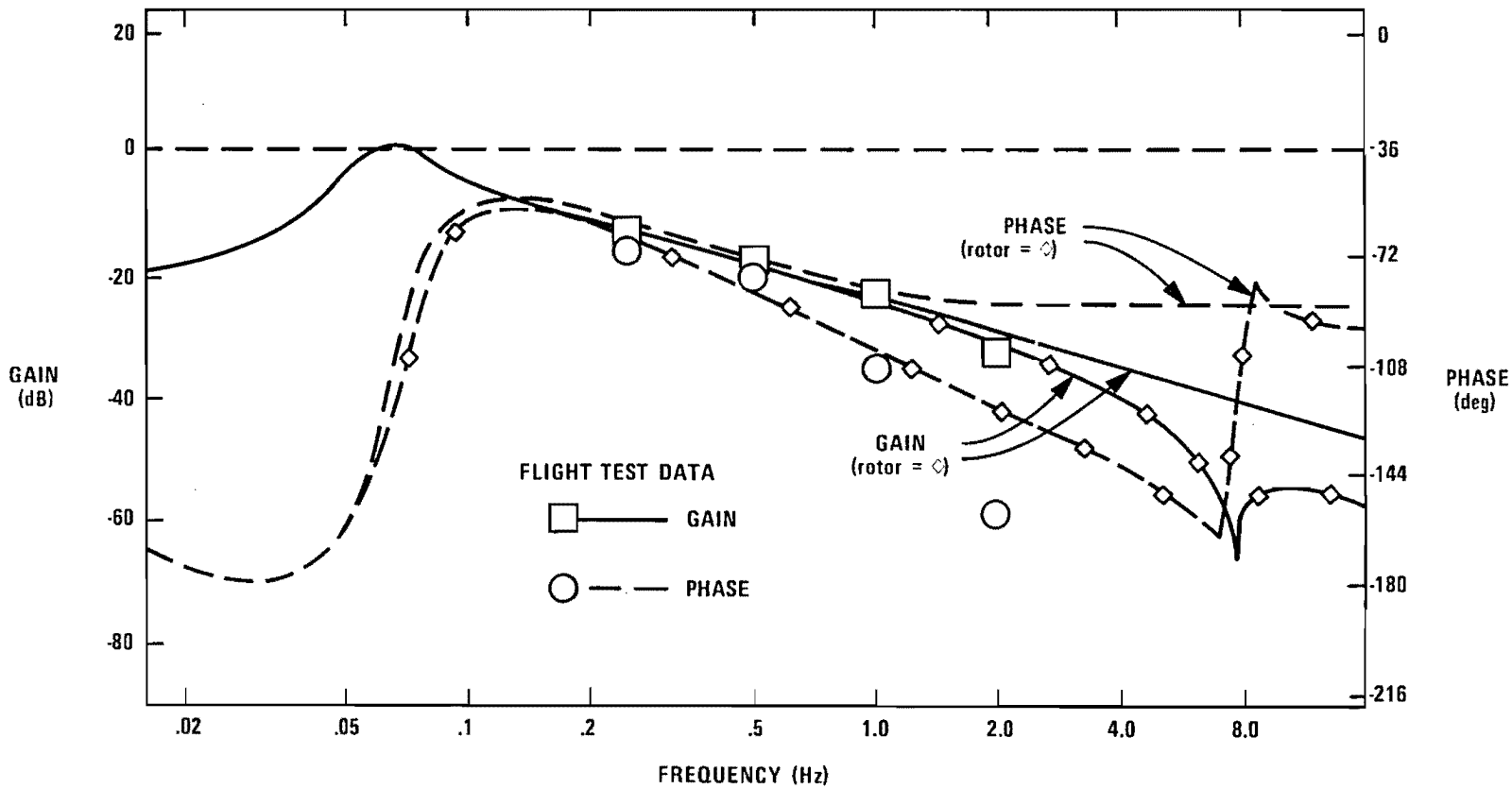

Figure 10. Analytical Model With Rotor Frequency Response (p/δ_S) Hover

DIFFERENTIAL COLLECTIVE	LATERAL CYCLIC	DIFFERENTIAL CYCLIC
$TFR_{\delta B} = \dfrac{\left(\dfrac{S^2}{W_n^2} + \dfrac{2\zeta_n S}{W_n} + 1\right)}{\left(\dfrac{S^2}{W_d^2} + \dfrac{2\zeta_d S}{W_d} + 1\right)}$	$TFR_{\delta S} = \dfrac{\left(\dfrac{S}{W_n^2} + \dfrac{2\zeta_n S}{W_n} + 1\right)\left(\dfrac{S}{Z_1} + 1\right)\left(\dfrac{S}{Z_2} + 1\right)}{\left(\dfrac{S^2}{W_{d1}^2} + \dfrac{2\zeta_{d1} S_d}{W_{d1}} + 1\right)\left(\dfrac{S^2}{W_{d2}^2} + \dfrac{2\zeta_{d2} S}{W_{d2}} + 1\right)}$	$TFR_{\delta P} = \dfrac{\left(\dfrac{S^2}{W_n^2} + \dfrac{2\zeta_n S_n}{W_n} + 1\right)\left(\dfrac{S}{Z_1} + 1\right)\left(\dfrac{S}{Z_2} + 1\right)}{\left(\dfrac{S^2}{W_{d1}^2} + \dfrac{2\zeta_{d1} S_d}{W_d} + 1\right)\left(\dfrac{S^2}{W_{d2}^2} + \dfrac{2\zeta_{d2} S}{W_d^2} + 1\right)}$
WHERE:	WHERE:	WHERE:
W_n = 24.47 r/s	W_n = 47.39 ± 2.0 r/s	W_n = 43.0 ± 1.0 r/s
ζ_n = .021 ± .015	ζ_n = .074 ± .060	ζ_n = 0.0 ± .07
W_d = 24.00 ± .20 r/s	Z_1 = 11.53 ± .40 r/s	Z_1 = 11.1 ± .4 r/s
ζ_d = .478 ± .03	Z_2 = 53.12 ± 20. r/s (INCREASES WITH |AIRSPEED|)	Z_2 = 51.65 ± 30. r/s (INCREASES WITH |AIRSPEED|)
$TFR = \dfrac{q/_{\delta B}\text{ (With Rotor)}}{q/_{\delta B}\text{ (Without Rotor)}}$	W_{d1} = 46.81 ± .03 r/s	W_{d1} = 46.81 ± .02 r/s
	ζ_{d1} = .262	ζ_{d1} = .265
	W_{d2} = 12.84 ± .02 r/s	W_{d2} = 12.70 ± .01 r/s
	ζ_{d2} = .972	ζ_{d2} = .974
	$TFR = \dfrac{p/\delta_s\text{(With Rotor)}}{p/\delta_s\text{(Without Rotor)}}$	$TFR = \dfrac{r/_{\delta R}\text{(With Rotor)}}{r/_{\delta R}\text{(Without Rotor)}}$

*± errors determined from 12th-order model applied over flight envelope

Figure 11. Transfer Function Rotor Models*

Actuator Models

The major function of the model verification flight tests was to investigate actuator dynamic characteristics. Appendix C contains procedural details for this effort and a composite actuator model for the three input controls of interest.

Figure 12 contains another version of the Appendix C model (Figure C-1). This version has been adjusted to mate with helicopter rigid body and rotor dynamics by establishing unity steady state gain, phase variable formulation, and a backlash model incorporated by means of an upper boost rate deadband term. This latter simplification is demonstrated in general in Figure 13.

Sensor Models

Sensor characteristics typically go unmodeled for flight control design because rough notions of bandwidth and noise are accounted for implicitly in the sensor choices. This is one of the few hardware areas where the control designer has some voice (because he is the only one with a need for flight control variable sensors).

The flight control sensors for the CH-47B, however, display well defined vibration modes in multiples of rotor frequencies. In addition to the spectral plots displayed in Appendix C (Figures C11-C14) NASA has generated spectrum magnitude plots for sensor outputs. Shown in Figures 14, 15, and 16, these plots were generated without excitation of the vehicle. The 12 Hz spike in Figure 15 is particularly large. This occurs at three times the rotor frequency.

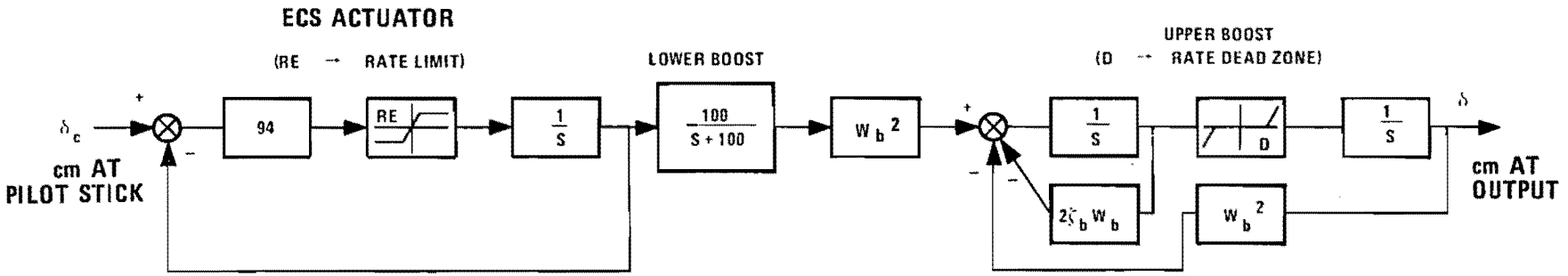

CONTROL AXIS	ECS RATE LIMITS	UPPER BOOST MODEL		
		W_b	ζ_b	D
PITCH (δb)	25.9 cm/s (10.2 in/s)	46 r/s	.45	12.4 cm/s (4.87 in/s)
ROLL (δs)	16.8 cm/s (6.6 in/s)	50 r/s	.50	3.48 cm/s (1.37 in/s)
YAW (δr)	15.1 cm/s (5.93 in/s)	37 r/s	.50	3.35 cm/s (1.32 in/s)

Figure 12. CH-47B Actuator Models

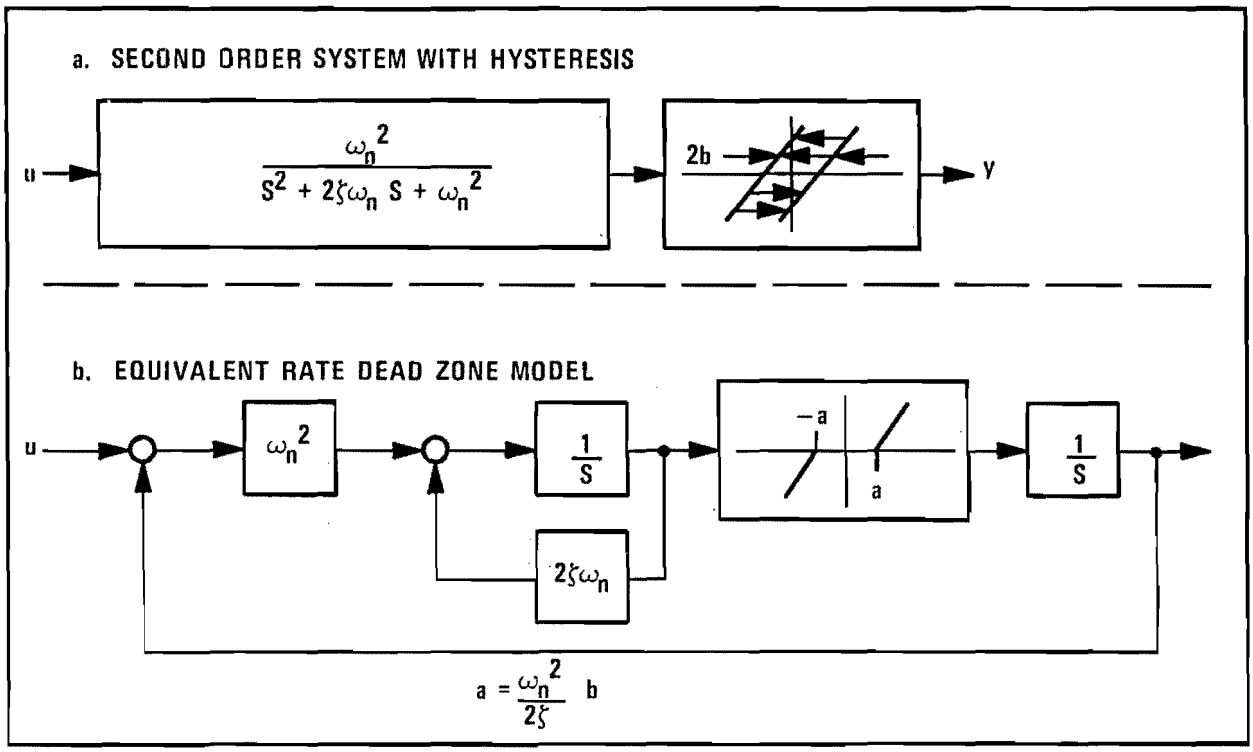

Figure 13. Hysteresis Model

The actual source of this noise is probably related to rotor dynamics and, in particular, the fact that there are three blades per rotor. The rotor dynamics discussed earlier lead to an interesting conjecture about this. The notch filter description of the rotor transfer functions (Figure 11) leaves some doubt as to where the input energy at the rotor frequency has dissipated. The explanation of equal up and down flapping at the rotor frequency in the coning model also points to an off-axis response in cyclic, both longitudinal and lateral, for a coning command input. Since this phenomenon is not modeled, a matchup of this idea and the sensor output spikes could be explored.

In any case, these oscillations corrupt the performance of feedback designs as gains on these sensors are increased.[1] Specific details on how to deal with this problem are discussed in the next section.

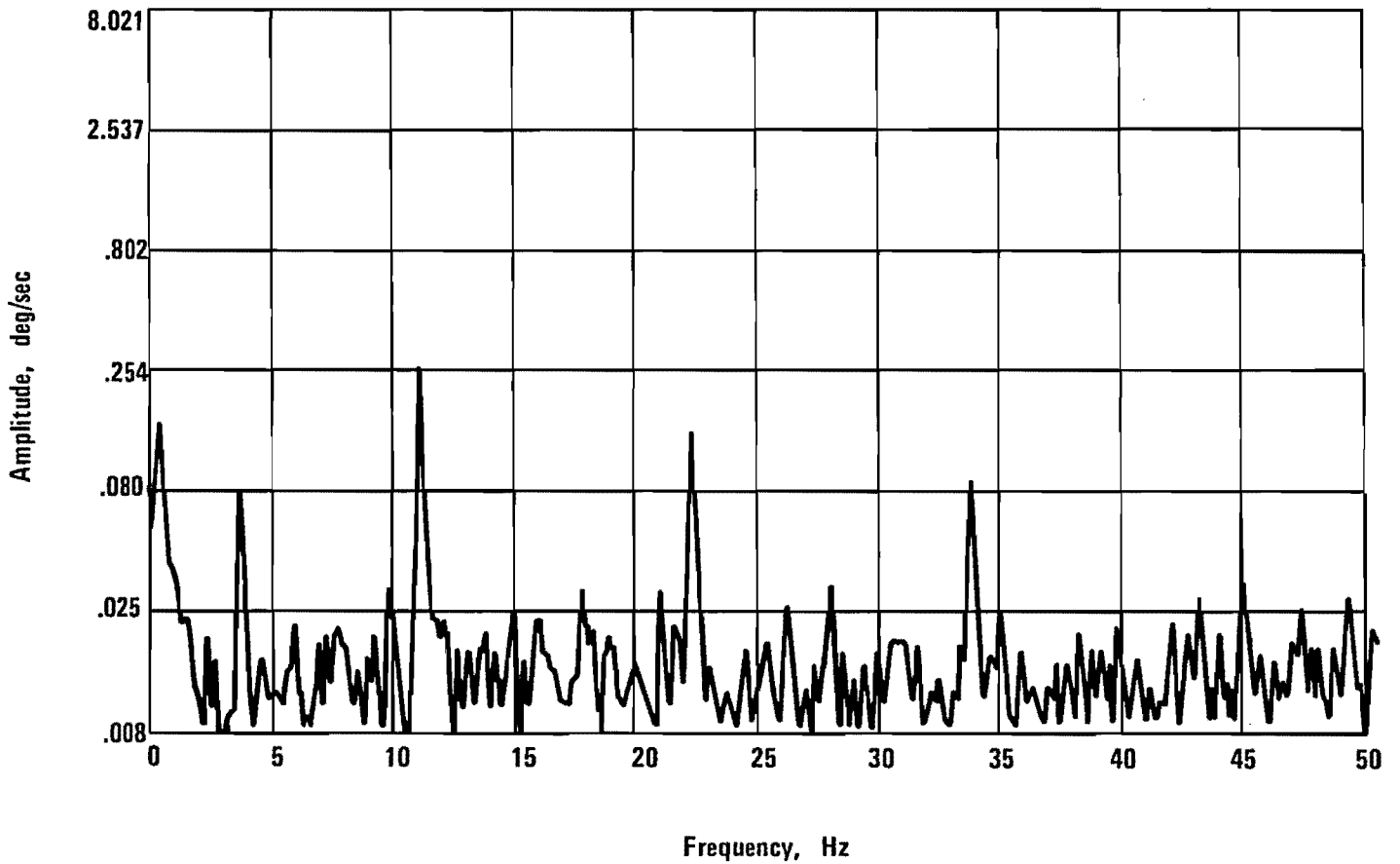

Figure 14. Pitch Rate Spectral Analysis (Hover)

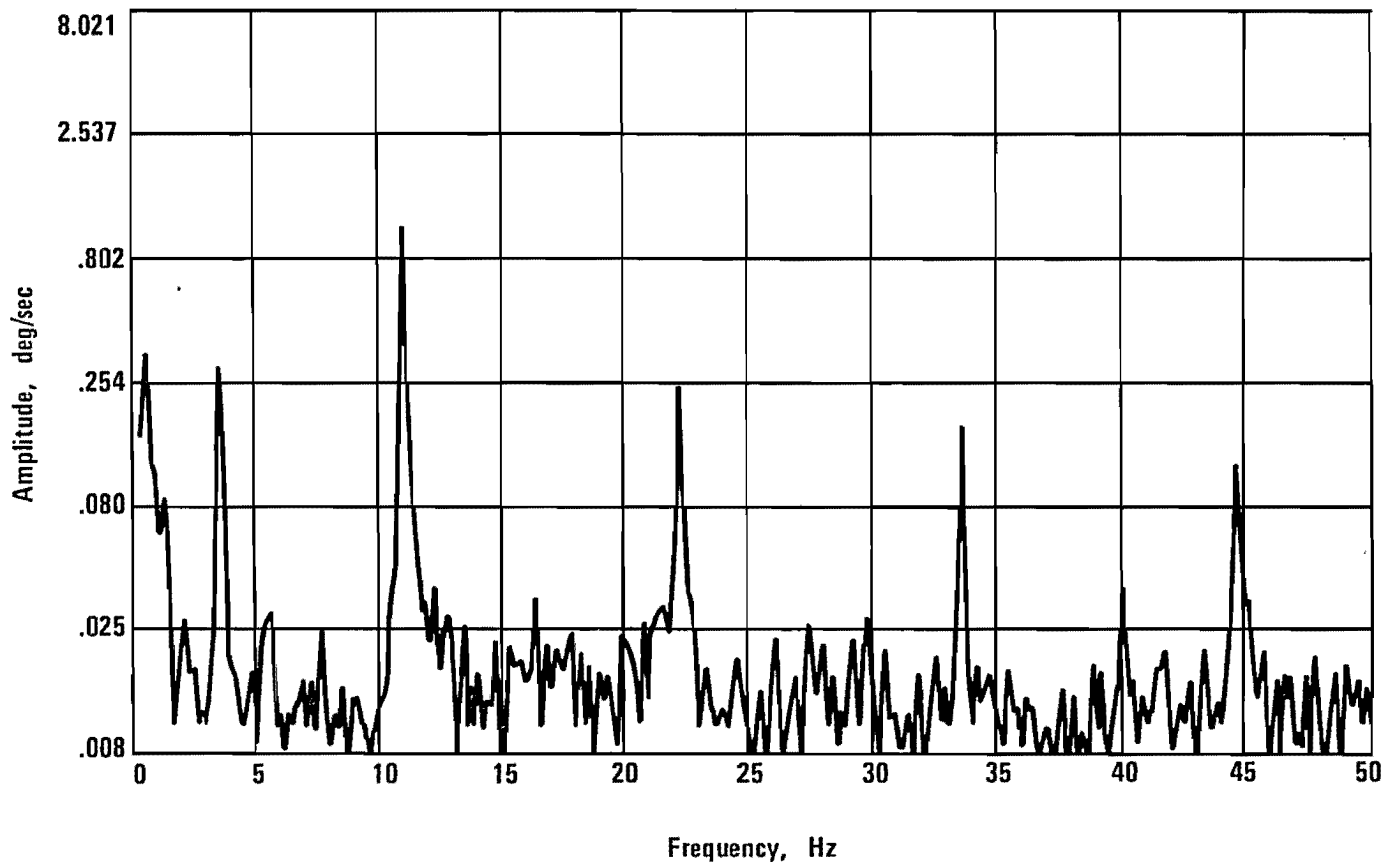

Figure 15. Roll Rate Spectral Analysis (Hover)

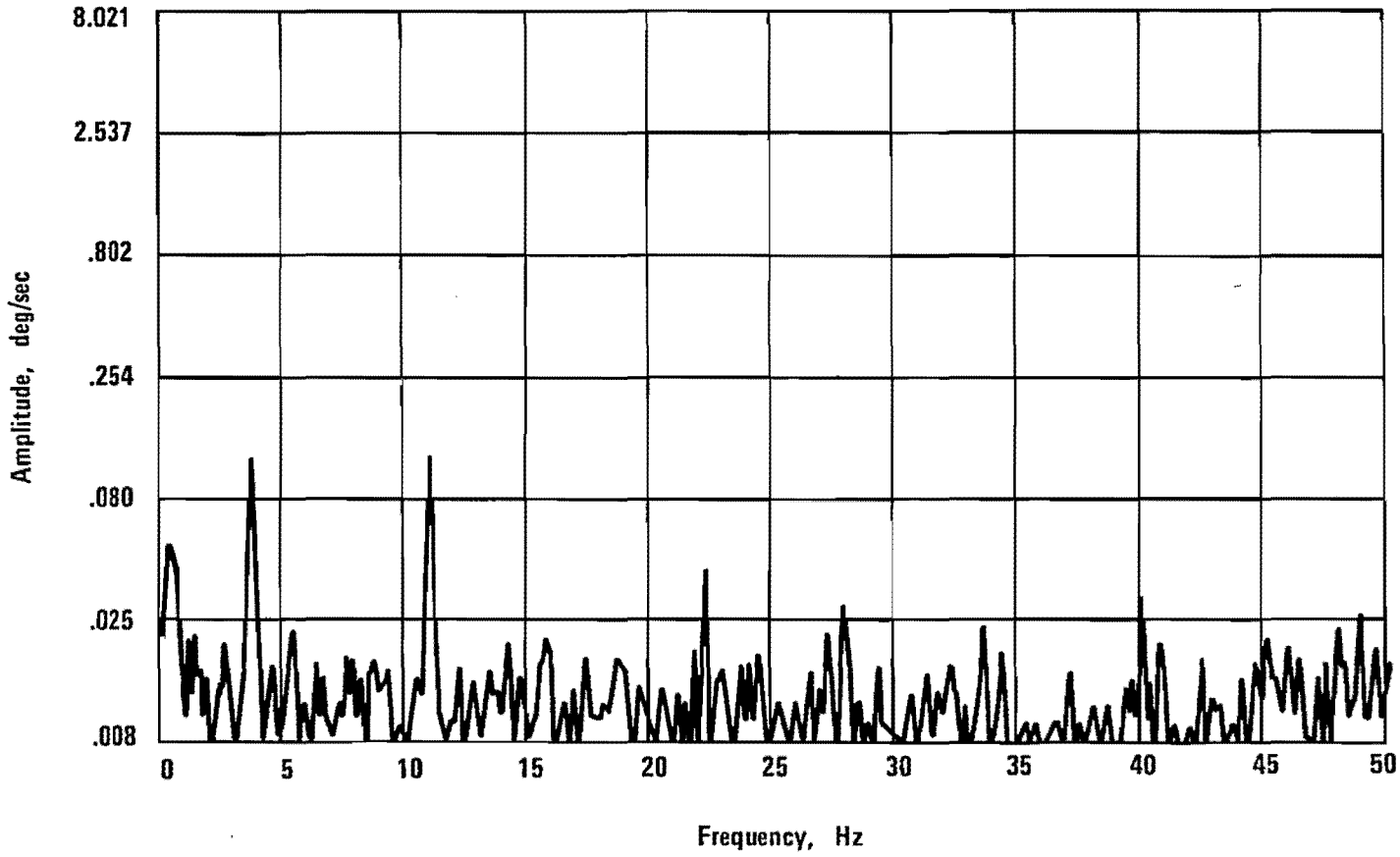

Figure 16. Yaw Rate Spectral Analysis (Hover)

The sensor model used for transient response evaluations was a perfect sensor corrupted by one- and three-per-rev sine waves of appropriate magnitude. This is described in Figure 17.

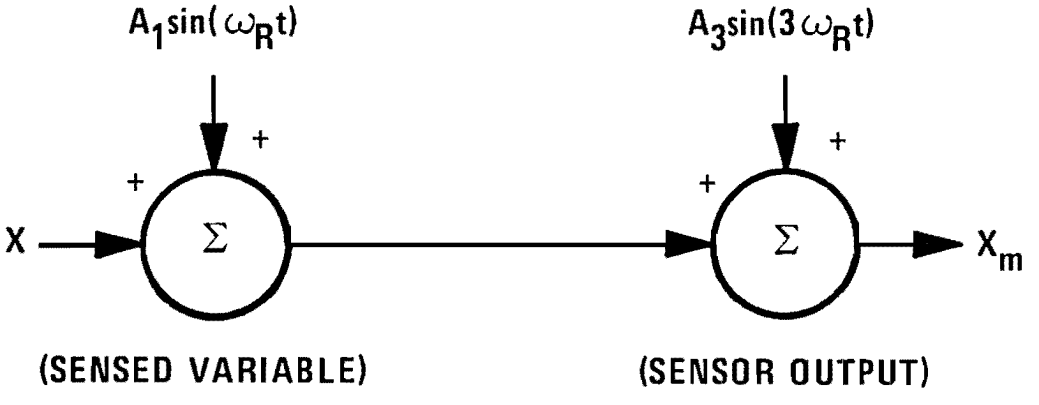

ω_R = 24 rad/sec

SENSED VARIABLE (X)	A_1	A_3
p	.0054	.0187
q	.0011	.0044
r	.0021	.0021

Figure 17. Rate Gyro Sensor Models

SECTION 3

CONTROL DESIGN

Design Objectives

The goals of this effort were to explore limitations to high gain control for the CH-47 vehicle and overcome these limitations where feasible within the constraints of the current hardware. The design is one which uses the current sensor complement and servo-actuation system. Additional designs which go beyond these constraints, such as rotor feedback and elimination of control nonlinearities and sensor noise, were explored for potential benefits.

Benefits

The primary benefit of high gain control is parameter insensitivity leading to simple control law modifications for numerous applications of model following. Figure 18 shows a simplified representation of this idea. If the controlled plant, represented by the multivariable series compensator $H_s(s)$, feedback compensator $H_p(s)$, and vehicle, performs consistently throughout the flight envelope, the feed forward model can be chosen with good predictability of results. Also, if the closed loop response of the plant is "fast" relative to the model, then the feed forward model becomes a lag compensator in the sense that the model will be replacing fast dynamics with slower dynamics.

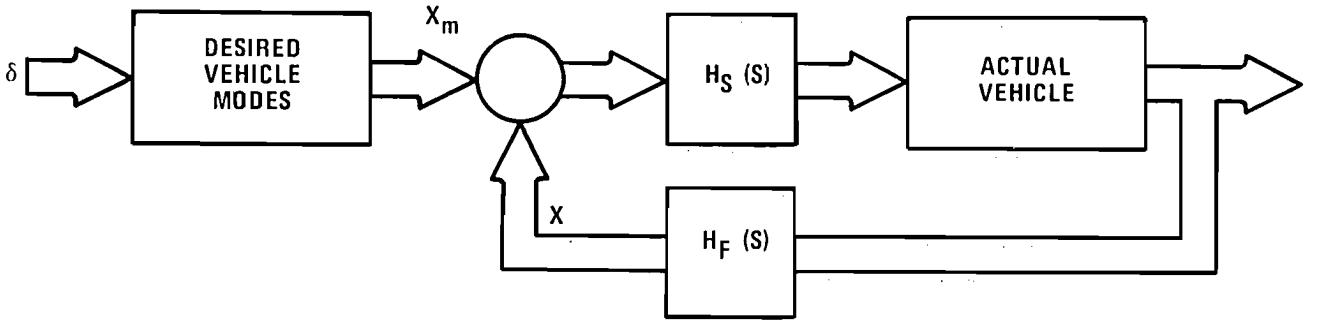

Figure 18. High Gain Model Following

The objective of this study is to design the high gain feedback controls to enable simple model design for model following. Therefore, the high gain design does not concentrate on the model itself but attacks the problem of designing a fast consistent response throughout the flight envelope.

Specific Design Goals

The specific design goals are to construct high bandwidth second-order responses for 1) the pitch rate/pitch angle pair in the longitudinal axis to a differential collective input and 2) roll rate/roll angle pair in the roll axis to a gang lateral cyclic input. Also, a high bandwidth first-order yaw rate response in the yaw axis to a differential lateral cyclic is considered. These goals are shown in Figure 19.

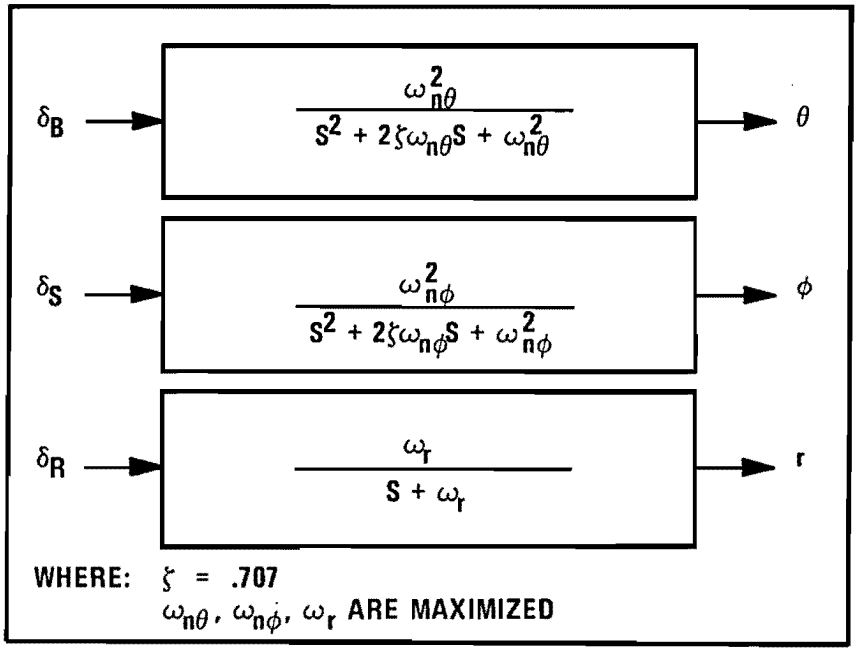

Figure 19. Control Response Design Goals

Modal Control Design Approach

Modal control design techniques, outlined in detail in Appendix B, have been used here because of the consistency with which one can achieve design specificity in the face of

- Higher order dynamics (rotors and actuators)
- Coupled dynamics, for example, roll and yaw
- Compensation, for example, proportional plus integral, notch filtering

Also, the multiple designs necessary to explore the maximum bandwidths dictate the use of an inexpensive computation tool. The modal control design

software is very fast, thereby producing desired results with minimal computer expenses. Furthermore, the design procedure makes use of only specified outputs and requires no post-design gain adjustments.

Compensation

Helicopters typically have vibration components at multiples of rotor frequencies. For the CH-47 the most important characteristics are high magnitude disturbances on sensors, with narrow frequency bands centered at the rotor governor frequency and integer multiples of the rotor governor frequency. Such disturbances do not effect the controller response of the vehicle until high gains are introduced. Initially, the servo-system responds because of its high bandwidth. Eventually, the rigid vehicle response is effected by the rate saturation of the ECS servo, causing a net reduction in ECS bandwidth which in turn lowers the rigid body response damping. Two types of compensation can be used to handle this:

- notch filtering
- complementary filtering

Notch Filters

Because the undesirable noise occurs at such precise frequencies, a very narrow deep notch filter can be used to effectively attenuate the noise and preserve loop phase close to the notch frequency.

Complementary Filtering

This concept has classically been utilized to combine sensors which contain information about a desired output in such a way as to attenuate individual sensor errors, including noise, and construct an output accurate over a broad range of frequency.

The concept examined here is based upon earlier work done by Garren and Niessen.[1] A description of how a complementary filter is used in a feedback path is shown in Figure 20.

Proportion Plus Integral Control

Control design in all axes includes proportional plus integral compensation. The benefits of using this type of series compensation are

- High gain is easily acquired at low frequencies.
- The pitch axis loop design contains a low frequency zero which if left uncompensated dominates the transient response, producing high overshoot. This can be correct by either proportional plus integral control (as performed here) or a control input feed forward which cancels the zero in question.
- Automatic trim adjustment results from proportional plus integral control.

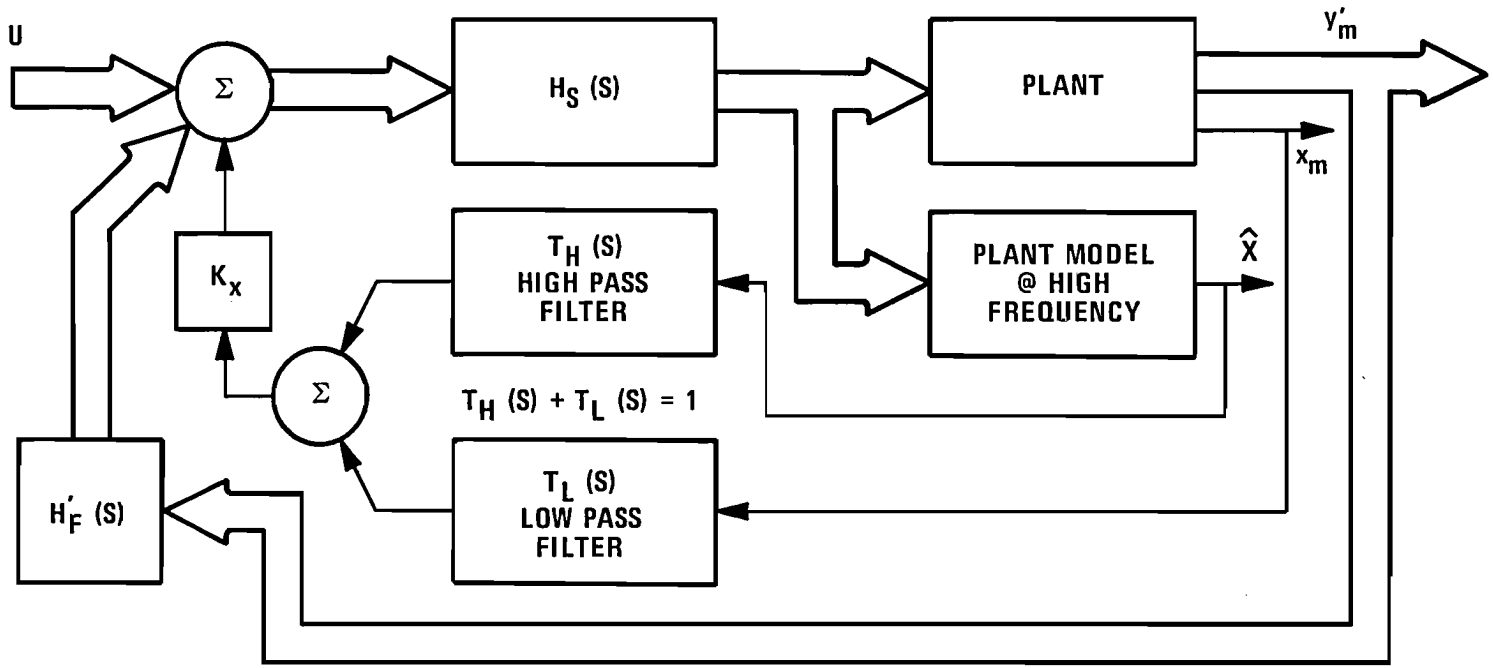

WHERE

H'_F (S) = COMPENSATION FOR MEASUREMENTS y'_m

y_m = ALL MEASUREMENTS EXCEPT x_m

K_x = GAIN FOR x FEEDBACK

x_m = MEASUREMENT OF OUTPUT, x, TO BE LOW PASSED

x = ESTIMATE OF OUTPUT, x, TO BE HIGH PASSED

u = CONTROL INPUT VECTOR

Figure 20. Complementary Filter Logic

Feedback Control Design Verification

Designs were verified using linear root locus techniques to establish dominant mode response for a given axis and assess the impact of all other system dynamics, including rotors, compensation, etc. Designs were also verified using step response simulation which included actuator nonlinearities, in other words, ECS rate limits and upper boost hysteresis. The simulation also included sensor noise spikes at one- and three-per-rev to test the effectiveness of notch and low-pass filtering. Results are discussed in the following sections.

Pitch Axis Design Results

High gain pitch axis control is achieved for various feedback arrangements for the differential collective. The following design concepts are based upon progressive constraint elimination.

1. Pitch angle, θ, and low-passed (@ 25 rad/sec) pitch rate, q to differential collective, δ_B. This case assumes current hardware complement, most important of which is the inclusion of rotor frequency pitch rate sensor noise. Also, upper boost hysteresis is examined.*

2. Pitch angle, θ, and nonfiltered pitch rate, q. Clean sensors and linear control hardware are assumed.

3. Clean θ and q plus front and rear rotor coning angle (β_{OF} and β_{OR}) feedback.

*As discussed later, the ECS rate limit is a severe constraint; however, this is more application-oriented, since the demands imposed by the input model greatly affect the impact of ECS rate limitations.

Finally, the gain scheduling of design #1 is analyzed to produce a consistent control throughout the flight envelope.

Pitch Angle--Low-Passed Pitch Rate Design

Using the modal control software, the design for the pitch axis was developed by increasing the desired pole placement demand natural frequency, ω_n, along a $\zeta = .707$ radial in the S-plane. This is shown in Figure 21.

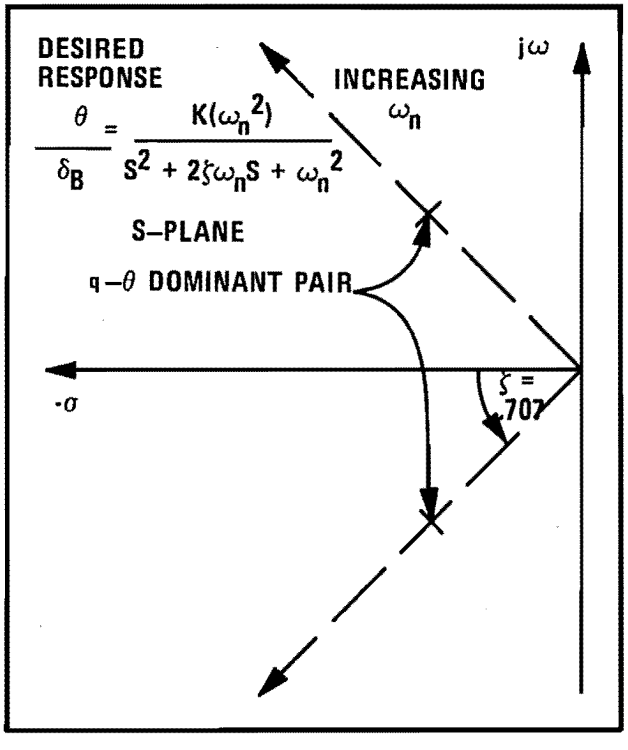

Figure 21. Pitch Axis Design Goal

This is a single input problem, in other words, differential collective (δ_B), and therefore only pole placement was possible using the modal control algorithm.* This produced no additional difficulties because the θ/δ_B transient response was dominated by the second-order root pair placed by the algorithm.

The first-order low-pass filter at 25 rad/sec on the pitch rate sensor distinguishes this design. The attenuation of the first and third rotor harmonic components of noise on the pitch rate sensor is thereby accomplished (see Figure 14).

As with all design cases in this report, a root locus plot of design options best presents the design results in terms of essential performance. Results for the low-pass pitch rate feedback case are summarized in Figure 5. Included in the figure are the dominant roots of the system. The entire axis has 13 modes: four rigid body, four rotor modes (coning only), four actuator modes, and the first-order low-pass mode. In this case, however, only five modes are needed to examine effective performance because others are either higher in frequency or effectively cancelled by zeros. Designs for desired natural frequencies from 3 to 8 rad/sec are included in Figure 22. As the placed pole pair moves higher in frequency, a single pole from higher frequency dynamics moves into a position of dominance. The optimal set appears to be at a frequency of approximately 5 rad/sec.

---

*As shown in Appendix B, eigenvector placement requires more than one control input.

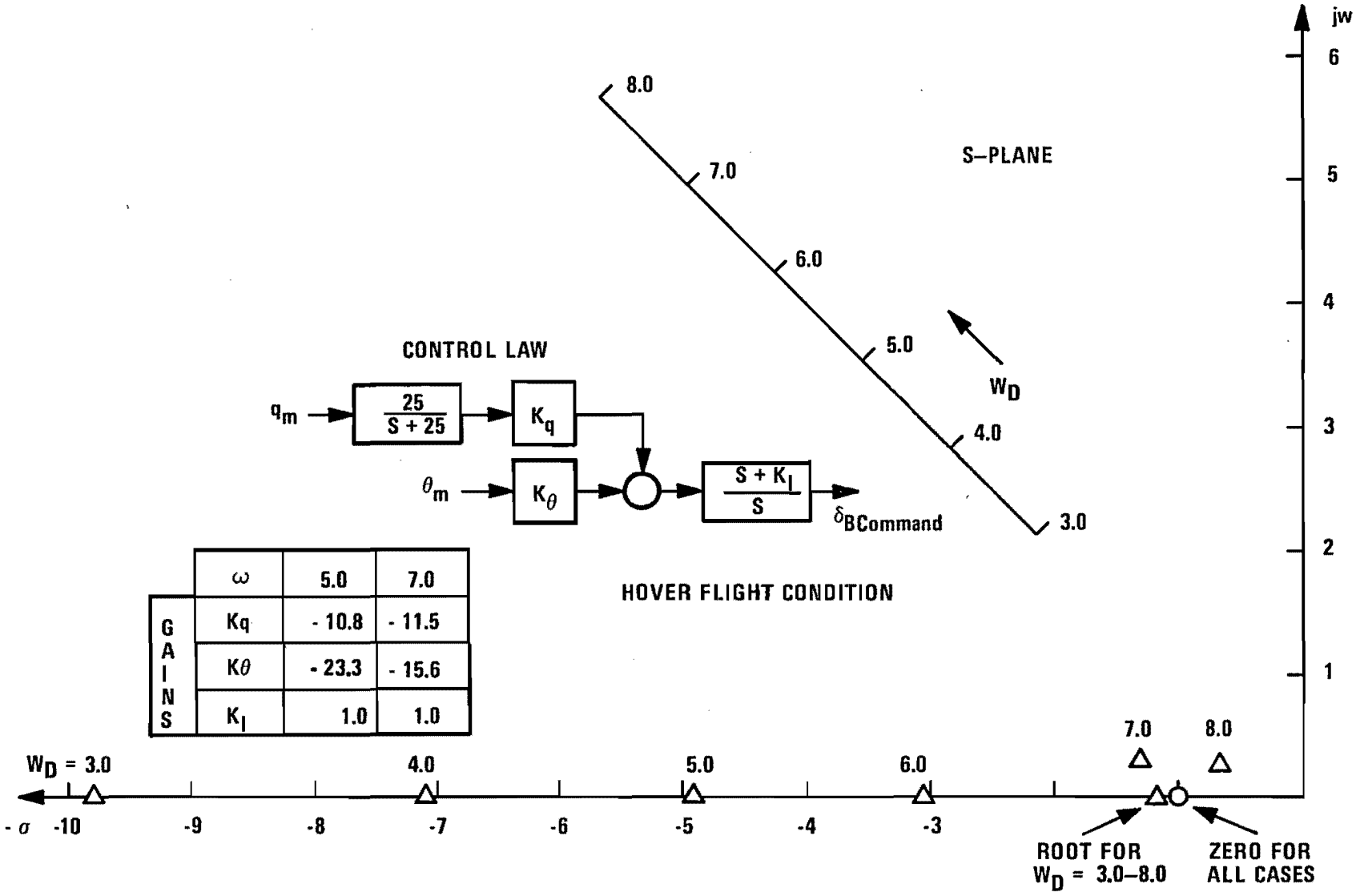

GAINS	ω	5.0	7.0
	Kq	- 10.8	- 11.5
	Kθ	- 23.3	- 15.6
	K_I	1.0	1.0

Figure 22. Pitch Axis Design Results, Low-Pass Filter

Transient response plots of two design cases tell a different story, resulting from the primary flight control system hysteresis (modeled as in Figure 12). Figures 23 and 24 contain differential collective step responses for two design cases. Figure 23 shows transient responses of various pitch axis dynamic states for the design case W_D = 5 rad/sec and the effect of the hysteresis on the performance.

Appendix C outlines the derivation of the hysteresis model used. The pitch axis, shown in Figure C-3, is by far the worst axis, as is evident from the fact that hangar tests on this axis produced significant backlash. In general, there are a number of ways to attack a problem like this:

1. Create a compensating nonlinearity in the loop to "cancel" the hysteresis. This approach is usually sensitive to changes in the fundamental nonlinearity.

2. Provide a high frequency input dithering signal to excite the actuator in the dead region, thus naturalizing its effect. This approach is commonly used; however, in this case the ECS rate limit also constrains us to keep the activity low. Indeed, an ideal dither signal already exists in the high frequency rotor noise anamolies on the rate gyros.

3. Redesign the control system to minimize hysteresis.

One solution which helps is to reduce the gain on the pitch attitude. This is shown in Figure 24. Our transient bandwidth is reduced, but the impact of the limit cycle is much lower. This design is shown in Figure 22 as W_D = 7.0 rad/sec. In addition to the placed root pair at W_D = 7.0, the response is also affected by the lower frequency roots shown. The net effect is a

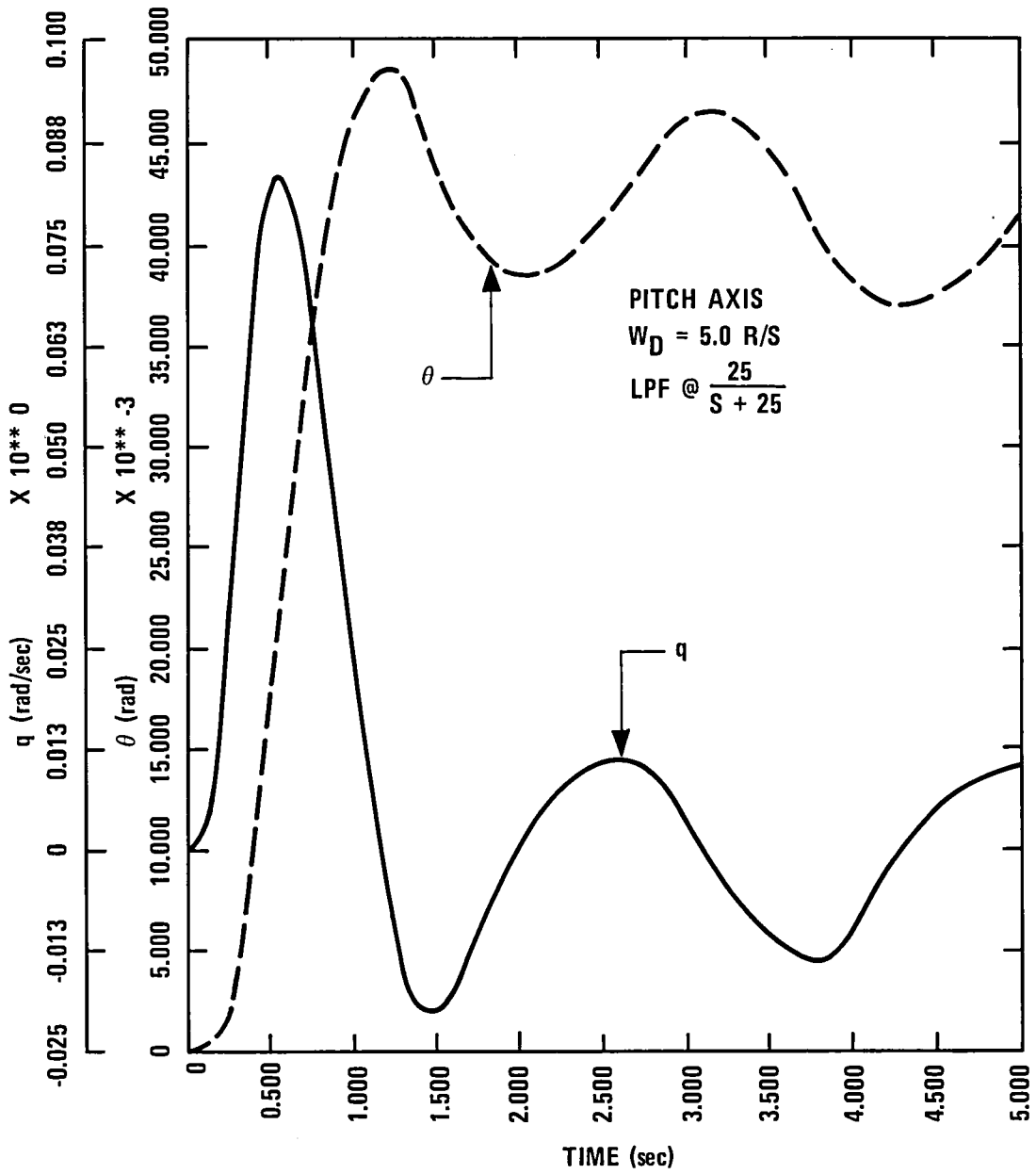

Figure 23. Pitch Axis Design W_D = 5.0 rad/sec

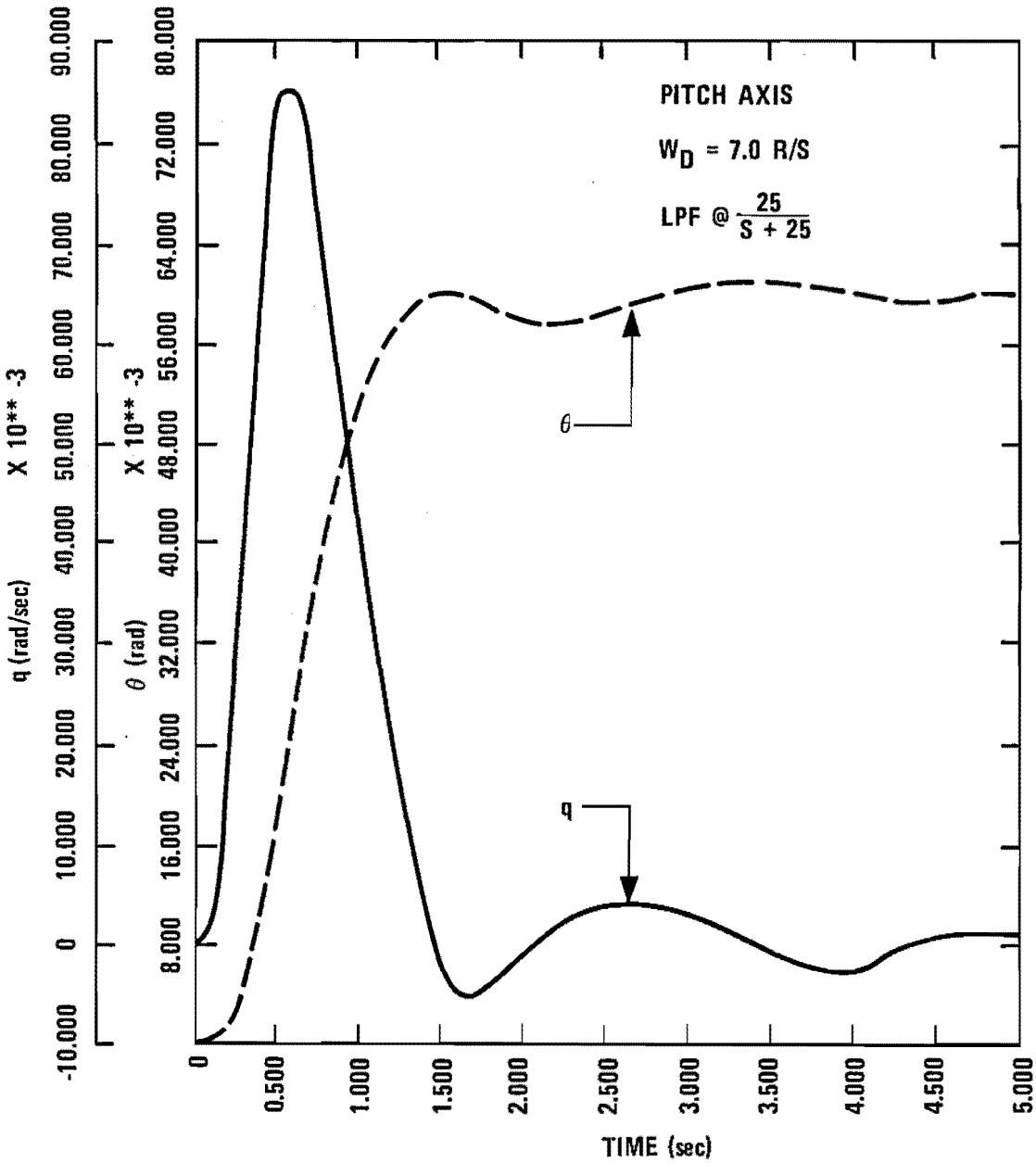

Figure 24. Pitch Axis Design W_D = 7.0 rad/sec

transient which displays characteristics of approximately 4.0 rad/sec in bandwidth and high damping.

A stability check of this latter design shows 10.4 dB gain margin and 46° phase margin. We have, therefore, a good design for vehicle implementation.

Pitch Axis Designs with Unfiltered Feedback

As discussed in the previous section, the control system hysteresis produced the fundamental limitation to high gain design in the pitch axis. The next limitation was imposed by the sensor noise at rotor frequencies, in other words, the requirement of low-pass filtering. The next design sequence is based upon two assumptions:

- Elimination of control nonlinearities, namely hysteresis
- Clean sensors

In Figure 25, the results of this design sequence are displayed. As the bandwidth demands increase, the system is increasingly dominated by a root excursion from higher frequency (originally part of a rotor pair). The design limit is $W_D = 8$ rad/sec. This is compared to $W_D \cong 4.0$ rad/sec for the hysteresis-dominated design and 5 rad/sec for the sensor noise-dominated design in which low-passed pitch rate was utilized.

Rotor Feedback

As demonstrated in Figure 25, the design limitation for high gains, assuming clean sensors and no hysteresis, was the rotor dynamics. Using the fourth-order coning model derived in Appendix A and the actuator dynamics, a rotor

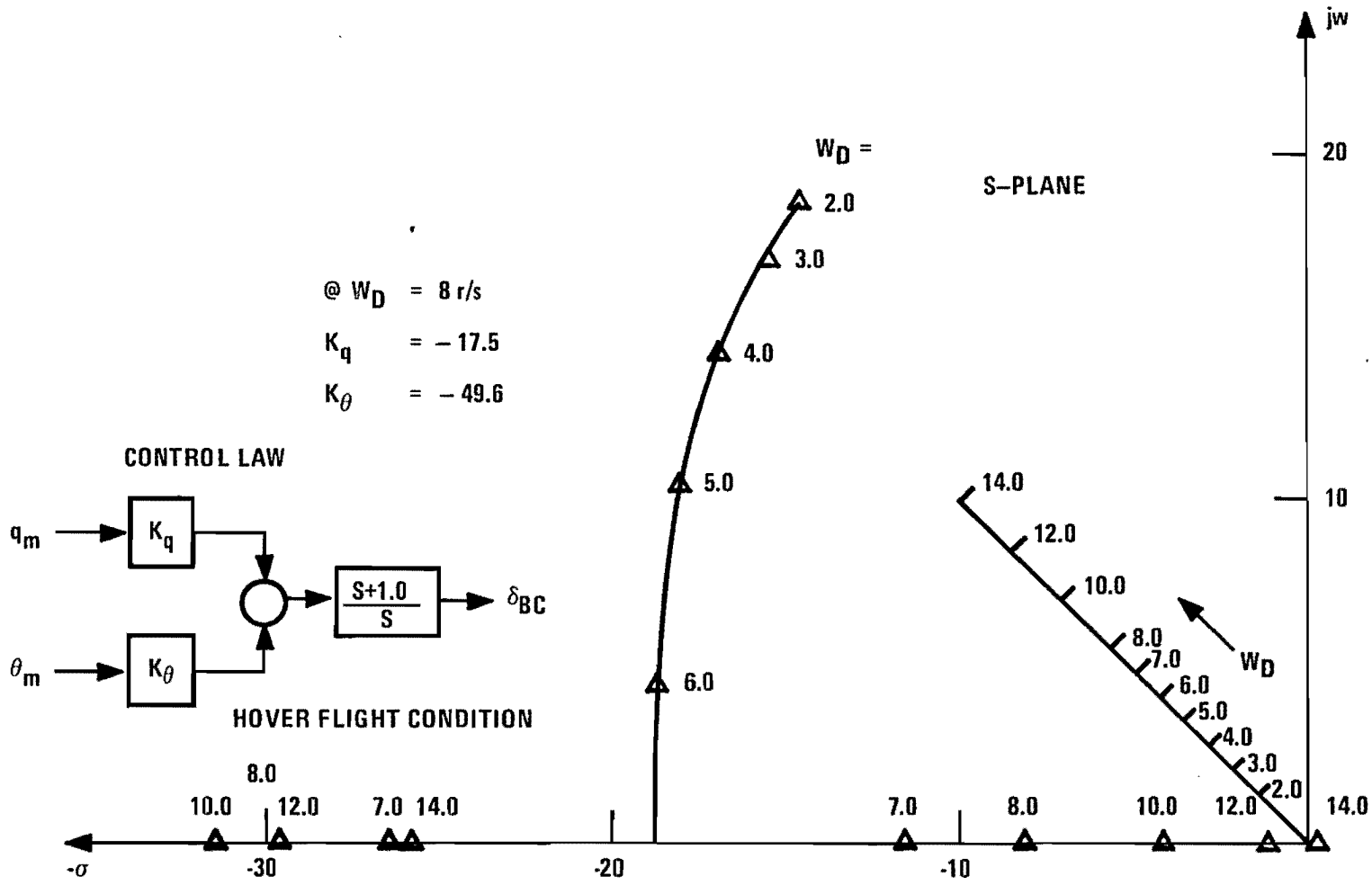

Figure 25. Pitch Axis Design Root Locus for Clean Sensors

feedback design was analyzed. As depicted in Figure 26, only two modes are observable. This is also demonstrated with the second-order coning model presented in Figure 11.

The feedback design of coning position states β_{OF} and β_{OR} was based upon moving the lowest frequency roots of the rotor dynamics, located in W_n = 24 rad/sec and ζ = .478, to a higher frequency. Within the linear constraints of the actuators, the lowest frequency attainable for the system of Figure 26 was W_n = 36 rad/sec with ζ = .7.

The rigid body pole placement algorithm was then used as before except that the open loop plant contained the rotor feedback design. Figure 27 contains the results of this effort. As can be seen, the maximum achievable bandwidth is between W_D = 11 rad/sec and 12 rad/sec.

Lateral-Directional Axes Design Results

Roll and yaw control designs were analyzed using the coupled lateral-directional rigid body dynamics of the CH-47B. High gain control designs were emphasized for the roll axis; however, increased demands upon the yaw rate response were also imposed. As with the pitch axis, the lateral-directional axes design sequence proceeded along a similar scenario.

1. Roll rate, p, yaw rate, r, and roll angle, ϕ, measurements were fed back to lateral cyclic, δS, and differential cyclic, δR. Current actuation hardware, including rate limits and hysteresis models, is assumed. Rotor frequency sensor noise was included on roll rate and yaw rate outputs.

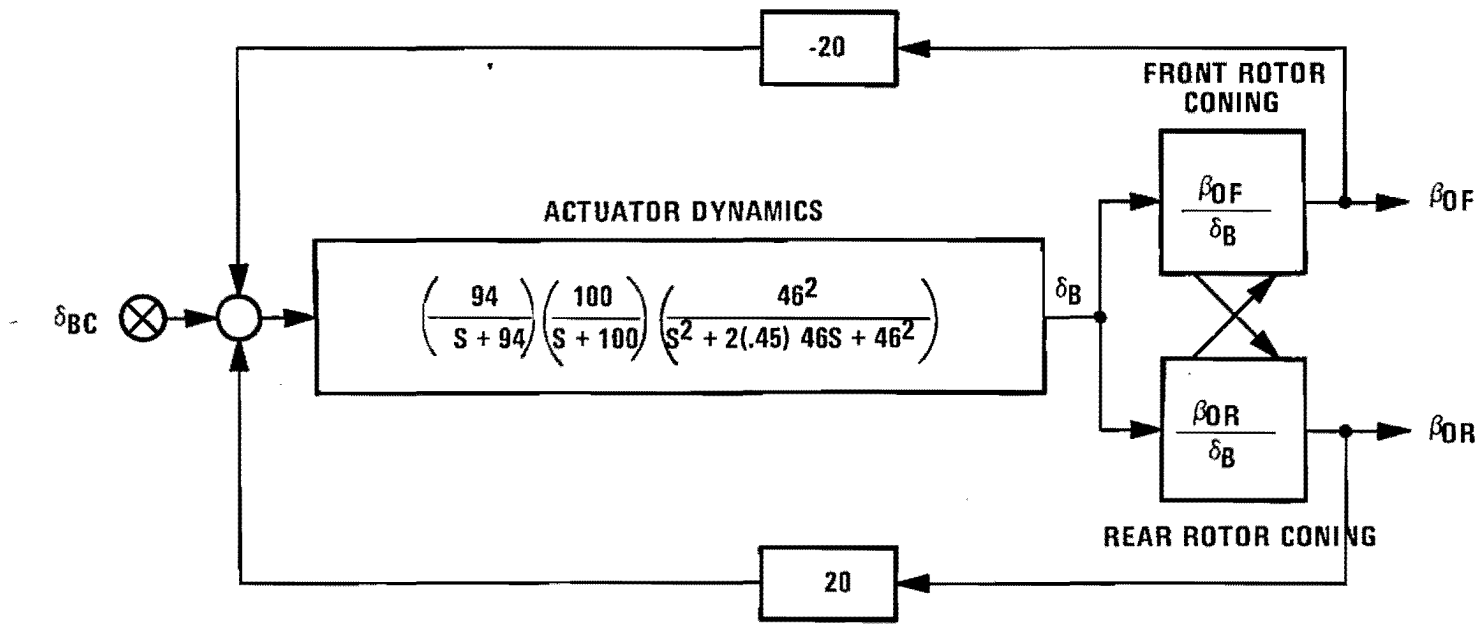

$$\frac{{}^{*}\beta_{OR}}{\delta_B} = -\frac{\beta_{OR}}{\delta_B}$$

Figure 26. Pitch Axis Rotor Feedback Implementation

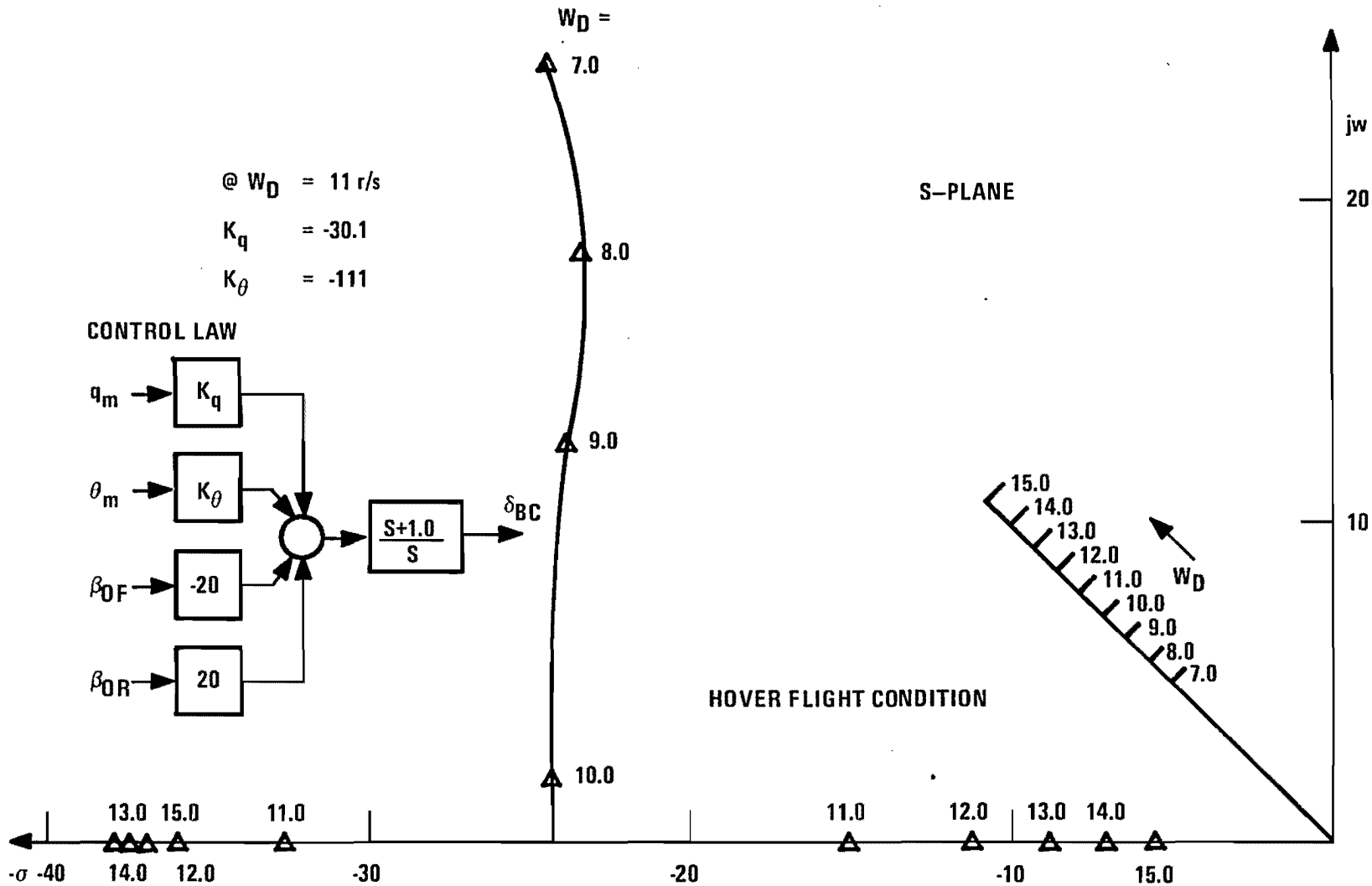

Figure 27. Pitch Axis Design with Rotor Feedback

2. Unfiltered sensors for p, r, ϕ. Clean sensors and linear hardware are assumed.

3. p, r, ϕ, plus front and rear rotor lateral flap angles (β_{SF} and β_{SR}) are fed back.

Finally, gain scheduling implications of design #1 are examined.

Langley Complementary Filter

As briefly outlined earlier, NASA Langley[1] has developed a unique approach to the high gain control problem. When sensor noise attenuation dominates the problem, as it does in the roll axis, the use of a "complementary" filter in the feedback loop yields good transient and noise rejection results. Figure 28 shows the specific arrangement of the NASA design outlined in general terms in Figure 20.

This filter was examined here for its consistency of response for various choices of the high- and low-pass filter break frequency, W_c. Figure 29 shows a root locus of dominant poles for the roll axis for three choices of W_c. These results verify earlier flight test results[1] which indicate similar loop responses for a similar range of W_c values.

A typical roll stick transient is shown in Figure 30. The low frequency departure of the high frequency roll rate estimate, $\hat{P}$, from the actual roll rate value, p, is indicative of the high-pass/low-pass nature of the design.

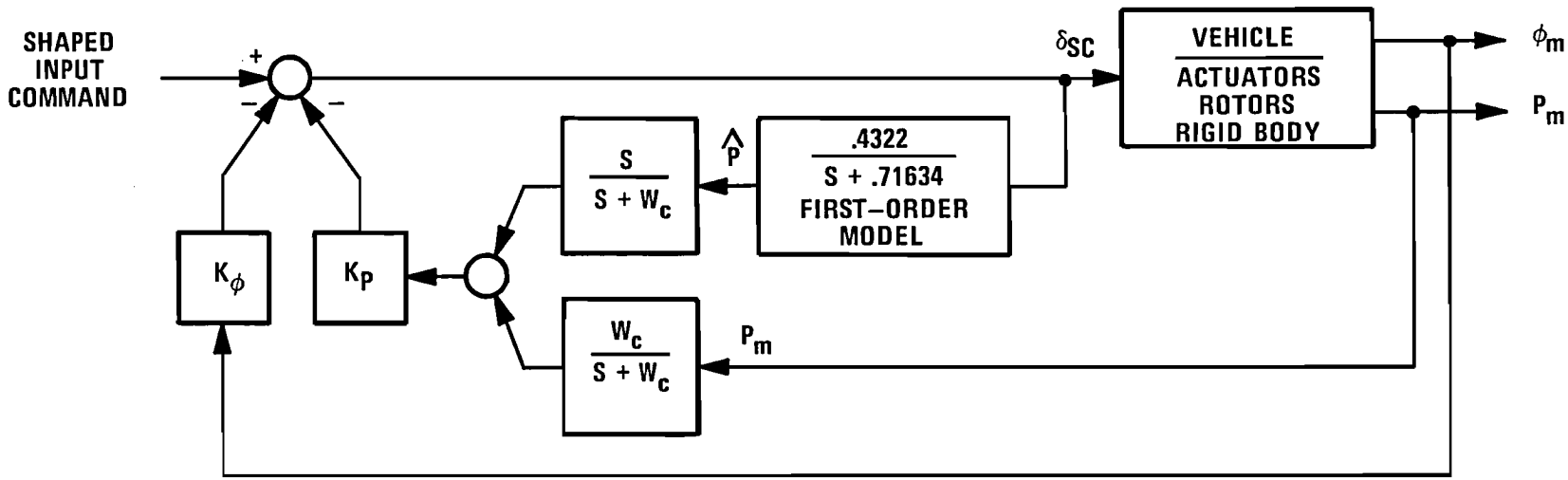

Figure 28. Langley Complementary Filter[1]

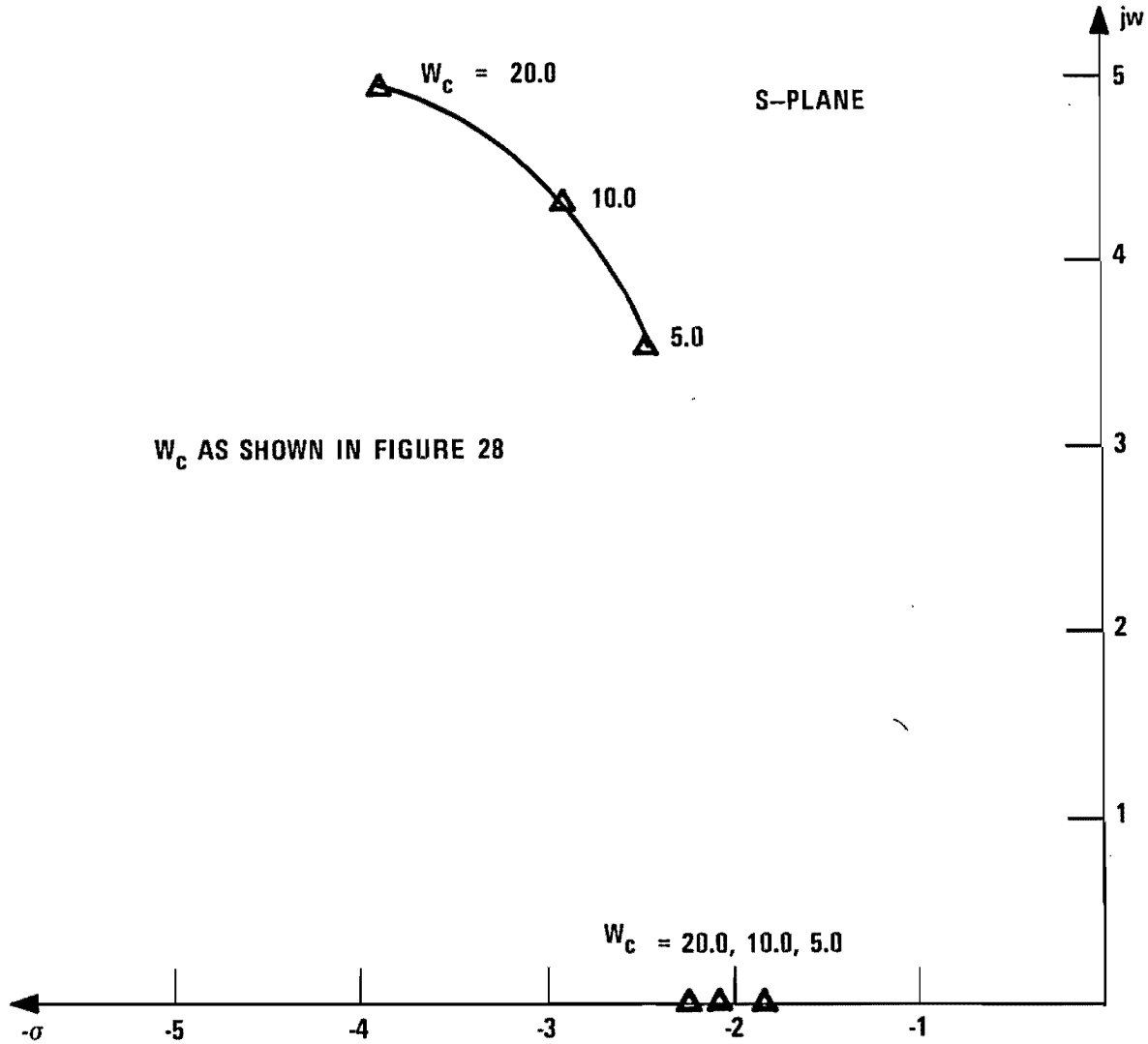

Figure 29. Complementary Filter Root Locus Versus W_c

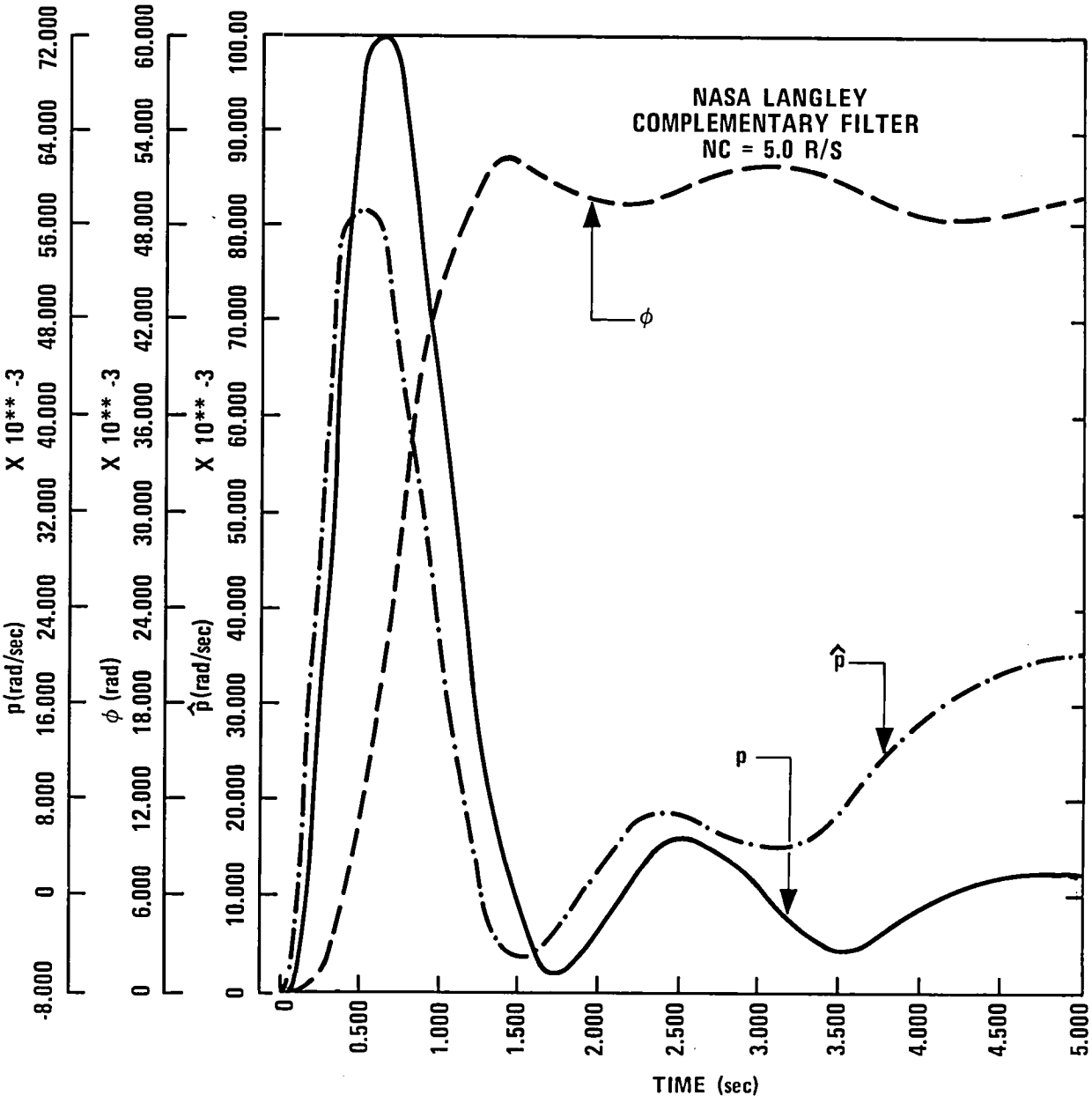

Figure 30. Complementary Filter Response to Step δ_R

Filtered Roll Rate Design

The problem attacked by the complementary filter is the same one presented in the current study, namely, attenuation of the one- and three-per-rev sensor noises. The roll rate gyro presents the biggest problem in this regard, because these noises, as shown in Figure 15, have the highest magnitudes of all the gyros (Figures 14 and 16 for pitch rate and yaw rate, respectively).

The approach taken here is to attenuate these noises as much as possible and retain as broad a spectrum as possible of the sensor's output. The guideline for choosing the appropriate filter feedback combination is to limit the amount of sensor noise which is passed to the actuators. This limit was chosen to be less than or equal to the noise which passed through the complementary filter. The following filter provided this attenuation while maintaining a broad band of roll rate.

$$TFC(s) = \left(\frac{S^2 + 24^2}{S^2 + 2(.1)\,24S + 24^2}\right) \left(\frac{S^2 + 72^2}{S^2 + 2(.1)\,72S + 72^2}\right) \left(\frac{60}{S + 60}\right)$$

The filter is composed of two narrow deep notch filters at one- and three-per-rev frequencies and a low-pass at 60 rad/sec. A 20 rad/sec low-pass was also applied to the yaw rate gyro.

Modal control design was then applied to the filtered sensors. Because there are two controls, in this case, eigenvector placement can be performed. Figure 31 shows a selected set of eigenvectors for a typical design case.

As outlined in Appendix B, the desired state responses are indicated by the "1.0" elements and the responses to be eliminated are indicated by the "0.0"

DESIRED

ROLL: $\lambda_{1,2} = -2.8284 \pm j2.8284$ YAW: $\lambda_3 = -4.0$

VPRO_ROTOR_ACTUATOR_COMP	REAL	COMPLEX	REAL
1	-1.0000E 00*	-1.0000E 00	-1.0000E 00
2	1.0000E 00	-1.0000E 00	0.
3	0.	0.	1.0000E 00
4	-1.0000E 00	1.0000E 00	0.
5	-1.0000E 00	-1.0000E 00	-1.0000E 00
6	-1.0000E 00	-1.0000E 00	-1.0000E 00
7	-1.0000E 00	-1.0000E 00	-1.0000E 00
8	-1.0000E 00	-1.0000E 00	-1.0000E 00
9	-1.0000E 00	-1.0000E 00	-1.0000E 00
10	-1.0000E 00	-1.0000E 00	-1.0000E 00
11	-1.0000E 00	-1.0000E 00	-1.0000E 00
12	-1.0000E 00	-1.0000E 00	-1.0000E 00
13	-1.0000E 00	-1.0000E 00	-1.0000E 00
14	-1.0000E 00	-1.0000E 00	-1.0000E 00
15	-1.0000E 00	-1.0000E 00	-1.0000E 00
16	-1.0000E 00	-1.0000E 00	-1.0000E 00
17	-1.0000E 00	-1.0000E 00	-1.0000E 00
18	-1.0000E 00	-1.0000E 00	-1.0000E 00
19	-1.0000E 00	-1.0000E 00	-1.0000E 00
20	-1.0000E 00	-1.0000E 00	-1.0000E 00
21	-1.0000E 00	-1.0000E 00	-1.0000E 00
22	-1.0000E 00	-1.0000E 00	-1.0000E 00
23	-1.0000E 00	-1.0000E 00	-1.0000E 00
24	-1.0000E 00	-1.0000E 00	-1.0000E 00
25	-1.0000E 00	-1.0000E 00	-1.0000E 00
26	-1.0000E 00	-1.0000E 00	-1.0000E 00
27	-1.0000E 00	-1.0000E 00	-1.0000E 00

ACHIEVED

ROLL: $\lambda_{1,2} = -2.8284 \pm j2.8284$ YAW: $\lambda_3 = -4.0$

	REAL	COMPLEX	REAL
1	1.6666E 01	-1.0572E 01	5.5872E-01
2	1.0000E 00	-6.6569E 00	-6.8144E-03
3	1.8626E-09	0.	9.9921E-01
4	-1.3536E 00	1.0000E 00	-2.7258E-02
5	-1.4008E-01	-2.4949E-01	2.2704E-01
6	1.1019E 00	3.0946E-01	-9.0817E-01
7	8.3102E-01	6.4281E-01	-1.4208E 00
8	-4.1686E 00	5.3234E-01	5.6833E 00
9	3.6703E-01	1.6416E-01	1.8320E-01
10	-1.5024E 00	5.7380E-01	-7.3279E-01
11	1.9764E 00	1.7679E 00	1.2253E 00
12	-1.0590E 01	5.8964E-01	-4.9014E 00
13	2.0821E 01	3.5247E 01	-1.8122E 00
14	2.2464E 01	3.5619E 01	-1.8977E 00
15	-1.7574E 02	-3.0093E 01	8.1506E 00
16	2.5746E 01	3.6386E 01	-2.0377E 00
17	-4.2862E 00	-9.2705E 00	-1.4173E 01
18	-4.6847E 00	-9.4039E 00	-1.4764E 01
19	4.3944E 01	1.1372E 01	6.5358E 01
20	-5.7581E 00	-9.7786E 00	-1.6340E 01
21	5.5963E 00	-1.0383E 01	5.7835E-01
22	1.3970E-09	0.	1.2490E 00
23	4.9739E-01	-7.2692E 00	-7.6304E-03
24	1.8290E-03	-1.1828E-02	-1.1897E-05
25	2.8282E-02	3.8628E-02	4.7586E-05
26	1.6163E-04	-1.3311E-03	-1.3696E-06
27	3.3078E-03	4.2221E-03	5.4782E-06

* -1.000 MEANS THAT THE ELEMENT PLACEMENT IS ARBITRARY

Figure 31. Eigenvalue-Eigenvector Placement Technique

elements. The "-1.0" are coded by the algorithm to indicate arbitrary eigenvector mode responses. Pole placement is guaranteed, but eigenvector admissability is not. Comparing the left side of Figure 31 with the right indicates that our desires are met, on the whole.

Figure 32 is a root locus of the eigensystem placement exercise for the filtered rate gyro cases. As with the pitch axis design sequences, the bandwidth expansion proceeds until a higher frequency root excursion moves into a position of dominance. In this case, this occurs between 4.0 and 5.0 rad/sec natural frequency. A higher limit on yaw rate could be obtained but this was not explored further.

The control law for the W_D = 5 rad/sec case is shown in Figure 33. A lateral cyclic, δs, step input transient is shown in Figure 34 to verify the second-order response of the roll attitude. Some hysteresis limit cycling occurs but this is much smaller than observed in the pitch axis, as expected. Also, a comparison of Figure 34 with the complementary filter transient of Figure 30 demonstrates only a slight improvement with the current design. Figure 35 demonstrates the first-order shape of the yaw rate response for a step differential cyclic, δR, input.

Lateral-Direction Design Without Filtering

In order to gain some perspective as to the losses due to filtering and explore higher gains based upon more idealized hardware, that is, clean sensors, bandwidth expansion designs were conducted without sensor filters.

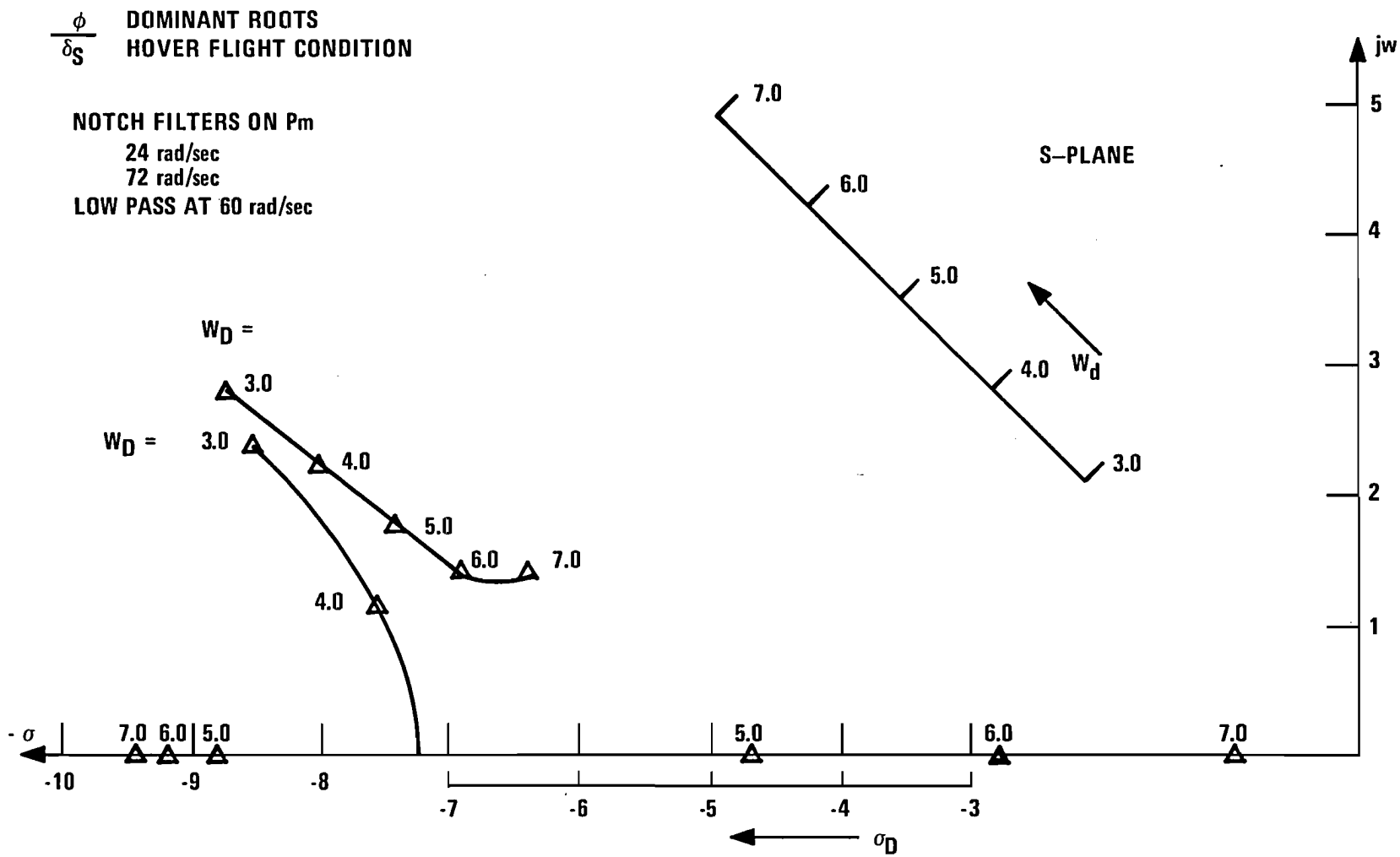

Figure 32. Roll Axis Root Locus, Filter Rate Gyros

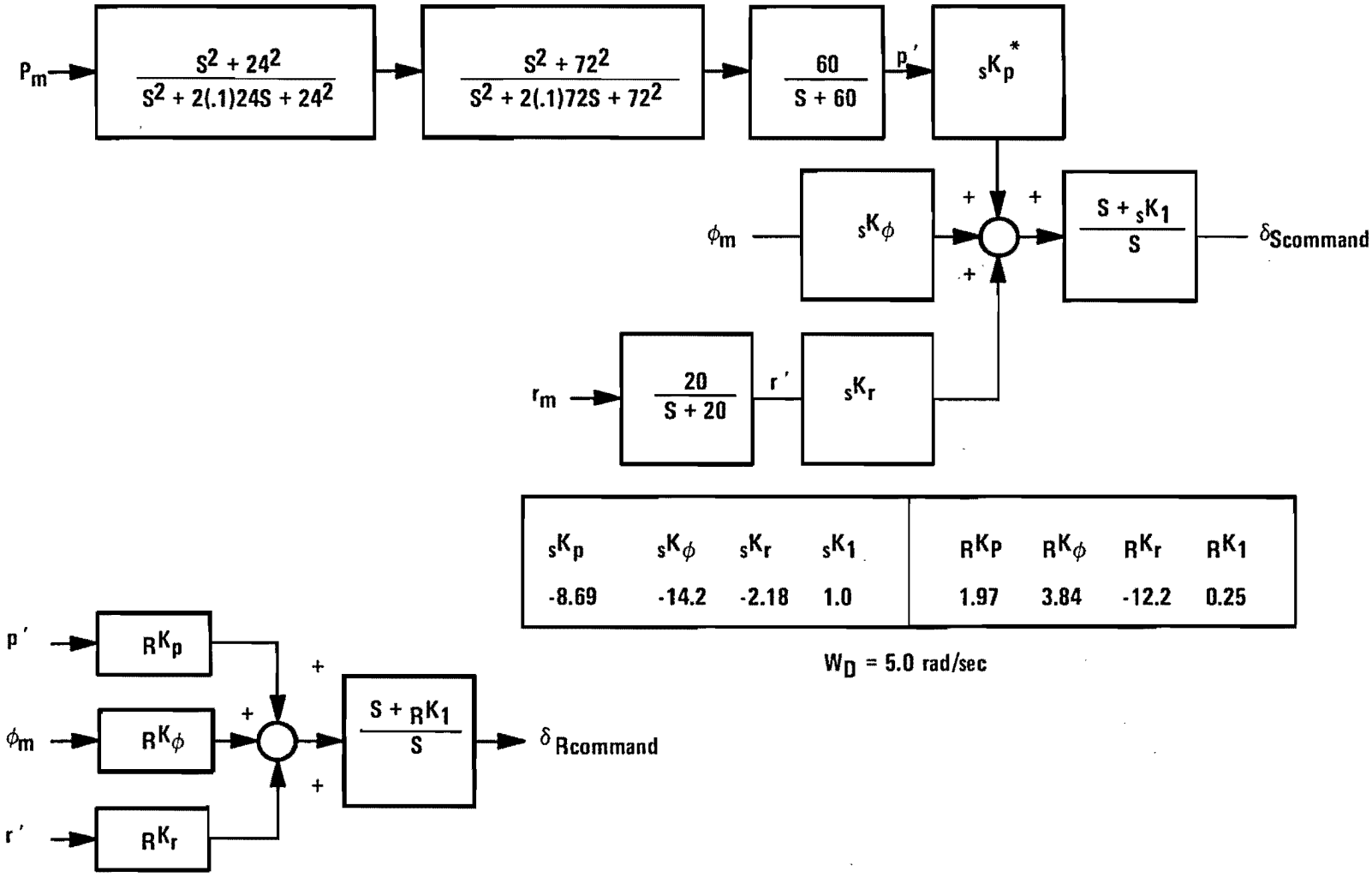

${}_sK_p$	${}_sK_\phi$	${}_sK_r$	${}_sK_1$	${}_RK_p$	${}_RK_\phi$	${}_RK_r$	${}_RK_1$
-8.69	-14.2	-2.18	1.0	1.97	3.84	-12.2	0.25

W_D = 5.0 rad/sec

${}^*{}_xK_g \triangleq$ GAIN FROM INPUT g TO OUTPUT x

Figure 33. Lateral-Directional Control Laws, Hover Flight Condition

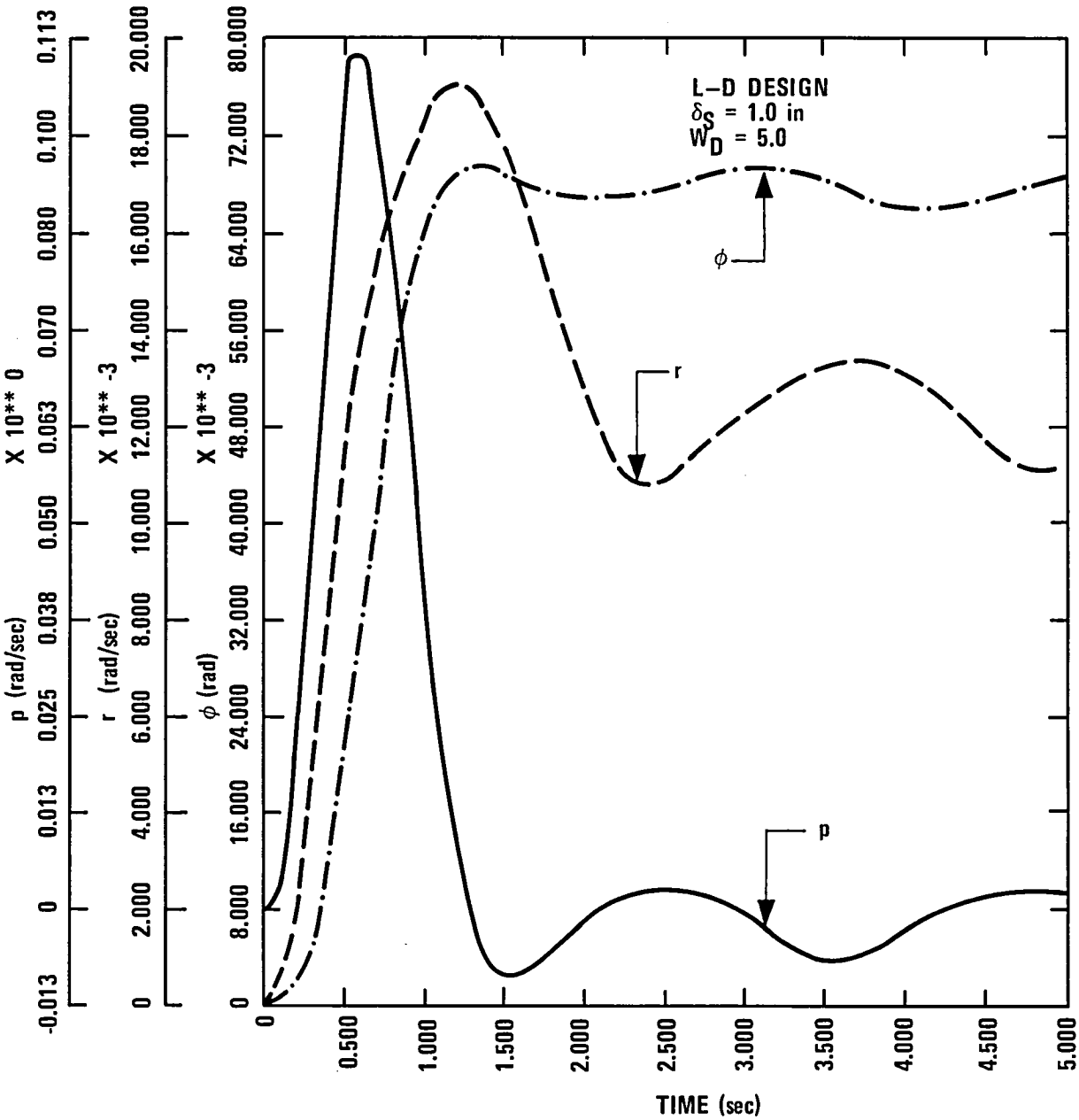

Figure 34. Roll Transient Response, Filtered Rate Gyros

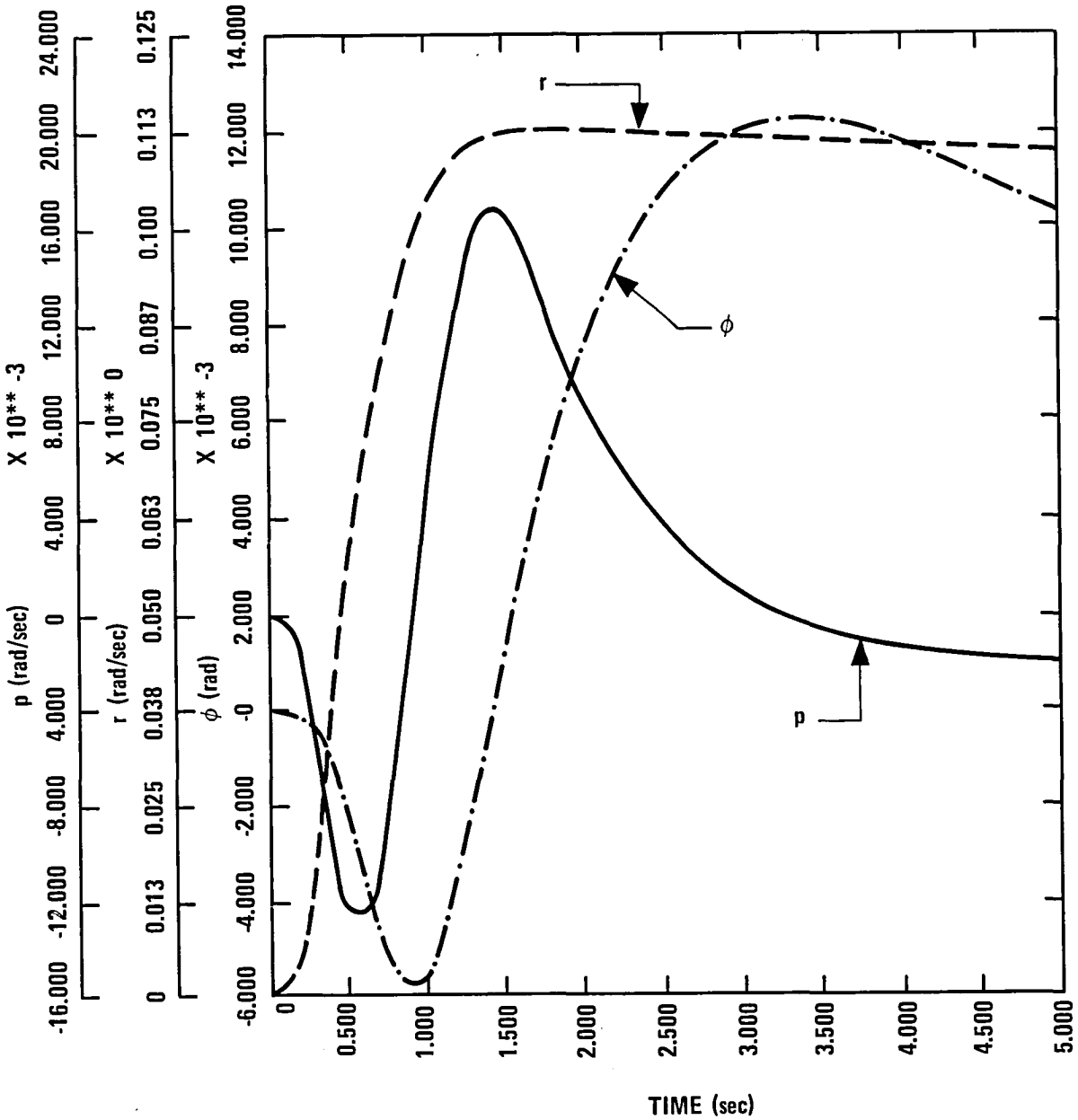

Figure 35. Yaw Rate Transient Response, Filtered Rate Gyros

Figure 36. shows the results for this sequence. The extra sensor band allows the closed loop bandwidth to increase to a "p-ϕ" closed loop natural frequency of 7.0 rad/sec before troublesome root excursions from higher frequency start to dominate.

Rotor Feedback

Using rotor feedback to lateral cyclic demonstrated some additional bandwidth benefits. Using rotor dynamics derived in Appendix A with the lateral cyclic actuator model, a successful design was performed. As shown in Figure 37, the use of rotor feedback allowed the "P-ϕ" root pair to achieve a 10 rad/sec natural frequency.

Finally, the gain values listed in Figure 37 are extremely high from a sensor noise standpoint. Since no post-design gain sensitivity was performed one can only conjecture that some may be arbitrarily high; however, most of those listed gains are much larger than those without rotor feedback, as was true for the pitch axis design with rotor feedback.

Gain Scheduling

The filtered designs for longitudinal and lateral directional axes were examined at forward speeds from -20.5 to 61.77 m/s (-40 to +120 kn) at zero vertical speed and -10.16 m/s (-2000 ft/min) to + 10.16 m/s (+2000 ft/min) at zero forward speed. The modal control software produced very similar gains to the hover condition, thereby raising the possibility of a constant gain system.

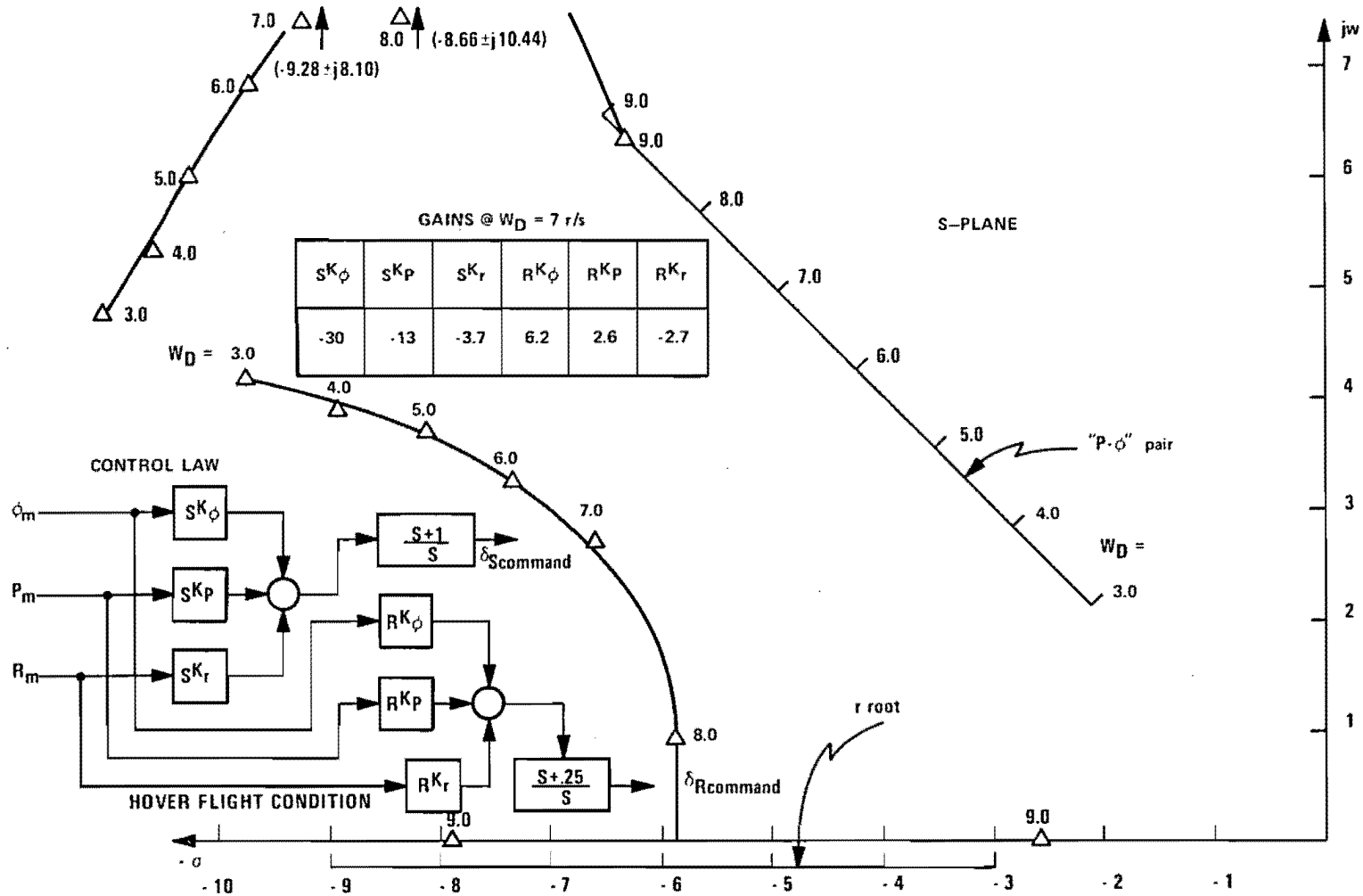

Figure 36. Lateral-Directional Root Locus, Clean Sensors

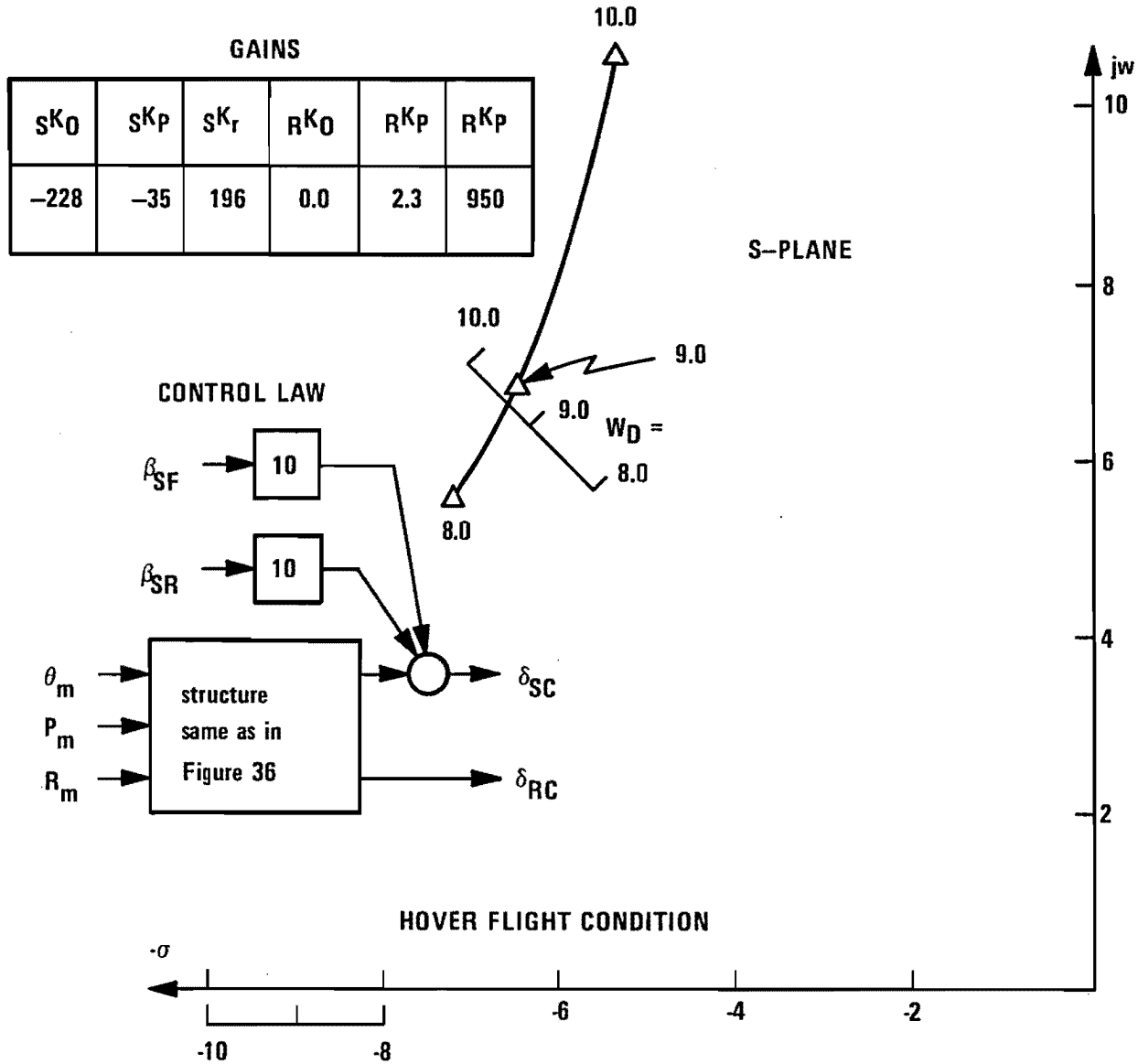

Figure 37. Lateral-Directional Root Locus, Rotor Feedback

Two difficulties with the transient responses surfaced:

1. At extreme forward speeds (both negative and positive) the pitch axis response overshoot increased from approximately 13% at hover to over 20%. This was corrected by increasing the integral gain in the pitch loop. A schedule on the integral gain with airspeed would be in order.

2. At extreme negative vertical speeds the yaw rate response did not return to steady state within a reasonable time. Here the solution was to increase the yaw rate integral gain, thereby suggesting a schedule for this parameter.

SECTION 4

SUMMARY AND CONCLUSIONS

The prospect of high gain benefits must always be tempered with hard reality. The approach taken was one of looking at a hierarchy of constraints beginning with those that exist, eliminating them one by one, and assessing the benefits. If a given limitation was solvable with the current hardware, the appropriate recommendation (such as compensation) was made.

Other limitations involved characteristics or anomolies not likely to be removed easily. For example, sensor noise spikes are a fact of life for this set of hardware. The approach here was simply to legislate away the problem and examine the benefits of doing so.

Modeling

Modeling was a major program task. Rigid body data was supplied at the outset in high quality form.[2] Conclusions about other models developed on the contract are:

- Actuator Models
  - The CH-47 boost actuators have considerable bandwidth, sufficient for all cases studied. Control system hysteresis posed difficulties in design performance, particularly the pitch design, where this nonlinearity ultimately became the bandwidth limiting factor.

- The ECS rate limit was not identified as a limiting factor in this study; however, this limit has the potential to impact the performance of all research system designs. This limit would greatly effect the response time if saturated. But more important, the system can go unstable if sufficient saturation is achieved. It is suggested that either this limit be increased or feed forward designs be constructed to avoid excessive ECS rate excitation.

- Rotor Models
  - Good models for transfer function representation for first harmonic flapping modes were derived with minimum realization. A second-order "notch filter" type coning model and similar fourth-order representations for lateral cyclic were derived. These demonstrate little parameter variation throughout the flight envelope.
  - Expansion of rotor models would logically include higher frequency flapping harmonic (three-per-rev) and lagging. This effect, however, should be preceded by more attention to unmodelled lower frequency dynamics such as the first body torsional mode.
  - Completely coupled state space representation of the first flapping mode was useful for rotor state feedback designs. Utilization of the reduced order transfer function realizations was not tried, but the use of similarly derived transfer relations from control inputs to flap states should also be successful.

Control Designs

Control designs were based upon placing increased bandwidth demands upon a given set of assumed dynamics and finding the maximum possible bandwidth for a given axis (pitch and roll/yaw). Using second-order responses for pitch and roll as a guideline, the designs proceeded along damping ratio = .707 radials in the S-plane. A summary of the limits found is shown in Table 1.

The roll/yaw axes design was compared with the NASA complementary filter.[1] The conclusion here is that for the specific noise rejection problem which dominates the roll axis the complementary filter is a much simpler alternative and transient performance was equal to the current design.

Finally, the use of modal control design techniques leads to some conclusions about this tool. Of the existing "modern" control design tools the one used here demonstrated the best facility for

- producing practical, implementable designs without post-design gain changing and/or observer construction
- conserving the computer budget by being computationally efficient
- allowing one to input design goals that make sense; in other words, eigenvalue-eigenvector placement has direct relationships with classical design specifications.

TABLE 1. HIGH GAIN CONTROL** DESIGN RESULTS

Axis	Controls Used	Sensors Used	Design Criteria	Assumptions	Filtering	Bandwidth Limit	Reason for Limit
Pitch	δ_B	q, θ	2nd-order q-θ response	-Nonlinear actuators -Noisy sensors	q filter = $\frac{25}{S+25}$	4.0 rad/sec	Upper boost hysteresis
Pitch	δ_B	q, θ	2nd-order q-θ response	-Linear actuators -Noisy sensors	q filter = $\frac{25}{S+25}$	5.0 rad/sec	Linear system performance
Pitch	δ_B	q, θ	2nd-order q-θ response	-Linear actuators -Clean sensors	No filtering	8.0 rad/sec	Linear system performance
Pitch	δ_B	q, θ β_{OF}, β_{OR}	2nd-order q-θ response	-Linear actuators -Clean sensors -Rotor position states available	No filtering	11.0 rad/sec	Linear system performance
Roll & Yaw	δ_S, δ_R	p, r, ϕ	-2nd-order p-ϕ response -1st-order r Response	-Nonlinear actuators -Noisy sensors	p filter = $\frac{S+24^2}{S^2+4.8S+24} \frac{S+72^2}{S^2+14.4S+72^2} \times \frac{60}{S+60}$ r filter = $\frac{20}{S+20}$	5.0* rad/sec	Sensor noise
Roll & Yaw	δ_S, δ_R	p, r, ϕ	-2nd-order p-ϕ response -1st-order r Response	-Nonlinear actuators -Clean sensors	No filtering	7.0* rad/sec	Linear system performance
Roll & Yaw	δ_S, δ_R	p, r, ϕ β_{SF}, β_{SR}	-2nd-order p-ϕ response -1st-order r Response	-Linear actuators -Clean sensors	No filtering	10.0* rad/sec	Linear system performance

*Limit based upon roll performance. Yaw bandwidths for each design was a first order root at the indicated location

**Proportional plus integral control was used on all designs

APPENDIX A

ROTOR DYNAMICS

Introduction

A significant portion of the study effort involved modeling, that is, vehicle rigid body, actuator dynamics and nonlinearities, sensor noise, and rotor dynamics. Rotor flapping dynamics were modeled over one period of revolution, as outlined by Hohenemser.[3] Equations were patterned after a development by Hall.[4] Significant impact from the tandem rotor arrangement (in particular, the front/rear rotor interaction) required special treatment as discussed in reference model parameters provided by Ostroff, et al.[2]

The final model derivations are part analytical (kinematics and coordinate rotations) and part numerical (external forces, rotor interaction, and rigid body/rotor coupling). The rotor models are mated to linearized rigid body dynamics with a reverse residualization technique to make full use of previously derived rigid body data.[2]

Blade Equations of Motion

A three degree of freedom (flap/lag/pitch) dynamic model of a helicopter blade is developed in this section.

Coordinates and Rotations

The coordinate systems used in the derivation are pictured in Figures A-1 and A-2 and defined in Table A-1. The fuselage coordinate system (F) is fixed in the helicopter, centered at the vehicle center of gravity. The hub system (H) for each rotor is fixed in the vehicle, but centered at the respective rotor hub and aligned with the rotor shaft which is tilted about the Y_F axis through an angle -i as shown in Figure A-1. The shaft coordinate system (S) is a fixed rotation (+180° about y_H) to aid in completing the rotations necessary to derive equations in the blade system (B). The other axes sets all rotate with the blades. All orientations with respect to each other are shown in Figure A-2 and defined in Table A-1.

Force and Moment Equations

The equations of motion for the blades are derived from the following momentum relation

$$\Sigma \vec{M} = \vec{H} + \vec{\Omega}^{B-I} \times H + m\vec{R}_{cm} \times \vec{a}^{o-I} \qquad \text{(A-1)}$$

where, $\vec{\Sigma} M$ is the vector of external moments acting at the blade hinge point

$\vec{H}$ is the angular momentum of the blade

$\vec{\Omega}^{B-I}$ is the angular momentum of the blade

m is the mass of the blade

$\vec{R}_{cm}$ is a vector pointing from the hinge point to the blade center of mass

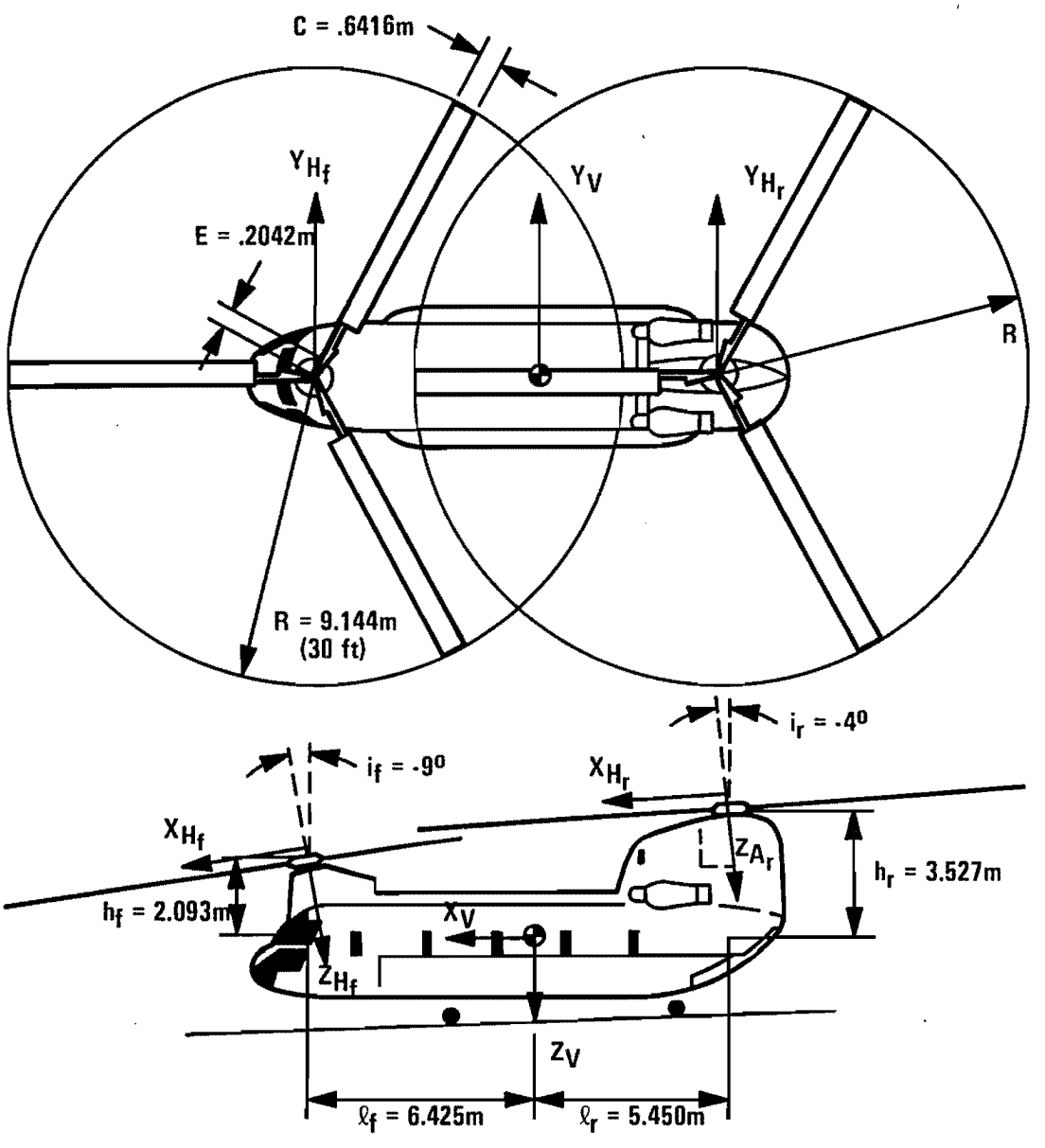

Figure A-1. Fuselage and Hub Coordinate Systems

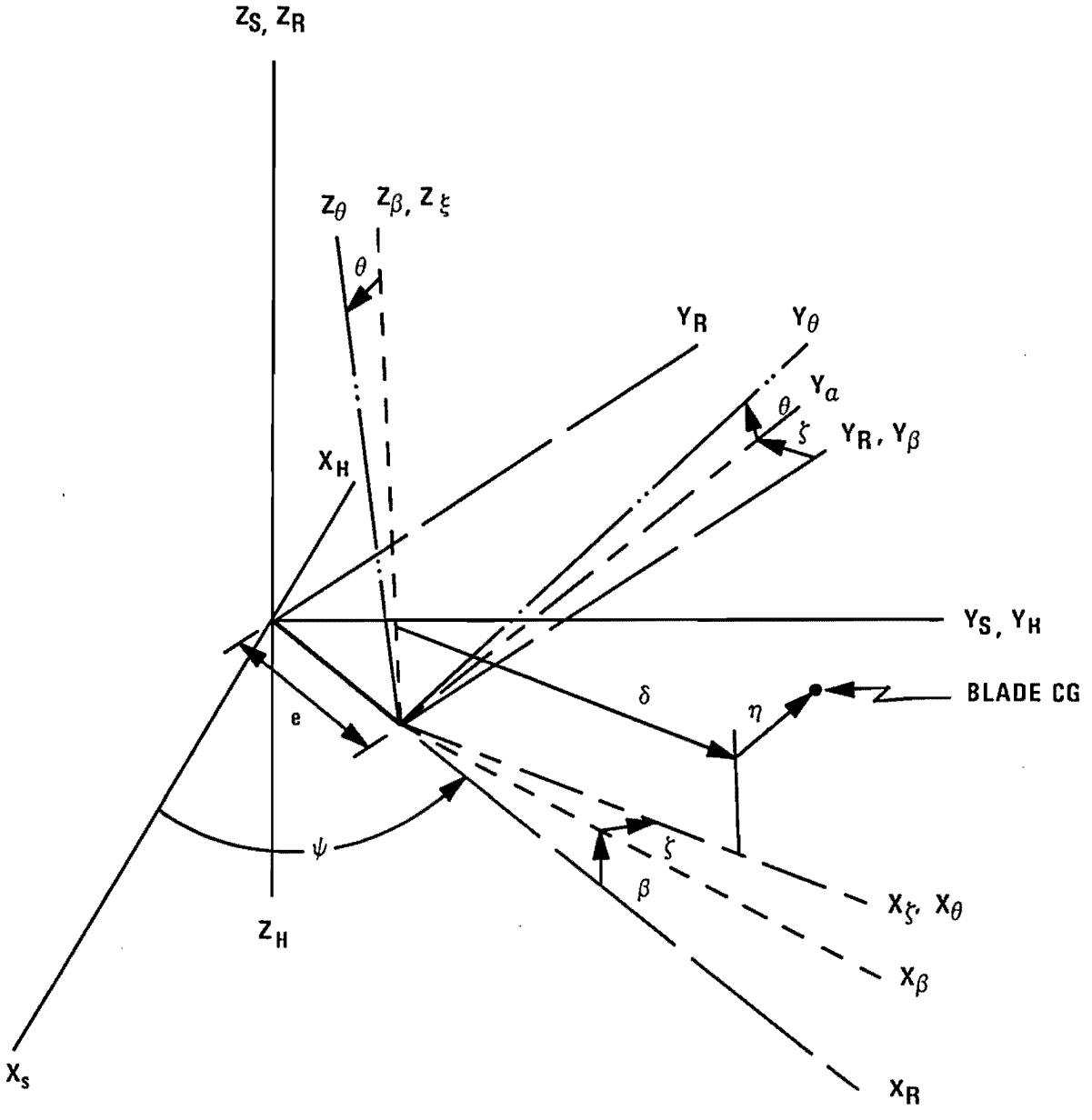

Figure A-2. Rotor Coordinate Systems

TABLE A-1. ROTATION SEQUENCE
(Fuselage to Blade)

Rotation	Axis of Rotation	Angle	Axis System	Frame Symbol
			X_F, Y_F, Z_F	F (Fuselage)
Tilt	Y_F	i		
			X_H, Y_H, Z_H	H (Hub)
Rotor Align	Y_H	+180°		
			(X_S, Y_S, Z_S)	S (Shaft)
Azimuth	Z_S	ψ		
			(X_R, Y_R, Z_R)	R (Rotor)
Flapping	Y_R	$-\beta$		
			$(X_\beta, Y_\beta, Z_\beta)$	
Inplane Lag	Z_β	ζ		
			$(X_\zeta, Y_\zeta, Z_\zeta)$	ζ (Inplane lag)
Pitch	X	θ		
			$(X_\theta, Y_\theta, Z_\theta)$	B (Blade)

$\vec{a}^{o-I}$ is the acceleration of the hinge point with respect to the inertial coordinate system

The angular momentum of the blade is the product of the inertia matrix and the angular velocity vector,

$$\vec{H} = I\,\vec{\Omega}^{B-I} \tag{A-2}$$

where

$$I \triangleq \begin{bmatrix} I_{xx} & I_{xy} & 0 \\ I_{xy} & I_{yy} & 0 \\ 0 & 0 & I_{zz} \end{bmatrix}$$

I_{xz} and I_{yz} inertia products in this matrix are assumed zero due to the smallness of the blade thickness relative to the chord and span.

The angular velocity vector $\vec{\Omega}^{B-I}$ is given by

$$\vec{\Omega}^{B-I} = \vec{\Omega}^{H-I} + \vec{\Omega}^{R-H} + \vec{\Omega}^{B-R} \tag{A-3}$$

where, $\vec{\Omega}^{H-I}$ is the angular velocity of the hub with respect to the inertial axes. Written in hub coordinates it is

$$\vec{\Omega}^{H-I}_{H} = [p_H, q_H, r_H]^T$$

$\vec{\Omega}^{R-H}$ is the angular velocity of the rotor with respect to the hub. Expressed in rotor coordinates it is

$$\vec{\Omega}^{R-H}_{R} = [0, 0, \Omega]^T$$

Ω^{B-R} is the angular velocity of the blade with respect to the rotor coordinate system. It is a combination of blade flapping, lagging, and pitching motion. In blade coordinates it is

$$\vec{\Omega}^{B-R}_{B} = T_{\theta/\zeta}\ [\dot{\theta}, 0, 0]^T + T_{\theta/\zeta} \cdot T_{\zeta/\beta}\ [0, 0, \dot{\zeta}]^T$$

$$+ T_{\theta/\zeta} \cdot T_{\zeta/\beta} \cdot T_{\beta/R}\ [0, -\dot{\beta}, 0]^T$$

The $T_{i/j}$ matrices in this expression are transformation matrices from the j coordinate system to the ith coordinate system.

If all the terms in Equation A-3 are expressed in the blade coordinate system and assuming the flap, lag, and pitch rotation angles (β, ζ, θ) are all small, the result is

$$\vec{\Omega}^{B-I}_{B} = \begin{bmatrix} -p_H\cos\psi + q_H\sin\psi + \beta\Omega + \dot{\theta} - \zeta\dot{\beta} \\ p_H\sin\psi + q_H\cos\psi + \theta\Omega + \theta\dot{\zeta} - \dot{\beta} - \beta\Omega \\ -r_H + \Omega + \dot{\zeta} + \theta\dot{\beta} \end{bmatrix} \tag{A-4}$$

Thus the angular momentum of the blade expressed in blade coordinates is

$$\vec{H}_B = I_B\,\vec{\Omega}^{B-I}_{B} = \begin{bmatrix} I_{xx}(-p_H\cos\psi + q_H\sin\psi + \beta\Omega + \dot{\theta} - \zeta\dot{\beta}) \\ \quad + I_{xy}(p_H\sin\psi + q_H\cos\psi + \theta\Omega + \theta\dot{\zeta} - \dot{\beta} - \zeta\beta\Omega) \\ I_{xy}(-p_H\cos\psi + q_H\sin\psi + \beta\Omega + \dot{\theta} - \zeta\dot{\beta}) \\ \quad + I_{yy}(p_H\sin\psi + q_H\cos\psi + \theta\Omega + \theta\dot{\zeta} - \dot{\beta} - \zeta\beta\Omega) \\ I_{zz}(-r_H + \Omega + \dot{\zeta} + \theta\dot{\beta}) \end{bmatrix} \tag{A-5}$$

The acceleration of the hinge point $\vec{a}^{o-I}$ in Equation A-1 is given by the equation

$$\vec{a}^{o-I} = \vec{a}^{h-I} + \dot{\vec{\Omega}}^{R-I} \times \vec{\rho}^{o-h} + \vec{\Omega}^{R-I} \times (\vec{\Omega}^{R-I} \times \vec{\rho}^{o-h}) \tag{A-6}$$

where $\vec{a}^{h-I}$ is the acceleration of the rotor hub

$\vec{\Omega}^{R-I}$ is the angular velocity of the hinge with respect to the inertial axes. In rotor coordinates,

$$\vec{\Omega}^{R-I}_{R} = \begin{bmatrix} -p_H \cos\psi + q_H \sin\psi \\ p_H \sin\psi + q_H \cos\psi \\ -r_H + \Omega \end{bmatrix}$$

$\vec{\rho}^{o-H}$ is a vector pointing from the rotor hub to the blade hinge point. Expressed in rotor coordinates it is

$$\vec{\rho}^{o-H}_{R} = [e,\ 0,\ 0]^T \qquad \text{(See Figure A-2)}$$

Similarly $\vec{a}^{H-I}$, the acceleration of the hub, is given by

$$\vec{a}^{H-I}_{H} = \begin{bmatrix} \dot{u}_H + q_H w_H - r_H v_H \\ \dot{v}_H + r_H u_H - p_H w_H \\ \dot{w}_H + p_H v_H - q_H u_H \end{bmatrix}$$

The acceleration of the hinge point $\vec{a}^{o-I}$ is found by solving Equation A-6, taking care to transform all terms into the same coordinate system. If all the small terms are dropped, the resulting expression for $\vec{a}^{o-I}$ is

$$\vec{a}_B^{o-I} = \begin{bmatrix} -(\dot{u}_H + q_H w_H - r_H v_H)\cos\psi \\ \quad + (v_H + r_H u_H - p_H w_H)\sin\psi \\ \quad - e(\Omega^2 + 2\Omega r_H) \\ \\ (\dot{u}_H + q_H w_H - r_H v_H)\sin\psi \\ \quad + (\dot{v}_H + r_H u_H - p_H w_H)\cos\psi \\ \quad - e r_H + e\zeta\Omega^2 + e\beta 2\Omega^2 \\ \\ -(\dot{w}_H + p_H v_H - q_H u_H) \\ \quad - e(p_H - 2q_H\Omega)\sin\psi - e\,(q_H + 2p_H\Omega)\cos\psi \\ \quad + \beta e\Omega^2 - \zeta\theta e\Omega^2 \end{bmatrix} \qquad \text{(A-8)}$$

The vector R_{cm} is Equation A-1. Written in blade coordinates, this is

$$\vec{R}_{B_{cm}} = [\delta,\ \eta,\ 0]^T \qquad \text{(See Figure A-2)} \qquad \text{(A-9)}$$

Substituting Equations A-4, A-5, A-8, and A-9 into Equation A-1 and performing the indicated operation results in the general flap-lag-pitch equations of motion.

Pitch:

$$
\begin{aligned}
M_x = {} & I_{xx}[(-\dot{p}_H - q_H\Omega)\cos\psi + (\dot{q}_H + p_H\Omega)\sin\psi + \dot{\beta}\Omega + \ddot{\theta} - \zeta\ddot{\beta}] \\
& + (I_{zz} - I_{yy})\,[p_H\Omega\sin\psi + q_H\Omega\cos\psi + \theta\Omega^2 + 2\theta\dot{\zeta}\Omega - \dot{\beta}\Omega - \zeta\beta\Omega^2] \\
& + I_{xy}\,[(\dot{p}_H - 2q_H\Omega)\sin\psi + (\dot{q}_H + 2p_H\Omega)\cos\psi + \theta\ddot{\zeta} - \ddot{\beta} - \beta\Omega^2 - 2\beta\dot{\zeta}\Omega] \\
& + m_\eta[-(\dot{w}_H + p_H v_H - q_H u_H) - e(\dot{p}_H - 2q_H\Omega)\sin\psi \\
& \quad - e(q_H + 2p_H\Omega)\cos\psi + \beta e\Omega^2 - \zeta\theta e\Omega^2]
\end{aligned}
\tag{A-10a}
$$

Flap:

$$
\begin{aligned}
M_y = {} & I_{yy}[(\dot{p}_H - q_H\Omega)\sin\psi + (\dot{q}_H + p_H\Omega)\cos\psi + \dot{\theta}\Omega + \theta\ddot{\zeta} - \ddot{\beta} - \dot{\zeta}\beta\Omega - \dot{\beta}\zeta\Omega] \\
& + (I_{xx} - I_{zz})\,[-p_H\Omega\cos\psi + q_H\Omega\sin\psi + \beta\Omega^2 + \beta\dot{\zeta}\Omega + \dot{\theta}\Omega - \zeta\dot{\beta}\Omega] \\
& + I_{xy}[(-\dot{p}_H + 2q_H\Omega)\cos\psi + (\dot{q}_H + 2p_H\Omega)\sin\psi + \ddot{\theta} - \zeta\ddot{\beta} + \theta\Omega^2 + 2\theta\dot{\zeta}\Omega - \zeta\beta\Omega^2] \\
& - m_\delta[-(\dot{w}_H + p_H v_H - q_H u_H) - e(\dot{p}_H - 2q_H\Omega)\sin\psi - e(\dot{q}_H + 2p_H\Omega)\cos\psi \\
& \quad + \beta e\Omega^2 - \zeta\theta e\Omega^2]
\end{aligned}
\tag{A-10b}
$$

Lag:

$$
\begin{aligned}
M_z = {} & I_{zz}[-r_H + \ddot{\zeta} + \theta\ddot{\beta}] \\
& + (I_{yy} - I_{xx})\,[-\beta\dot{\beta} + \theta\dot{\theta}\Omega] \\
& + I_{xy}\,[2\beta\dot{\theta}\Omega + 2\theta\dot{\beta}\Omega] \qquad \text{(A-10c)} \\
& + m\delta[(\dot{u}_H + q_H w_H - r_H v_H)\cos\psi + (\dot{v}_H + r_H U_H - p_H \omega_H)\cos\psi \\
& \qquad - e\dot{r}_H + e\zeta\Omega^2 + e\beta\,\theta\Omega^2] \\
& - m_\eta[-(\dot{u}_H + q_H w_H - r_H v_H)\cos\psi + (\dot{v}_H + r_H u_H - p_H w_H)\sin\psi \\
& \qquad - e\Omega^2 + 2e\Omega r_H]
\end{aligned}
$$

Some simplification in these equations is possible with the assumptions that

$$I_{xx} << I_{yy} \simeq I_{zz}$$

$$I_{zz} - I_{yy} \simeq I_{xx}$$

The first of these assumptions implies that the moment of inertia about the flap hinge is approximately equal to the moment of inertia about the lag hinge and much larger than the moment of inertia about the blade pitch axis. The second approximation comes from assuming that the blade thickness and chord length are small in comparison with the span.

Furthermore, if it is assumed that the blade is a homogeneous rectangular prism, its inertia properties can be approximated as

$$I_{zz} \simeq I_{yy} = \frac{m(R-e)^2}{3}$$

$$I_{xy} = \frac{m(R-e)\eta}{2}$$

where m is the mass of the blade

R is the blade radius

e is the hinge offset distance

η is the distance from the pitch axis to the blade center of gravity (see Figure A-2).

Substituting these relations into Equations A-10 and introducing the notation

$$\bar{\eta} = \eta/R$$

$$\bar{e} = e/R$$

gives the simplified flap-lag-pitch equations of motion.

Pitch:

$$\begin{aligned}\frac{M_x}{I_{xx}} &= (-\dot{p}_H + 2q_H\Omega)\cos\psi + (\dot{q}_H + 2p_H\Omega)\sin\psi + \ddot{\theta} + (\Omega^2 + 2\Omega\dot{\zeta}) - \zeta(\ddot{\beta} + \Omega^2\beta) \\ &+ \frac{I_{xy}}{I_{xx}}\left[(\dot{p}_H - 2q_H\Omega)\sin\psi + (\dot{q}_H + 2p_H\Omega)\cos\psi + \ddot{\zeta}\theta - \ddot{\beta} - (\Omega^2 + 2\Omega\dot{\zeta})\beta\right] \\ &+ \frac{m_\eta}{I_{xx}}\left[-(\dot{w}_H + p_H v_H - q_H u_H) - e(\dot{p}_H - 2q_H\Omega)\sin\psi - e(\dot{q}_H + 2p_H\Omega)\cos\psi\right. \\ &\left. + e\Omega^2\beta - e\Omega^2\zeta\theta\right]\end{aligned} \tag{A-11a}$$

Flap:

$$\frac{M_y}{I_{yy}} = (\dot{p}_H - 2q_H\Omega)\sin\psi + (\dot{q}_H + 2p_H\Omega)\cos\psi - \ddot{\beta} - (\Omega^2 + 2\Omega\dot{\zeta})\beta + \theta\ddot{\zeta}$$

$$+\frac{e}{2}\frac{\overline{\eta}}{(1-\overline{e})}[(-p_H + 2q_H\Omega)\cos\psi + (q_H + 2p_H\Omega)\sin\psi + \ddot{\theta} \qquad \text{(A-11b)}$$

$$+ (\Omega^2\ 2\Omega\dot{\zeta})\theta - (\ddot{\beta} + \Omega^2\beta)\zeta]$$

$$+\frac{3/R}{2(1-\overline{e})}[\dot{w}_H + p_H v_H - q_H u_H]$$

$$+\frac{3\overline{e}}{2(1-\overline{e})}[(p_H - 2q_H\Omega)\sin\psi + (\dot{q}_H + 2p_H\Omega)\cos\psi - \Omega^2\beta + \Omega^2\zeta\,\theta]$$

Lag:

$$\frac{M_z}{I_{zz}} = -\dot{r}_H + \ddot{\zeta} + \theta\ddot{\beta} - \beta\dot{\beta}\Omega + \theta\dot{\theta}\Omega + \Omega^2\beta\,\theta + \dot{\theta}\dot{\beta}$$

$$+\frac{3\overline{\eta}}{2(1-\overline{e})}[2\Omega\beta\dot{\theta} + 2\Omega\,\theta\dot{\beta}]$$

$$+\frac{3/R}{2(1-\overline{e})}[(\dot{u}_H + q_H\,\omega_H - r_H v_H)\sin\psi + (\dot{v}_H + r_H u_H - p_H w_H)\cos\psi]$$

$$+\frac{3\overline{\eta}/R}{(1-\overline{e})^2}[(\dot{u}_H + q_H\,\omega_H - r_H v_H)\cos\psi - (\dot{v}_H + r_H u_H - p_H w_H)\sin\psi]$$

$$+\frac{3\overline{e}}{2(1-\overline{e})}[-\dot{r}_H + \xi\Omega^2 + \beta\theta\Omega^2] + \frac{3\overline{\eta}\,\overline{e}}{(1-\overline{e})^2}[\Omega^2 - 2\Omega r_H] \qquad \text{(A-11c)}$$

External Moments

The external moments acting on the rotor blades come from two sources, (a) aerodynamic forces and (b) spring forces in the hinges. The moment due to aerodynamic forces is found by integrating the lift force acting on the blade. Lift per unit span is given by the equation

$$L = \frac{1}{2} \rho a c U^2 \alpha$$

where L is the lift force per unit span

ρ is air density

a is the slope of the sectional lift curve

c is chord length

U is the velocity of air passing over the blade

α is the angle of attack of the blade

If the radial component is ignored, the velocity of the airflow at the blade elements can be resolved into a component in the plane of rotation, U_T, and a component perpendicular to the plane of rotation, U_P, as shown in Figure A-3. Since $U_p/V_T << 1$, the total lift acting in the vertical direction is

$$L_\beta = \frac{1}{2} \rho a c \int_0^R (U_T^2 + U_p^2)(\theta - U_P/U_T)\, dr$$

$$= \frac{1}{2} \rho a c \int_0^R U_T^2 (1 + U_P^2/U_T^2)(\theta - U_P/U_T)\, dr$$

$$\cong \frac{1}{2} \rho a c \int_0^R (U_T^2 \theta - U_T U_P)\, dr.$$

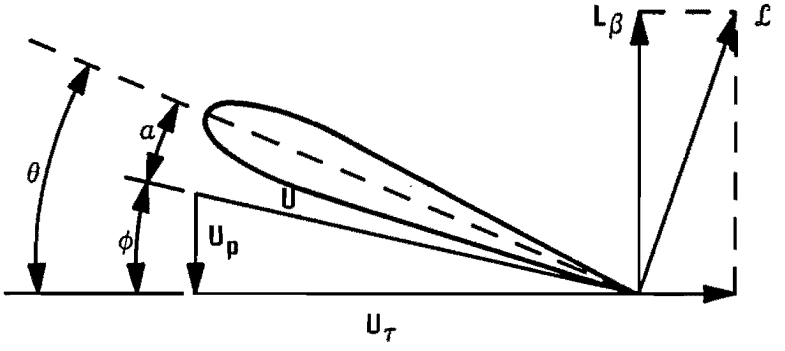

Figure A-3. Resolution of Blade Element Velocity Components[4]

The moment acting about the flap hinge line ($-Y_s$ direction) is

$$M_\beta \cong \frac{1}{2} \rho a c \int_0^R (U_T^2 \theta - U_T U_P) \, r \, dr \qquad \text{(A-12a)}$$

and the moment about the lag hinge line (Z_ζ direction) is

$$M_\zeta \cong \frac{1}{2} \rho a c \int_0^R (U_P^2 - U_T U_P \theta) \, r dr \qquad \text{(A-12b)}$$

where θ is the pitch angle of the blade.

With the introduction of the rotor lock number

$$\gamma = \frac{\rho a c R^4}{I_\beta}$$

where I_β is the moment of inertia about the flap hinge ($I_\beta = I_{yy} = I_{zz}$) becomes

$$\frac{M_y}{I_{yy}} \cong \frac{M_\beta}{I_\beta} = \frac{\gamma}{8} \int_0^1 4(\tilde{U}_T^{\,2}\,\theta - \tilde{U}_P\tilde{U}_T)\,x dx \tag{A-13a}$$

$$\frac{M_z}{I_{zz}} = \frac{M_\zeta}{I_\beta} = \frac{\gamma}{8} \int_0^1 4(\tilde{U}_P^{\,2} - \tilde{U}_T\tilde{U}_P\,\theta)\,x dx \tag{A-13b}$$

where

$$\tilde{U}_T = U_T/R$$

$$\tilde{U}_P = U_P/R$$

$$x = r/R$$

Expressions for U_T and U_P are obtained from the equation

$$\vec{v}^{\,B-I} = \vec{v}^{\,S-I} + \vec{\Omega}^{R-I} \times \vec{e} + \vec{\Omega}^{B-I} \times \vec{\delta}^{\,b-0}$$

where $\vec{v}^{\,B-I}$ is the velocity of the blade. In the blade coordinate system it is

$$\vec{v}^{\,B-I}_B = [U_R,\ U_T,\ U_P]^T.$$

$\vec{v}^{\,S-I}$ is the velocity of the shaft. Expressed in hub coordinates it is

$$\vec{v}^{\,S-I}_H = [u_H,\ v_H\ w_H]^T.$$

$\vec{\Omega}^{R-I}$ is the angular velocity of the rotor with respect to the inertial coordinate system

$$\vec{\Omega}_R^{R-I} = \begin{bmatrix} -p_H \cos\psi + q_H \sin\psi \\ p_H \sin\psi + q_H \cos\psi \\ -r_H + \Omega \end{bmatrix}$$

$\vec{e}$ is the vector from the rotor hub to the hinge line

$$\vec{e}_R = [e,\ 0,\ 0]^T.$$

$\vec{\Omega}^{B-I}$ is the angular velocity of the blade (see Equation A-4).

$\vec{\delta}^{b-0}$ is the vector pointing from the hinge point to a point located a distance r down the blade

$$\vec{\delta}_B^{b-0} = [r,\ 0,\ 0]^T.$$

Performing the algebraic manipulations indicated in Equation A-14 results in the following expressions for U_T and U_P:

$$U_T = (r+e)\,(\Omega - r_H) + r\dot{\zeta} + (v_H + \zeta u_H)\cos\psi - (u_H + \zeta v_H)\sin\psi \qquad \text{(A-15)}$$

$$U_P = r\dot{\beta} + [-(r+e)\,q_H + \beta u_H]\cos\psi + [-(r+e)\,p_H - \beta v_H]\sin\psi - w_H$$

The total velocity at the blade is obtained by adding a downwash term to Equation A-15. Analytical and empirical formulae exist for downwash and these may be sufficient for single main rotor vehicles. However, for a

tandem rotor helicopter with overlapping horizontal rotor planes the downwash velocity is the source of key cross rotor interaction terms. Rotor interaction will be discussed in a later section and its inclusion here is limited to the following definition

ν is the blade downwash (or induced) velocity generated by the increased air passing through the rotor producing thrust

ν is therefore added to the U_P equation in A-15.

$$U_T = (r+e)(\Omega - r_H) + r\dot{\zeta} + (v_H + \zeta u_H)\cos\psi - (u_H + \zeta v_H)\sin\psi \tag{A-16}$$

$$U_P = r\dot{\beta} + [-(r+e)\, q_H + \beta u_H]\cos\psi + [-(r+e)\, p_H - \beta v_H]\sin\psi - w_H + \nu$$

It is further assumed that the pitching motions of the blade are small, so that for a given blade element, the pitch angle of the blade, θ, can be approximated as

$$\theta = \theta_0 - \theta_s \sin\psi - \theta_c \cos\psi + \theta_T r + \text{h.o. } (n\psi)^* \tag{A-17}$$

where θ_0 is the collective input

---

*Higher order harmonics of ψ can be used if appropriate. Hohenemser has expanded these terms in Ref. 3.

θ_s is the longitudinal cyclic* input

θ_c is the lateral cyclic* input

θ_T is the blade twist per radial element (assumed constant)

This approximation also implies that the actual pitch angle dynamics (Equation 11a) are fast and therefore will be ignored.

Spring Moments

Spring restraints on the rotor flapping and lagging can be expressed as

$$M_\beta \text{ spring} = K_\beta \beta$$
$$M_\zeta \text{ spring} = K_\zeta \delta \qquad \text{(A-18)}$$

Linear Solution to Tip Path Plane Equations

As with the pitch angle, the use of the first harmonic approximation is applied to the flap equation A-11b. From this point on, pitching, θ, will be assumed to be an input (Equation A-17) and lag, δ, will be assumed negligible, that is, $\delta = \dot{\delta} = \ddot{\delta} = 0$.

Letting

$$\beta(t) = \beta_o(t) - \beta_c(t) \cos\psi - \beta_s \sin\psi \qquad \text{(A-19)}$$

---

*Special note should be taken of the terminology of longitudinal cyclic reference to the $\sin\psi$ coefficient, θ_c. Control inputs effect blade flapping gyroscopically; that is, a $\sin\psi$ direction input produces a $\cos\psi$ output in β; likewise, a $\cos\psi$ input θ produces a $\sin\psi$ output in β.

where

$\beta_o(t)$ is the coning angle

$\beta_c(t)$ is the longitudinal flap angle

$\beta_s(t)$ is the lateral flap angle

and taking derivatives of A-19 yields

$$\dot{\beta}(t) = \dot{\beta}_o - (\dot{\beta}_c + \Omega\beta_s)\cos\psi - (\dot{\beta}_s - \Omega\beta_c)\sin\psi \tag{A-20}$$

$$\ddot{\beta}(t) = \ddot{\beta}_o - (\ddot{\beta}_c + 2\,\Omega\dot{\beta}_s - \Omega^2\,\beta_c)\cos\psi - (\ddot{\beta}_s - 2\,\Omega\dot{\beta}_c - \Omega^2\beta_s)\sin\psi. \tag{A-21}$$

Substituting A-19, A-20, and A-21 into the flapping Equations A-11b, we get grouped terms of rotor harmonic coefficients as follows:

Coning:

$$\ddot{\beta}_o + \left\{ [1 + \frac{3\bar{e}}{2(1-\bar{e})}]\,\Omega^2 + \frac{K_\beta}{I_{yy}} \right\} \beta_o - \frac{3/R_T}{2(1-\bar{e})}\,(\dot{w}_H + v_{Ho}p_H + u_{Ho}) = \sum_{i=1}^{n} M_{oi}\delta x_i + M_{oo}(\bar{x}_o) \tag{A-22}$$

Longitudinal flapping, that is, $\sin(\psi)$ terms:

$$\ddot{\beta}_c + 2\Omega\beta_s - \Omega^2\beta_c + \left\{ [1 + \frac{3\bar{e}}{2(1-\bar{e})}]\,\Omega^2 + \frac{K_\beta}{I_{yy}} \right\}\beta_c + 2\Omega\,[1 + \frac{3\bar{e}}{2(1-\bar{e})}]\,p_H + [1 + \frac{3\bar{e}}{2(1-\bar{e})}]\,\dot{q}_H = \sum_{i=1}^{n} M_{ci}\delta x_i + M_{co}(\bar{x}_o) \tag{A-23}$$

Lateral flapping, that is, $\sin(\psi)$ terms:

$$\ddot{\beta}_s - 2\Omega\dot{\beta}_c - \Omega^2\beta_s + \left\{ [1 + \frac{3\bar{e}}{2(1-\bar{e})}]\,\Omega^2 + \frac{K_\beta}{I_{yy}} \right\} \beta_s$$
$$- 2\Omega\,[1 + \frac{3\bar{e}}{2(C1-\bar{e})}]\,q_H + [1 + \frac{3\bar{e}}{2(1-\bar{e})}]\,\dot{p}_H \qquad \text{(A-24)}$$
$$= \sum_{i=1}^{n} M_{si}\delta x_i + M_{so}(\bar{x}_o)$$

where

- $M_{oo}(\bar{x}_i)$, $M_{co}(\bar{x}_i)$, and $M_{so}(\bar{x}_i)$ are trim moments for flap dynamic coning, pitching, and rolling, respectively.
- $\bar{x}_o$ is the trim state vector containing trim values for all rigid body and rotor states and controls. These values are derived later.
- M_{oi}, M_{ci}, and M_{si} are aerodynamic moment perturbations for state x_i for flap coning, pitching, and rolling, respectively. They are derived below.
- δx_i is the perturbation of state X_i when $\bar{X}^T = (u_H, v_H, w_H, p_H, q_H, r_H, \beta_o, \dot{\beta}_o, \beta_c, \dot{\beta}_c, \beta_s, \dot{\beta}_s, \theta_o, \theta_c, \theta_s)$

Aerodynamic Moment Perturbations

Analytical expressions for the individual coefficients for the M_{oi}'s, M_{ci}'s, and M_{si} have been derived by Hohenemser[3] and Hall.[4] For this study, however, these parameters were derived numerically because of numerous trim values. This created a massive set of perturbed combinations and a complicated, yet important interaction between the front and rear rotors (detailed later).

Using Equation A-13a,

$$\frac{M_y}{I_{yy}} \cong \frac{\gamma}{8} \int_0^1 4(\tilde{U}_T{}^2\theta - \tilde{U}_P\tilde{U}_T)\, x dx$$

and neglecting the offset distance, e,

$$\tilde{U}_T = (\Omega - r_H) + (v_H \cos\psi + u_H \sin\psi)/R$$

$$\tilde{U}_P = x\dot{\beta} - (xq_H - \frac{u_H}{R}) \cos\psi - (xp_H + \frac{\beta V_H}{R}) \sin\psi \qquad \text{(A-25)}$$

$$- (w_H + \nu/R)$$

A-13a can be expanded analytically, and certain major portions of the integral have been derived through first and higher harmonics in ψ. For the current application, however, the integration with respect to x is carried out by grouping terms in powers of x and performing the integration analytically. This leaves numerous harmonic terms associated with θ (Equation A-17), β (Equation A-19), and $\dot{\beta}$ (Equation A-20), plus the harmonic terms contained in the definition of $\tilde{U}_T$ and $\tilde{U}_P$ (Equation A-25). The coefficient grouping is performed by numerical harmonic matching; in other words,

$$M_o = \frac{1}{2\pi} \int_0^{2\pi} \frac{M_y}{I_{yy}}\, d\psi \qquad \text{(A-26a)}$$

$$M_c = \frac{1}{2\pi} \int_0^{2\pi} \frac{M_y}{I_{yy}} \cos\psi d\psi \qquad \text{(A-26b)}$$

$$M_s = \frac{1}{2\pi} \int_0^{2\pi} \frac{M_y}{I_{yy}} \sin\psi d\psi \qquad \text{(A-26c)}$$

Trim values M_{oo}, M_{co}, and M_{so} are calculated by fixing the input state $\bar{x}$ at trim ($\bar{x}_o$). Perturbation quantities, M_{oi}'s, M_{ci}'s, and M_{si}'s, are calculated by forward and backward perturbing of the input state. For example

$$M_{ci} = \frac{\frac{1}{2\pi} \int_0^{2\pi} \frac{M_y}{I_{yy}} (x_i + \Delta x_i) \cos\psi d\psi - \frac{1}{2\pi} \int_0^{2\pi} \frac{M_y}{I_{yy}} (x_i - \Delta x_i) \cos\psi d\psi}{2\Delta x_i}$$

These results are coupled with the analytical relationships of Equations A-22 through A-24 to form the flapping equations of motion.

Rotor Forces and Moments on the Vehicle

The rotor impact on the vehicle comes from three sources:

- Spring forces
- Inertia forces
- Aerodynamic forces

Spring Forces

Equation A-18 shows the spring moment equations. Using only A-18a, since we have dropped the rotor lagging dynamics, we can expand the flapping moment using Equation A-19 for β:

$$M\beta spring = K_\beta(\beta_o - \beta_c \cos\psi - \beta_s \sin\psi)$$

In hub coordinates this moment becomes

$$M_{XSH} = -M\beta spring \sin\psi$$

$$M_{YSH} = -M\beta spring \cos\psi$$

Averaging over one revolution and including all blades (N_B),

$$\overline{M}_{XSH} = \frac{N_B}{2\pi} \int_0^{2\pi} M_{SXH}\, d\psi = \frac{N_\beta}{2} K_\beta \beta_s \tag{A-27a}$$

$$\overline{M}_{YSH} = \frac{N_B}{2\pi} \int_0^{2\pi} M_{SYH}\, d\psi = \frac{N_\beta}{2} K_\beta \beta_c \tag{A-27b}$$

Inertia Forces

Using techniques documented earlier, the one-revolution average forces produced by inertia at the hub can be written in hub coordinates

$$\overline{F}_{XIH} = -N_B \rho_B R [\dot{u}_H + q_H \omega_H - r_H U_H] \tag{A-28a}$$

$$\overline{F}_{YIH} = -N_B \rho_B R [\dot{v}_H + v_H u_H - p_H w_H] \tag{A-28b}$$

$$\overline{F}_{ZIH} = -N_B \rho_B R [\dot{w}_H + p_H v_H - q_H u_H - \frac{1}{2} \dot{\beta}_o R] \tag{A-28c}$$

Moments acting on the fuselage at the hub result in the above forces being applied through the rotor offset e. These are derived in rotor coordinates, converted to the hub system, and averaged over one revolution to become

$$M_{XIH} = -\frac{1}{4} e N_B \rho_B R [(\ddot{\beta}_s + \dot{p}_H) - 2\Omega(\dot{\beta}_c + q_H) \Omega^2 \beta_s] \tag{A-29a}$$

$$M_{YIH} = -\frac{1}{4}\, e\, N_B\, \rho_B R\, [(\ddot{\beta}_c + \dot{q}_H) + 2\Omega(\dot{\beta}_s + p_H) - \Omega^2 \beta_c] \tag{A-29b}$$

$$M_{ZIH} = -\frac{1}{2}\, e\, N_B\, \rho_B R\, [\dot{r}_H] \tag{A-29c}$$

The above equations also include the assumptions that products of small perturbations can be eliminated and $e \ll R/2$.

Aerodynamic Lift Forces

Equation A-12 shows the lift characteristics for a given rotor blade. This can be translated to hub coordinate forces and moments as follows:

$$F_{ZLH} = -L \tag{A-30a}$$

$$M_{XLH} = e\, L \sin\psi \tag{A-30b}$$

$$M_{YLH} = -e\, L \cos\psi \tag{A-30c}$$

where Equation A-12 is modified to be:

$$L = \frac{1}{2}\, \rho a c\, R^3 \int_0^1 (\tilde{U}_T^{\,2}\, \theta - \tilde{U}_P \tilde{U}_T)\, dx \tag{A-31}$$

The A-30 equations are averaged over one revolution for all blades of a rotor;

$$\overline{F}_{ZLH} = -\frac{N_\beta}{2\pi} \int_0^{2\pi} L\, d\psi \tag{A-32a}$$

$$\overline{M}_{XLH} = -\frac{N_\beta e}{2\pi} \int_0^{2\pi} L \sin\psi d\psi \tag{A-32b}$$

$$\overline{M}_{YLH} = -\frac{N_\beta e}{2\pi} \int_0^{2\pi} L \cos\psi d\psi \tag{A-32c}$$

Inplane Forces

Figure A-4 augments Figure A-3 by showing the inplane force relationships for a typical rotor. In hub coordinates these can be resolved to be

$$F_{XD} = -D \sin\psi + L(\beta \cos\psi - \tilde{U}_P/\tilde{U}_T \sin\psi) \tag{A-33a}$$

$$F_{YD} = -D \cos\psi - L\,(\tilde{U}_P/\tilde{U}_T \cos\psi + \sin\psi) \tag{A-33b}$$

where L is defined in Equation A-31 and

$$D = \frac{1}{2}\,\rho C\,R^3\,C_{do} \int_0^1 \tilde{U}_T^{\,2}\,dx. \tag{A-34}$$

These forces are integrated over one revolution to yield the average value for an N_β bladded rotor,

$$\overline{F}_{XDH} = \frac{N_\beta}{2\pi} \int_0^{2\pi} F_{XDH}\,d\psi \tag{A-35a}$$

$$\overline{F}_{YDH} = \frac{N_\beta}{2\pi} \int_0^{2\pi} F_{YDH}\,d\psi \tag{A-35b}$$

Total Forces and Moments

The forces and moments derived from spring, inertial, and aerodynamic sources are

$$\begin{aligned} \overline{F}_{XH} &= \overline{F}_{XIH} + \overline{F}_{XDH} \\ \overline{F}_{YH} &= \overline{F}_{YIH} + \overline{F}_{YDH} \\ \overline{F}_{ZH} &= \overline{F}_{ZIH} + \overline{F}_{ZLH} \end{aligned} \tag{A-36}$$

$$\overline{M}_{XH} = \overline{M}_{XSH} + \overline{M}_{XLH}$$

$$\overline{M}_{YH} = \overline{M}_{YSH} + \overline{M}_{YLH} \qquad \text{(A-37)}$$

$$\overline{M}_{ZH} = 0$$

Transfer from Hub to Fuselage Coordinates

In all previously defined equations the center of action was the rotor hub. All input dynamic states from the vehicle (vehicle translational and rotational velocities and accelerations) were input at the hub position. All output rotor forces and moments were also centered at the hub.

It is necessary to translate and rotate these quantities to the vehicle body axis located at the c.g. of the aircraft. Referring to Figure A-1 for a given rotor inclination, i, forward offset, ℓ, and vehicle offset, h, the following vehicle state transformations of velocities must be made:

$$\begin{pmatrix} u_H \\ v_H \\ w_H \end{pmatrix} = \begin{pmatrix} \cos i & 0 & -\sin i \\ 0 & 1 & 0 \\ \sin i & 0 & \cos i \end{pmatrix} \begin{pmatrix} u_V - hq_V \\ v_V + \ell r_V + hp_V \\ w_V - \ell q_V \end{pmatrix} \qquad \text{(A-38)}$$

$$\begin{pmatrix} p_H \\ q_H \\ r_H \end{pmatrix} \begin{pmatrix} \cos i & 0 & -\sin i \\ 0 & 1 & 0 \\ \sin i & 0 & \cos i \end{pmatrix} \begin{pmatrix} p_V \\ q_V \\ r_V \end{pmatrix} \qquad \text{(A-39)}$$

Since i, ℓ, and h are fixed in time acceleration states, u_H, v_H, w_H, p_H, q_H, and r_H would be transformed in the same manner. The output forces and moments are transformed back to the vertical body system at the c.g. as follows:

$$\begin{pmatrix} \overline{F}_{XV} \\ \overline{F}_{YV} \\ \overline{F}_{ZV} \end{pmatrix} = \begin{pmatrix} \cos i & 0 & \sin i \\ 0 & 1 & 0 \\ -\sin i & 0 & \cos i \end{pmatrix} \begin{pmatrix} \overline{F}_{XH} \\ \overline{F}_{YH} \\ \overline{F}_{ZH} \end{pmatrix} \tag{A-40}$$

$$\begin{pmatrix} \overline{M}_{XV} \\ \overline{M}_{YV} \\ \overline{M}_{ZV} \end{pmatrix} = \begin{pmatrix} \cos i & 0 & \sin i \\ 0 & 1 & 0 \\ -\sin i & 0 & \cos i \end{pmatrix} \begin{pmatrix} \overline{M}_{XH} + \ell F_{YV} \\ \overline{M}_{YH} - \ell \overline{F}_{ZV} - h\,\overline{F}_{XV} \\ \overline{M}_{ZH} \end{pmatrix}$$

Rotor Interference

The treatment of rotor dynamics, to this point, has proceeded nicely with individual rotors. The impact of rotor interference, however, is significant for this type of tandem arrangement. A good analytical study of this effect for the CH-46 helicopter is contained in Reference 5.

The parameter ν in Equation A-15 represents the appropriate location for analyzing this effect.

Let

$$\lambda_I \triangleq \frac{\nu}{|\Omega|\,R} \qquad \text{(interference in flow ratio)}$$

also

$$\lambda = \frac{w_H}{|\Omega| R} \qquad \text{(in flow ratio)}$$

$$\mu = \frac{u_H}{|\Omega| R} \qquad \text{(advance ratio)}$$

Reference 2 contains the following front (subscript F) and rear (subscript R) interaction relationships

$$\lambda_{IF} = \frac{C_{TF}}{2[(\lambda_F - \lambda_{IF})^2 (\mu_F)^2]^{1/2}} + dF_{RF} \frac{C_{TR}}{2[(\lambda_R - \lambda_{IR})^2 + (\mu_R)^2]^{1/2}} \tag{A-42}$$

$$\lambda_{IR} = \frac{C_{TR}}{2[(\lambda_R - \lambda_{IR})^2 (\mu_R)^2]^{1/2}} + dF_{FR} \frac{C_{TF}}{2[(\lambda_F - \lambda_{IF})^2 + (\mu_p)^2]^{1/2}} \tag{A-43}$$

where interaction parameters dF_{RF} and dF_{FR} are defined empirically.[2]

For $U \geq 0$:

$$dF_{FR} = [0.356 + 0.321R_{IF} - 0.368(R_{IF})^2 + 0.392(R_{IF})^3](1 - |\sin \beta'_F|) + [0.356 + 0.0131\, R_{IF} - 0.0764(R_{IF}) - 0.0085(R_{IF})^3]\, |\sin \beta'_F| \tag{A-44}$$

$$dF_{RF} = [0.356 - 0.151R_{IR} - 0.314(R_{IR})^2 + 0.164(R_{IR})^3]\, |\sin \beta'_R|) + [0.356 + 0.0131\, R_{IR} - 0.0764(R_{IR})^2 - 0.0085(R_{IR})^3]\, |\sin \beta'_R| \tag{A-45}$$

For $U < 0$:

$$dF_{RF} = [0.356 + 0.321R_{IR} - 0.368(R_{IR})^2 + 0.392(R_{IR})^3] (1 - |\sin\beta'_R|) + [0.356 + 0.0131R_{IR} - 0.0764(R_{IR})^2 - 0.0085(R_{IR})^3] |\sin\beta'_R| \quad \text{(A-46)}$$

$$dF_{FR} = [0.356 - 0.151R_{IF} - 0.314(R_{IF})^2 + 0.164(R_{IF})^3](1 - |\sin\beta'_F|) + [0.356 - 0.0131R_{IF} - 0.0764(R_{IF})^2 - 0.0085(R_{IF}) |\sin\beta'_F| \quad \text{(A-47)}$$

where for each rotor

$$R_I = \tan^{-1}\left(\frac{\mu}{\lambda - \lambda_I}\right) \quad \text{(A-48)}$$

$$\beta' = \tan^{-1}\left(\frac{v_H}{u_H}\right) \quad \text{(A-49)}$$

The thrust coefficients in Equation A-42, C_{TF} and C_{TR}, can be calculated through each rotor trim state, that is,

$$C_T = \frac{a\sigma}{2} \; T_c \quad \text{(A-50)}$$

Although T_c can be calculated by trimming the previously derived equations, Reference 2 has performed this analytically:

$$T_c = \frac{(\lambda - \lambda_I)}{2} + \frac{\theta_{oo}}{2} + \frac{\theta_T}{4} + \mu \left[\mu\left(\frac{\theta_{oo}}{2} + \frac{\theta_T}{4}\right) - \frac{\theta so}{2}\right] \quad \text{(A-51)}$$

The above equations represent a trancendental set for the solution of λ_{IF} and λ_{IR} and involve both front and rear rotor trim states.

Trim Calculations

Trim can be calculated by solving the previously derived equations, assuming the rigid body trim states are known. Reference 2 develops these equations for each rotor.

Coning angle:

$$\beta_{oo} = \frac{\gamma}{12}\left[4\,T_c + \frac{\theta_{oo}}{6} + \frac{\theta_T}{5} - \frac{\mu^2\beta_{oo}}{2}\right] \tag{A-52}$$

Longitudinal flap angle:

$$\beta_{co} = \frac{4}{\left[1 - \frac{\mu^2}{2}\right]}\left[\mu\frac{(\lambda - \lambda_I)}{2} + \frac{2}{3}\,\theta_{oo} + \frac{\theta_T}{2} - \frac{3}{8}\,\mu\theta_{so}) - \frac{\theta_{so}}{4}\right] \tag{A-53}$$

Lateral flap angle:

$$\beta_{so} = \frac{4}{3}\,\frac{\mu}{\left[1 + \frac{\mu^2}{2}\right]}\beta_{oo} + \beta_{co} \tag{A-54}$$

Control Input Coupling

The actual control inputs are collective (δ_C), differential collective (δ_B), longitudinal cyclic (δ_L), lateral cyclic (δ_S) and differential cyclic (δ_R). The derived control inputs θ, θ_c, and θ_s are related to these as follows:

$$\theta_{OF} = TDC\,\delta_C + TDB\delta_B \tag{A-55}$$

$$\theta_{OR} = TDC\,\delta_C - TDB\delta_B \tag{A-56}$$

$$\theta_{CF} = TDR\ \delta_R + TDS\delta_S \tag{A-57}$$

$$\theta_{CR} = TDR\ \delta_R - TDS\delta_S \tag{A-58}$$

Coupling to Rigid Body Equations

Although a complete set of equations of motion can proceed to include the full rigid body aerodynamics, the model was modified to utilize previously derived rigid body equations.[2] This allowed the use of trim data for the rigid body states, u_o, v_o, w_o, θ_o, and ϕ_o and the control inputs δ_{Bo}, δ_{Co}, δ_{So}, and δ_{Ro}.

Some modifications to the force and moment equations are also required. Because the HELCOP model in Reference 2 consists of perturbations of rigid body states to rigid body equations, the rigid body perturbations of Equations A-28 through A-37 need not be performed.

Deresidualization for Total Vehicle/Rotor Dynamics

Because the Reference 2 data includes rotor trim states and rigid body dynamics coupled through the rotor, the required vehicle/rotor coupling involves proper treatment of rigid body dynamics which "pass through" the rotors. This procedure is best explained using a state space formulation.

NASA has derived its HELCOP model in the following form:

$$\dot{x}_a = \tilde{F}x_a + \tilde{G}u \tag{A-59}$$

where

x_a is the rigid body state vector (eighth order)

$$x_a^T = (u_v, v_v, w_v, p_v, q_v, r_v, \theta_v, \phi_v)$$

u is the control vector

$$u^T = (\delta_B, \delta_C, \delta_S, \delta_R)$$

$\tilde{F}$ is the state coupler matrix

$\tilde{G}$ is the control coupler matrix

The current development is represented as

$$\begin{pmatrix} \dot{x}_a \\ \dot{X}_r \end{pmatrix} = \begin{pmatrix} F_{a,a} & F_{a,r} \\ R_{r,a} & F_{r,r} \end{pmatrix} \begin{pmatrix} x_a \\ x_r \end{pmatrix} + \begin{pmatrix} G_a \\ G_r \end{pmatrix} u \qquad \text{(A-60)}$$

where:

x_r is the rotor state vector (12th order)

$$x_r^T = (\beta_{OF}, \dot{\beta}_{OF}, \beta_{CF}, \dot{\beta}_{CF}, \beta_{SF}, \dot{\beta}_{SF}, \beta_{OR}, \dot{\beta}_{OR}, \beta_{CR}, \dot{\beta}_{CR}, \beta_{SR}, \dot{\beta}_{SR})$$

Because HELCOP uses rotor trim states, the NASA model A-59 is an implicit residualization of Equation A-60. Residualization of A-60 is performed by setting $\dot{x}_r$ to zero and solving for x_r:

$$x_r = -F_{r,r}^{-1} (F_{r,a} x_a + G_r u) \qquad \text{(A-61)}$$

This results in

$$\dot{x}_a = (F_{a,a} - F_{a,r} F_{r,r}^{-1} F_{r,a}) x_a + (G_a - F_{a,r} F_{r,r}^{-1} G_r) u$$

Comparing to Equation A-15 yeilds

$$\tilde{F} = F_{a,a} - F_{a,r} F_{r,r}^{-1} F_{r,a} \tag{A-62}$$

$$\tilde{G} = G_a - F_{a,r} F_{r,r}^{-1} G_r \tag{A-63}$$

The current situation, however, is peculiar in that we know $\tilde{F}$, $F_{a,r}$, $F_{r,r}$, $F_{r,a}$, G_a, and G_r but not $F_{a,a}$. The solution for $F_{a,a}$ can then be obtained using Equation A-60 by "deresidulizing" $\tilde{F}$:

$$F_{a,a} = \tilde{F} + F_{a,r} F_{r,r}^{-1} F_{r,a} \tag{A-64}$$

This then provides the missing part of our formulation. Equation A-16 could also be used to specify G_a; but this is already calculated. The equation therefore provides a useful validity check on the rotor modeling task.

Comparing $\tilde{G}$ of Equation A-63 with the calculated control effectiveness values of HELCOP was performed for key input parameters. Figures A-4 to A-12 contain some comparisons. Minor discrepancies can be attributed to numerical accuracy. Errors at high forward velocity (particularly $\dot{x}$ = 160 kn) are caused by the inability of the rotor modeling computer program to achieve perturbations on rotor interference parameters (see Equations B-42 and B-43 of Reference 2). These calculations are transcendental, and convergence on the wrong interference parameter for the 160-kn case results in gross errors in effectiveness values. For this reason, the rotor model

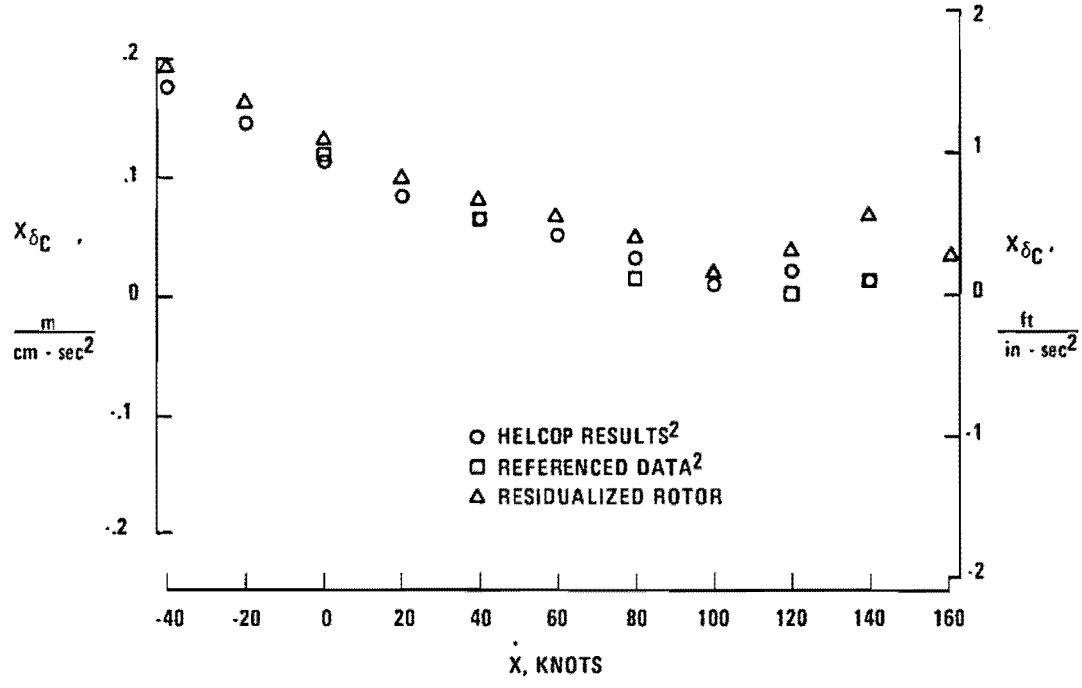

Figure A-4. X_{δ_C} Comparisons

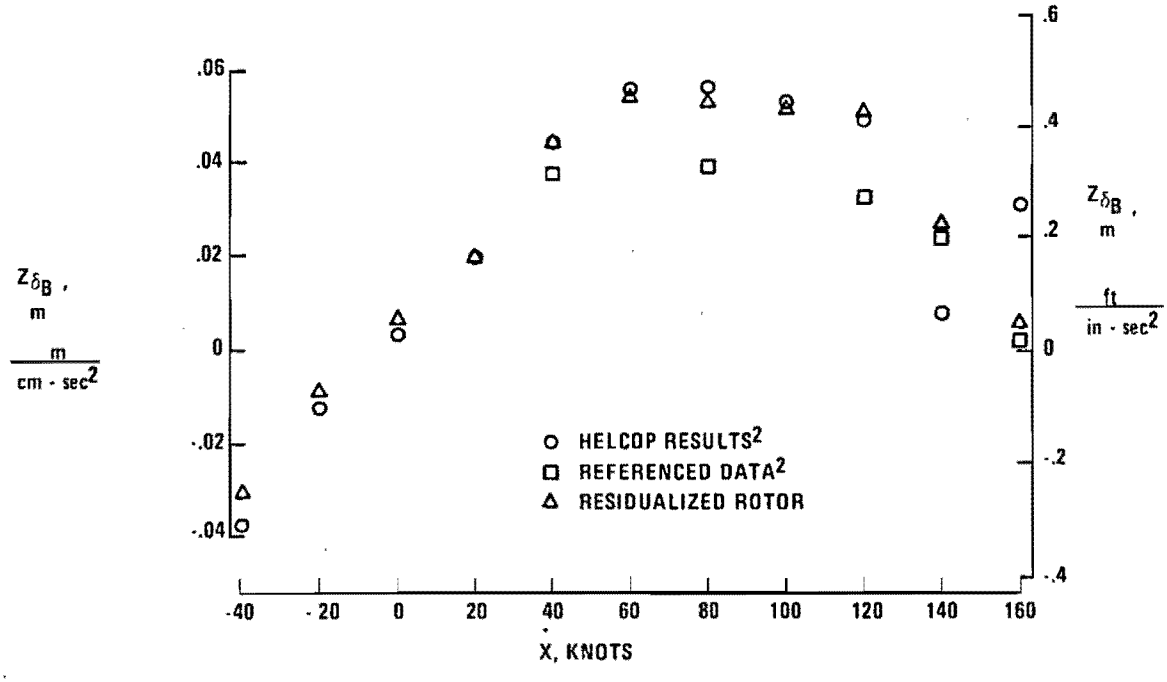

Figure A-5. Z_{δ_B} Comparisons

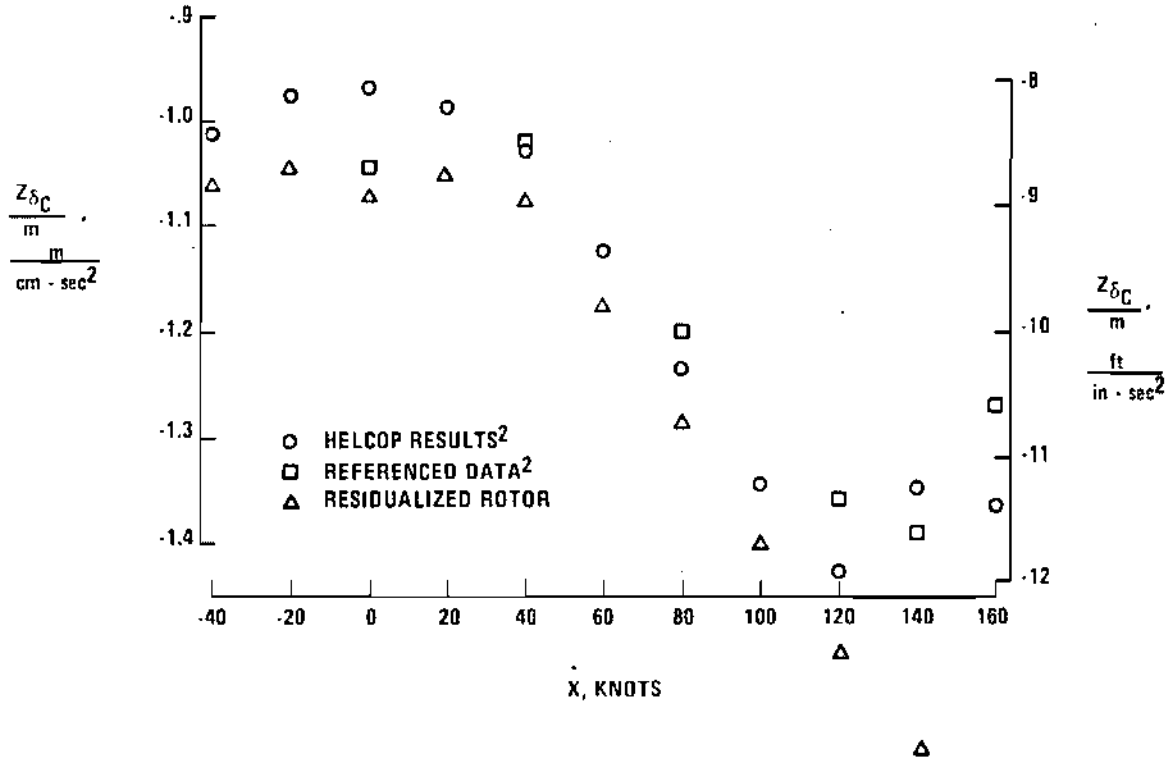

Figure A-6. Z_{δ_C} Comparisons

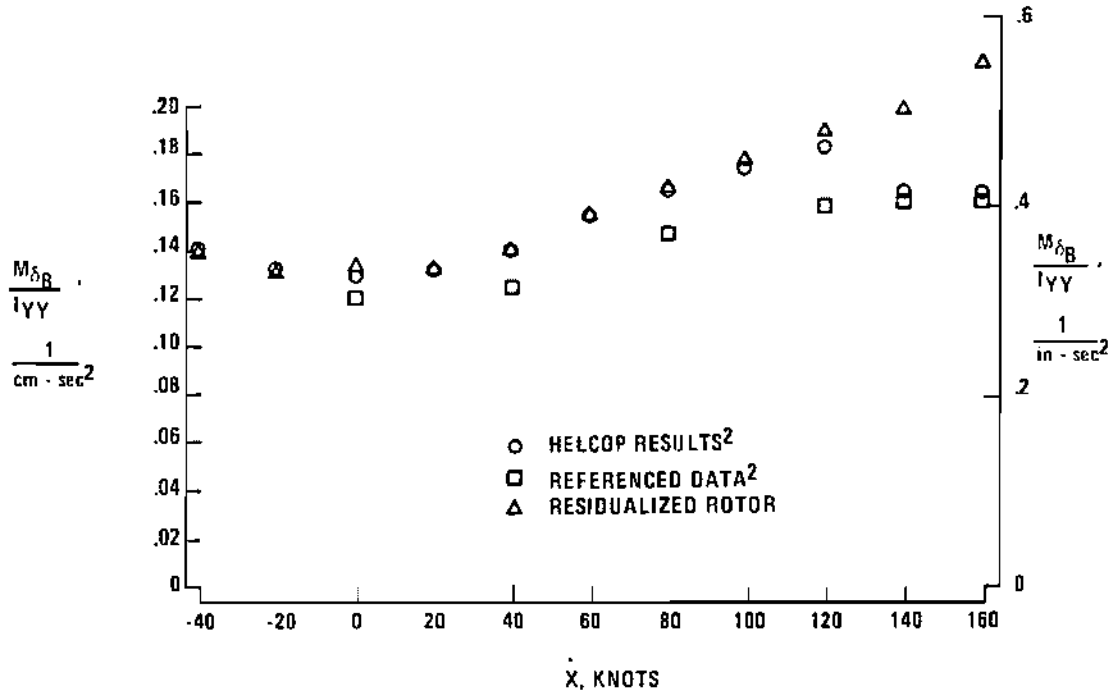

Figure A-7. M_{δ_B} Comparisons

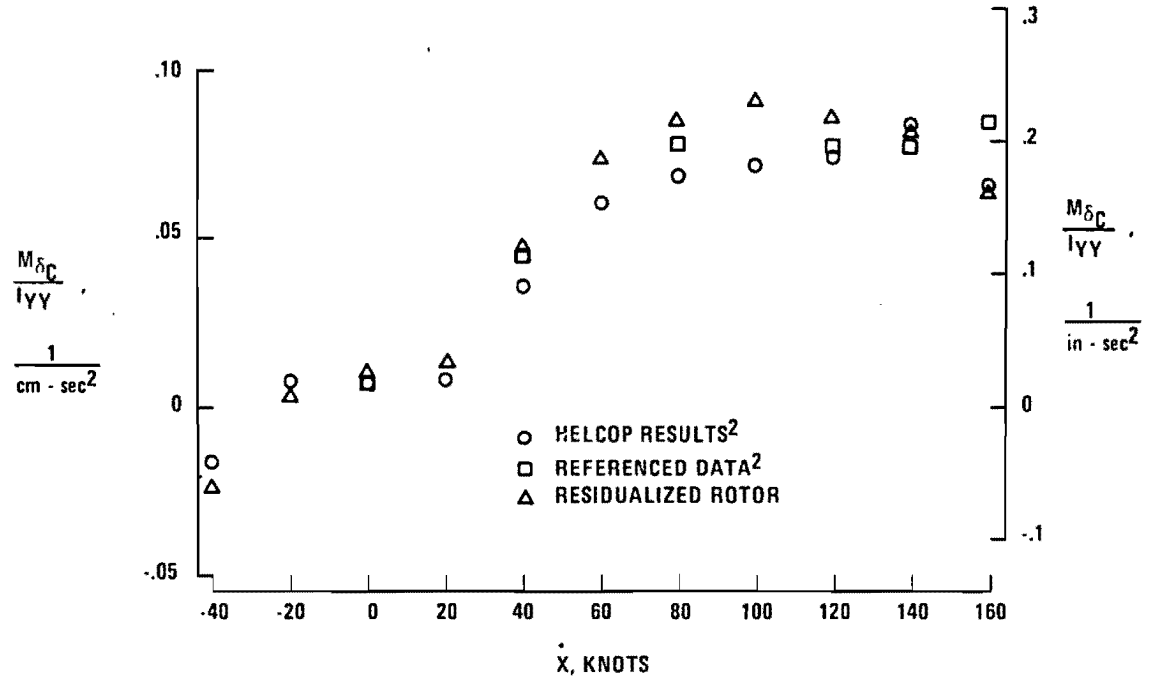

Figure A-8. M_{δ_C} Comparisons

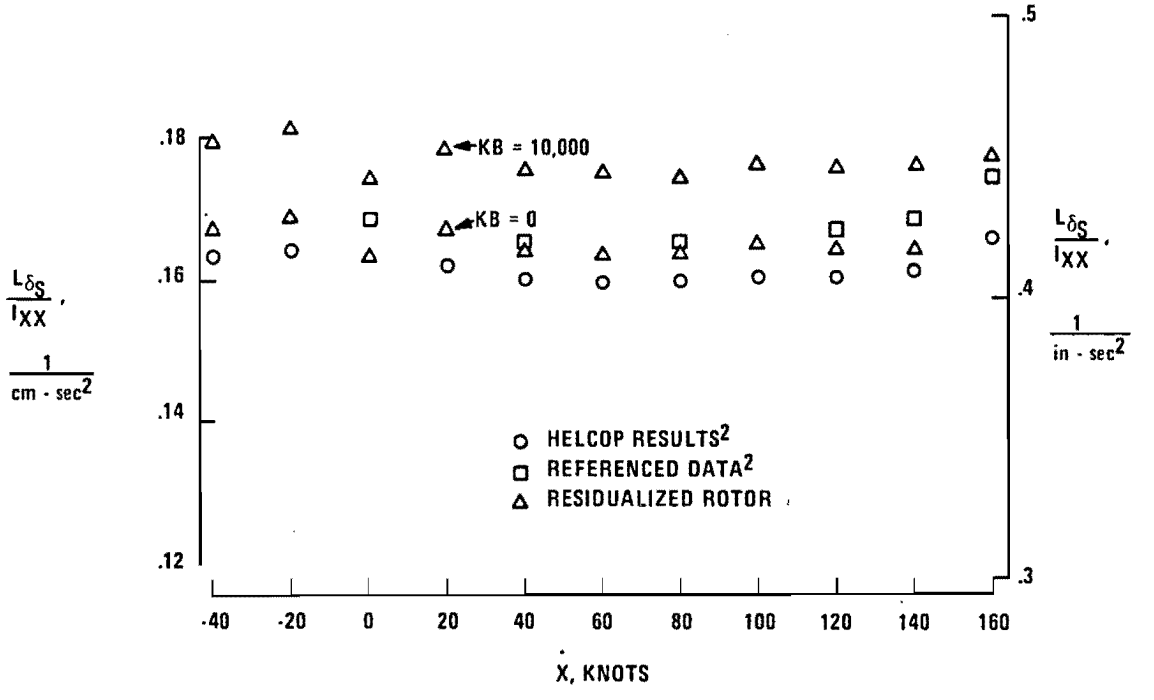

Figure A-9. L_{δ_S} Comparisons

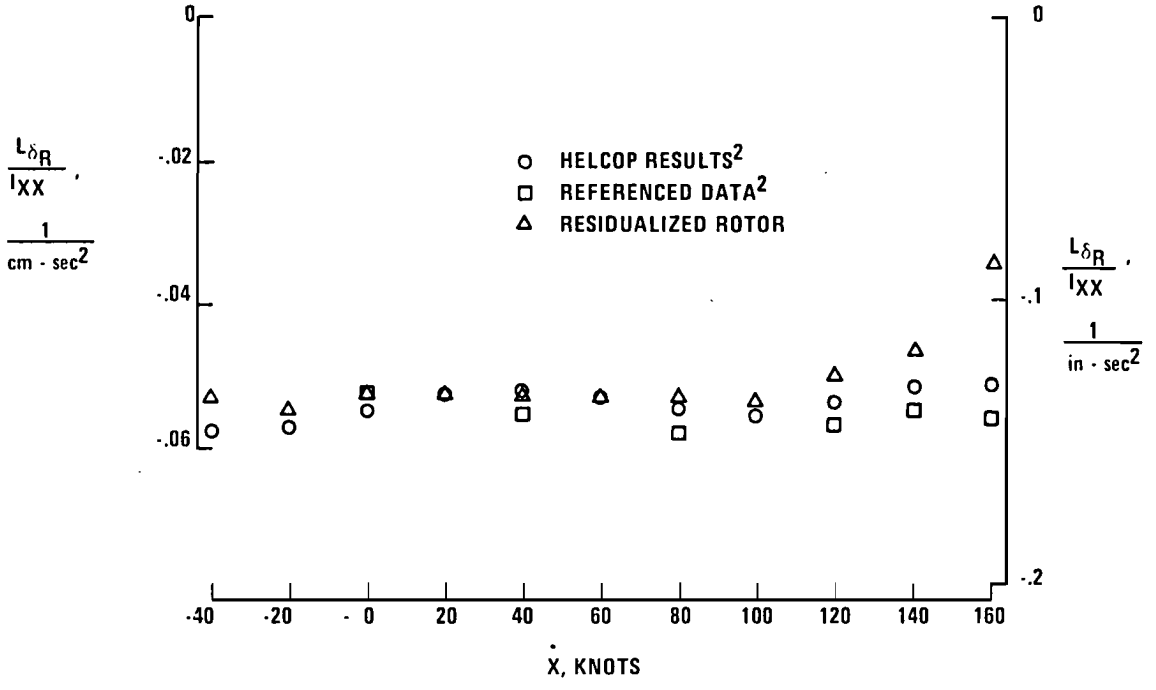

Figure A-10. $L_{\delta R}$ Comparisons

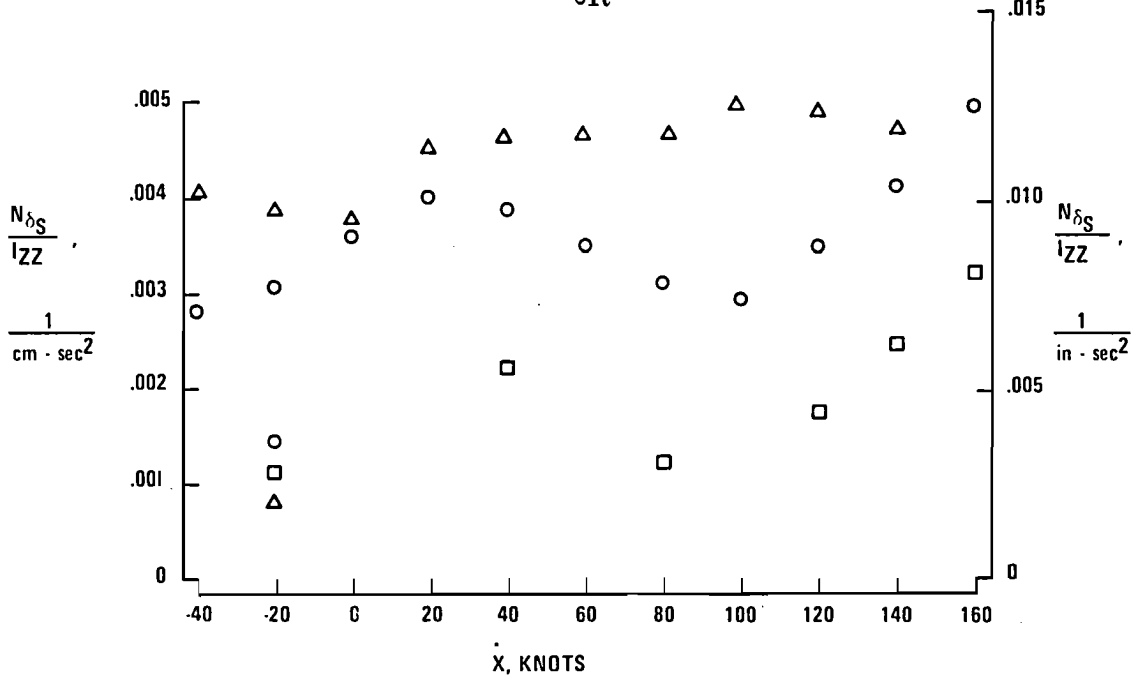

Figure A-11. $N_{\delta S}$ Comparisons

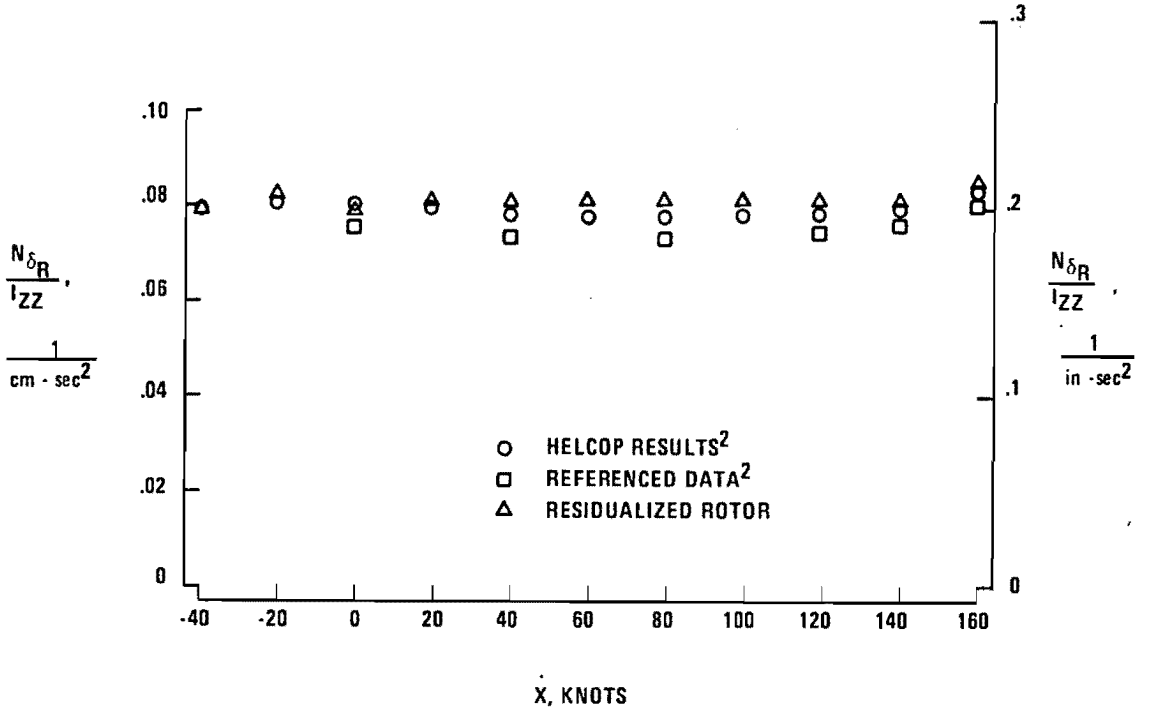

Figure A-12. $N_{\delta R}$ Comparisons

is considered suspect at airspeeds higher than 120 kn. This should pose little problem in control design as sufficient data exists for gain scheduling in the remaining flight conditions.

One interesting result concerns the value of L_{δ_S} in Figure A-9. A key roll parameter, the HELCOP derived values were consistently lower than reference data (although not significantly). The residualized rotor model results were consistently higher, as shown. The sensitivity of L_{δ_S} to the flapping spring constant, K_β, shows a definite impact of L_{δ_S}. Since HELCOP does not include this in its calculation, one can conjecture that the cause of the discrepancy between calculated and referenced results could be the effect of the flapping spring constant. One could further conjecture that the value of K_β = 10000 (an estimate used here) is too high.

One important parameter not shown is γ_{δ_s}. Because of the scaling used in Figure 13 of Reference 2, the current results could not be plotted. However, all values were approximately 15% low.

Rotor Measurements for Feedback Control

Selected designs in Section 3 utilize states of the rotor models for coning, β_{OF} and β_{OR}, and lateral flapping, β_{SF} and β_{SR}, to increase the control bandwidth. Because these are harmonic coefficients, they must be derived from the appropriate geometry of actual measurements. If we have a sensor measuring total flap angle on each blade of a three-bladed rotor, the appropriate states can be derived.

Let:

$$\beta_1 = \beta_0 - \beta_c \cos\psi - \beta_s \sin\psi$$

$$\beta_2 = \beta_0 - \beta_c \cos(\psi + 120°) - \beta_s \sin(\psi + 120°)$$

$$\beta_3 = \beta_0 - \beta_c \cos(\psi - 120°) - \beta_s \sin(\psi - 120°)$$

The simple algebra and trigonometry results in*

$$\begin{bmatrix} \beta_c \\ \beta_s \end{bmatrix} = \begin{bmatrix} \cos\psi, & -\sin\psi \\ \sin\psi, & \cos\psi \end{bmatrix} \begin{bmatrix} \dfrac{\beta_2 + \beta_3 - 2\beta_1}{3} \\ \dfrac{3}{2}(\beta_3 - \beta_2) \end{bmatrix}$$

This also requires that ψ be measured.

---

*This, of course, ignores higher harmonics, blade lagging, and flexure.

APPENDIX B

MODAL CONTROL DESIGN TECHNIQUES

Introduction

Modal control design is one of placing closed loop eigenvalues and eigenvectors for a given plant. The term modal refers to the mode design (pole placement) and the construction of system responses to these modes. The result is a design in which various system responses contain dynamics associated with desired roots or modes. For example, the lateral-directional axis of a fixed wing aircraft has three dominant modes, roll, dutch roll, and spiral. Pole placement algorithms can be used to change the roots of the closed loop system corresponding to each of these modes; however, unless aircraft responses are isolated from certain modes, the transient response of the system might not demonstrate the desired properties. The dutch roll root should dominate the β - R responses, the roll root should dominate the P response, and the spiral root should dominate the ϕ response.

Most aircraft contain some natural response decoupling, but existing pole placement algorithms do not account for this. System eigenvector placement provides the key additional design element.

Modal Control Overview

The design theory, based upon work done by Moore,[6] may be presented briefly as follows. Using state space notation

$$\dot{x} = Fx + Gu$$
$$y = Cx \tag{B-1}$$

where

$x(t) \epsilon R^n$; $u(t) \epsilon R^m$; $y(t) \epsilon R^p$

F, G, C have the appropriate dimensions and

rank (G) = m

rank (C) = $p \leq n$

An eigenvalue-eigenvector pair for a closed loop design for system B-1 is defined as

$$F_c v_i = \lambda_i v_i \tag{B-2}$$

where λ_i is one of the n eigenvalues, v_i is the corresponding eigenvector, and F_c is the closed loop plant matrix.

The λ_i, v_i pair can be achieved with control through the input matrix G; that is,

$$Fv_i + Gw_i = \lambda_i v_i \tag{B-3}$$

where w_i is a vector which satisfies the equation for the desired λ_i and v_i.

Case I: State Feedback

If we have access to all the states of the system, the feedback control law becomes

$u = Kx$

(assuming p=n and letting C=I without loss in generality)

and B-2 becomes

$$(F + GK)v_i = \lambda_i v_i \tag{B-4}$$

Matching B-4 with B-3, we must find w_i and K, which maps v_i into w_i.

$w_i = Kv_i$

For the entire collection of closed loop eigenvalues and eigenvectors, A-3 becomes

$$V\Lambda - FV = GW \tag{B-5}$$

where

$\Lambda \triangleq \text{diag}\,(\lambda_1, \lambda_2, \ldots \lambda_n)$ (nxn)

V is the eigenvector matrix (nxn)

W is the matrix which satisifes B-5 for Λ and V (mxm).

Likewise from B-4,

$$W = KV \tag{B-6}$$

therefore

$$K = WV^{-1*} \text{ (mxn)} \tag{B-7}$$

---

*Moore[6] demonstrates that rotating complex eigenvector pairs to real vectors produces a real K matrix which performs the desired placement.

Case 2: Output Feedback ($p<n$)

$$y = Cx$$

In this case Equation B-6 becomes

$$W = KCV \tag{B-8}$$

Since C is of rank $p<n$, a unique solution for K is impossible. The alternative used here is to choose only p eigenvalue-eigenvectors* to place; in other words, choose $p\lambda$'s and V (nxp) and solve for K such that

$$K = W(CV)^{-1} \text{ (mxp)} \tag{B-9}$$

Design Constraints

The key design issue is to find W, which satisifes B-8. In general, one cannot completely satisfy both exact eigenvalue and eigenvector placement.

Case 1: Single Input Systems

For single inputs Equation A-3 reduces to

$$(\lambda_i I - F)\, v_i = g w_i$$

where w_i is a scalar. Since this single variable must be adjusted to place n parameters on the left hand side, λ_i and n-1 parameters of v_i, the job is impossible. Therefore, the single input case only involves pole placement with arbitrary eigenvector position.

---

*There is no guarantee that the remaining closed loop system eigenvalues will be stable.

Case 2: Multiple Input Systems

The real benefit of modal control is employed when more than one control is available. The job becomes a matter of choosing the right w_i's in Equation A-3.

$$(\lambda_i I - F)v_i = Gw_i$$

The design procedure initially involves choosing portions of v_i in order to eliminate certain state responses from a mode while emphasizing others and letting other responses (control or compensation) react arbitrarily.

For Rank (B) = m, m free parameters can be specified, one of which is the eigenvalue. Equation B-3 can be rewritten

$$F_{ci}q_i = [(F - \lambda_i I),\ G]\, q_i = 0 \qquad n \text{ by } (n+m)$$

$$q = \begin{bmatrix} v_i \\ w_i \end{bmatrix} \tag{B-10}$$

q_i is therefore a null space mapping of F_{ci}. A convenient tool for finding the relationship between v_i and w_i is contained in the singular value decomposition of F_{ci}.[9]

The singular values of the matrix A_{ci} are the eigenvalues of $[A_{ci}\ A_{ci}^*]$, where * refers to the complex conjugate transpose. They are observed through the singular value decomposition of F_{ci}.

$$F_{ci} = X_i \Sigma_i Z_i^* \tag{B-11}$$

where:

X_i is an n-by-n matrix containing columns of orthogonal left singular vectors of F_{ci}

Σ_i is an n-by-n+m matrix containing n singular values, σ's, of A_{ci}

$$\Sigma_i = \left.\begin{array}{c} \left[\begin{array}{cccc|ccc} \sigma_1, & 0 & \cdots & 0 & 0 & \cdots & 0 \\ 0, & \sigma_2 & & & & & \\ \cdot & & \cdot & & & & \\ \cdot & & & \cdot & & & \\ \cdot & & & & \cdot & & \\ 0 & & & \sigma_n, & 0 & \cdots & 0 \end{array}\right] \\ \underbrace{\qquad\qquad}_{n} \quad \underbrace{\qquad\qquad}_{m} \end{array}\right\} n$$

$= [\overline{\Sigma}_i, [0]]$; $\qquad \overline{\Sigma}_i$ is nxn diagonal

Z_i is an n+m-by-n+m matrix containing n+m orthogonal right singular vectors of F_{ci}

By rearranging B-11

$$F_{ci} Z_i = X_i \Sigma_i \tag{B-12}$$

and noting that the last m columns of the $X_i \Sigma_i$ product are null, we find the appropriate null space for F_{ci} by using the last m columns of Z_i:

$$F_{ci} \overline{Z}_i = 0 \tag{B-13}$$

where $\overline{Z}_i$ is defined as

$$Z_i = \left.\left[\underbrace{\tilde{Z}_i}_{n}\ \underbrace{\overline{Z}_i}_{m}\right]\right\} n+m \tag{B-14}$$

The matrix $\overline{Z}_i$ is a set of m orthonormal basis vectors spanning the null space of A_{ci}. Referring to B-10, we have

$$q_i = \overline{Z}_i \alpha_i \tag{B-15}$$

where α_i is an m vector of linear coefficients not all of which can be zero.

Modal Control Algorithm

Returning to our original problem, we wish to specify the desired v_i and find a w_i which solves B-10. This cannot be done in general if $m<n$, therefore we formulate a least squares performance index

$$J = (v_{di} - v_i)^* Q(v_{di} - v_i) \tag{B-16}$$

where

v_{di} is the desired eigenvector

v_i is the resulting admissible vector subject to the constraint B-10.

Replacing v_i in B-15 with

$$v_i = E\,\overline{Z}_i \alpha_i$$

where

E is an n-by-n+m matrix

$$E \triangleq \underbrace{[I,\ 0]}_{n\ \ m} \Big\} n$$

and minimizing B-16 with respect to α_i

$$\alpha_i = \mathrm{Arg}[\min J]$$
$$= (\overline{Z}_i^* E^T Q E\overline{Z}_i)^{-1} \overline{Z}_i^* E^T Q V_{di} \tag{B-17}$$

the appropriate W_i is found using B-15.

$$W_i = \overline{E}\,\overline{Z}_i\alpha_i = \overline{E}\overline{Z}_i(\overline{Z}_i^* E^T Q E\overline{Z}_i)^{-1} \overline{Z}_i^* E^T Q V_{di} \tag{B-18}$$

where $\overline{E}$ is an m-by-n+m matrix

$$\overline{E} \triangleq \underbrace{[0,\ I]}_{n\ \ m} \Big\} m$$

Referring to B-16, it should be noted that one could try to fit the n elements of v_i to a prespecified n elements of v_{di}. Unless v_{di} happens to lie in the m-dimensional subspace of w_i, a perfect fit is impossible. As a practical matter one should specify up to m elements of v_{di} and let the other elements be arbitrarily placed. This is performed by the proper choice of Q, that is, by placing the desired quadratic weights only in diagonal elements corresponding to element locations in v_{di} which are to be placed. The example which follows demonstrates this.

Illustrative Example: F-4 Lateral-Directional Axis

The design of an inner loop control law for the F-4 lateral-directional axis was undertaken to illustrate the multivariable optimal control design procedures developed under an ONR sponsored contract.[7] Much of the problem description is repeated here because the eigenvalue-eigenvector design goals are identical.

The F-4 fighter aircraft at a low dynamic pressure flight condition is taken from Reference 8. The dynamics are

$$\dot{x} = Fx + Gu$$

with

$$x = \begin{bmatrix} p_s \\ r_s \\ \beta \\ \phi \\ \delta_r \\ \delta_a \end{bmatrix} \begin{array}{l} \text{stability axis roll rate} \\ \text{stability axis yaw rate} \\ \text{angle of sideslip} \\ \text{bank angle} \\ \text{rudder deflection} \\ \text{aileron deflection} \end{array}$$

$$u = \begin{bmatrix} \delta_{rc} \\ \delta_{ac} \end{bmatrix} \begin{array}{l} \text{rudder command} \\ \text{aileron command} \end{array}$$

Matrices F and G are

$$F = \left[\begin{array}{cccc|cc} -.746 & .387 & -12.9 & 0. & .952 & 6.05 \\ .024 & -.174 & 4.31 & 0. & -1.76 & -.416 \\ .006 & -.9994 & -.0578 & .0369 & .0092 & -.0012 \\ 1. & 0. & 0. & 0. & 0. & 0. \\ \hline 0. & 0. & 0. & 01. & -20. & 0. \\ 0. & 0. & 0. & 0. & 0. & -10. \end{array}\right]$$

$$G = \left[\begin{array}{cc} 0. & 0. \\ 0. & 0. \\ 0. & 0. \\ 0. & 0. \\ \hline 20. & 0. \\ 0. & 10. \end{array}\right]$$

Open Loop Poles

λ roll subsidence = -.079

λ dutch roll = -.098 $\pm$ j2.079

λ spiral = -.0063

λ rudder actuator = -20.0

λ aileron actuator = -10.0

An initial condition response for the open loop system is shown in Figure B-1.

From the point of view of fighter handling qualities, all four of the lateral axis closed loop roots have desired values which can be taken from MIL-F8785B, as is done, for example, in Reference 9. The desired roots are:

a) Roll subsidence mode = -4.0

b) Dutch roll mode = -0.63 $\pm$ j2.42

c) Spiral mode = -0.05

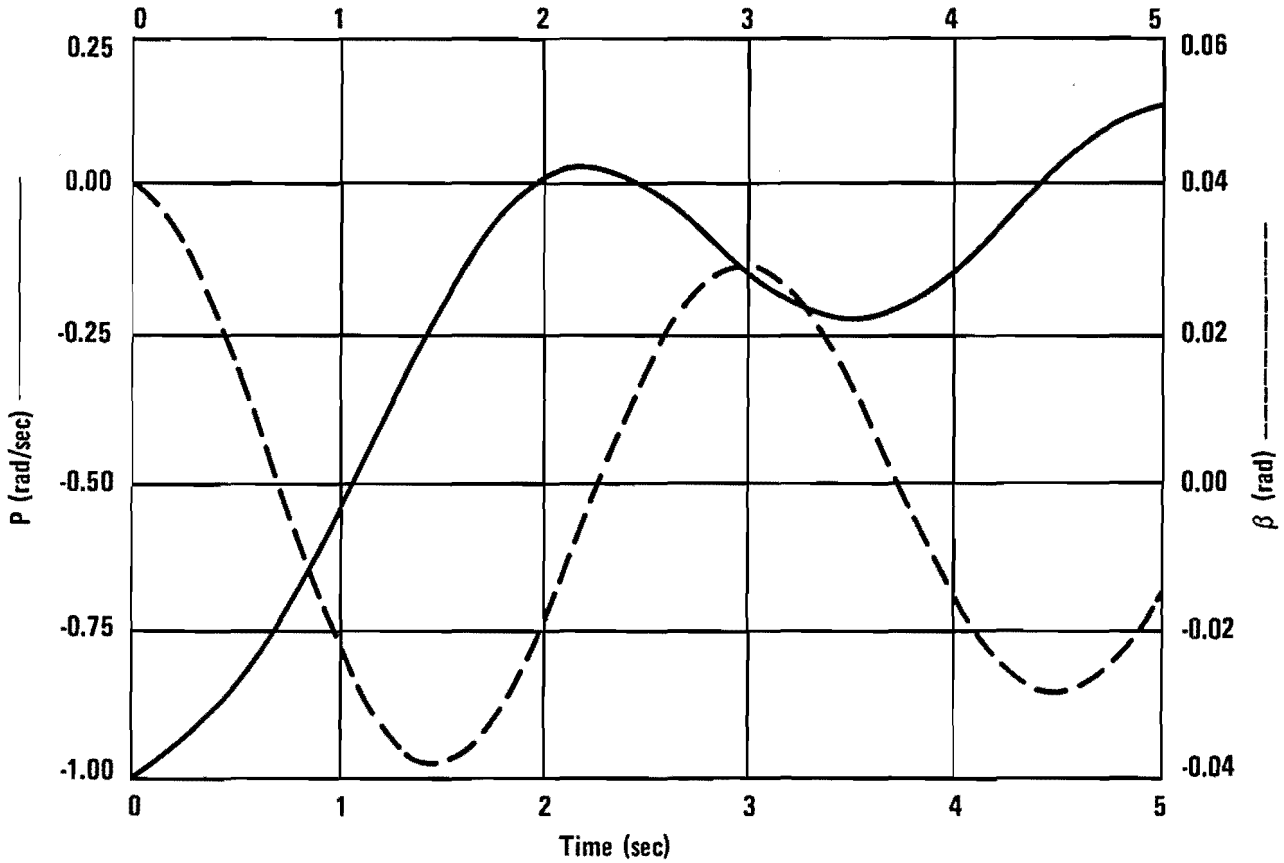

Figure B-1. F-4 Lateral-Directional Open Loop Response

Each of these poles can be assigned an asymptotic eigenvector, v_i, which distributes the modal response, $e^{\lambda_i t}$, among the state variables and outputs of the system. However, each eigenvector is constrained to lie in a two-dimensional subspace (page 16, Reference 7). An element of this subspace was selected by using B-18 to find the best linear projection of an unconstrained desired vector, v_{di}, on the subspace. The results of the eigenvector selection are:

a) Roll subsidence mode ($e^{-4t}v_1$)

Desired v_{d1} = [1. 0 0 a a a]

Attainable v_1 = [1. -.007 0 -.25 .13 -.56]

b) Dutch roll mode, real part $\left(e^{-.63t}(\cos 2.42t)v_2\right)$

Desired v_{d2}	= [0	a	1.	0	a	a]
Attainable v_2	= [0	15.6	1.	0	7.86	-.103]

c) Dutch roll mode, imaginary part $\left(e^{-.63t}(\sin 2.42t)v_3\right)$

Desired v_{d3}	= [0	1.	a	0	a	a]
Attainable v_3	= [0	1.	6.16	0	-9.49	14.6]

d) Spiral mode $\left(e^{-.05t}v4\right)$

Desired v_{d4}	= [a	a	0	1.	a	a]
Attainable v_4	= [-.05	.037	0	1.	-.0014	-.0079]

A few comments are in order to explain these choices. Consider, for example, the roll subsidence mode. The desired eigenvector is taken to be v_{dl} = (1 0 0 a a a), which means that the mode should show up dominantly on roll rate, but not on yaw rate or sideslip (we want no sideslip buildup during turn entries). These are good basic handling quality considerations. The a's in the vector indicate that we do not care how much of the mode shows up on these components. Certainly, since $\phi = \int p_s dt$, some mode content has to be expected on element a_4 and, similarly, if the surfaces are actually controlling the mode, some mode content should also appear in a_5 and a_6. The linear projection which best achieves these objectives is shown as v_i above. Note that we can satisfy our desires almost perfectly.

Similar arguments also apply to the dutch roll mode. In this case we want no oscillatory dutch roll content on roll rate and bank angle. This is a key handling quality requirement for all well-behaved lateral control laws.[8]

This output feedback problem poses little difficulty using modal control techniques since we wish only to place four eigenvalue-eigenvector sets. Actually there is concern for the remaining two poles. It is desirable to avoid moving these remaining poles too far to the left, which would hint at high actuator demands. The control design gives us a bonus here if the measurement vector contains no actuator states; in other words,

$$y = [C, 0] \begin{bmatrix} X \text{ vehicle} \\ X \text{ actuator} \end{bmatrix}$$

Since the form of the open loop system matrix F is

$$F = \begin{bmatrix} F_{11}, & F_{12} \\ 0 \quad , & F_{22} \end{bmatrix}$$

then the closed loop system matrix F_c is

$$F_c = \begin{matrix} F_{11}, & F_{12} \\ BKC, & F_{22} \end{matrix}$$

The trace of a matrix is the sum of the eigenvalues; therefore,

$$\sum_{i=1}^{n} \lambda_{ci} = \text{trace } F_c = \sum_{i=1}^{n} \lambda_i = \text{trace } F$$

The sum of the closed loop eigenvalues is equal to the sum of the open loop eigenvalues. This becomes important if our design goal involves moving plant poles to the left (which is usually the case), because it requires that the remaining eigenvalues of the closed loop system move to the right. Since the "remaining" eigenvalues are our "actuator poles" (roughly speaking), we are assured that they do not increase in magnitude.

Design Results

Case I: Vehicle State Feedback

Using the vehicle states listed earlier,

$$y^T = (p_s, r_s, \beta, \phi)$$

Perfect pole placement was achieved (as guaranteed by earlier analysis) and the eigenvectors which we found to be achievable were obtained. The remaining poles move to the right as expected.

$$\lambda_5 = -19.03 \text{ (formerly -20)}$$

$$\lambda_6 = -\ 6.64 \text{ (formerly -10)}$$

An initial condition response, shown in Figure B-2, verifies the eigenvector response isolation desired. This is virtually identical to the results of the ONR design study,[7] which used optimal feedback control, although some minor pole movement was observed in the later design when actuator gains were eliminated.

Case II: Practical Output Feedback

Although β feedback is possible it is usually not advisable because of the difficulty of obtaining good side slip data. A more reasonable approach is to use lateral acceleration instead. This is not a trivial linear transformation, since the measurement includes actuator states. Also, our nice property of invariant eigenvalue sums is no longer valid.

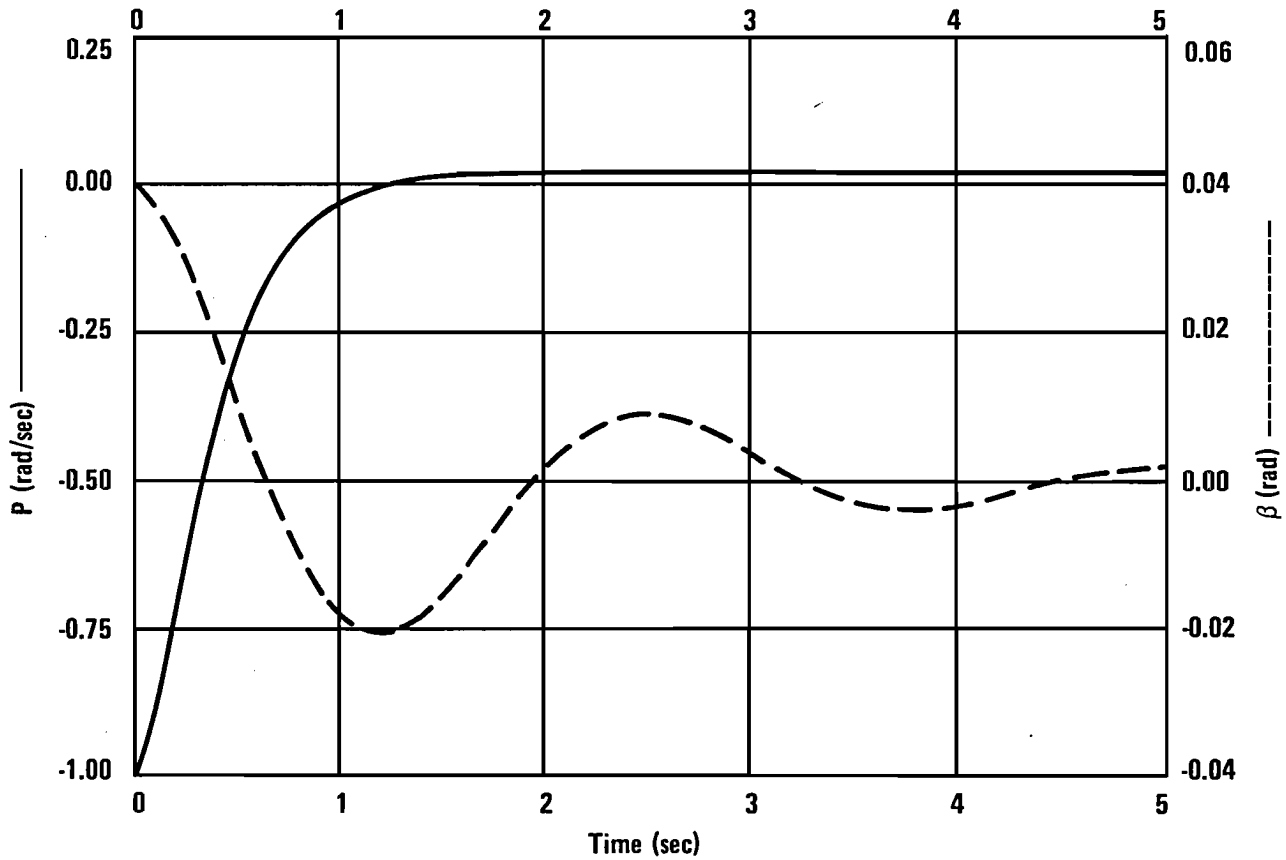

Figure B-2. Closed Loop Design: Cases 1 and 2

Using the output vector

$$y^T = (p_s, r_s, n_y, \phi)$$

we achieved the same desired "vehicle" poles and eigenvectors as in Case I (as we should) plus two additional poles at

$$\lambda_5 = -15.82$$

$$\lambda_6 = -\ 5.98$$

Although not guaranteed, the two additional poles move even further to the right than in Case I.

The initial condition response is virtually identical to that in Case I (Figure B-2).

Case III: Reduced Measurement Set

Another practical alternative is to eliminate more sensors (in other words, save $'s) and go for the same design goals. One logical candidate would be the roll attitude gyro (measuring ϕ). In modal control this would require placing one fewer pole (and eigenvector). The logical candidate here would be the spiral mode (λ spiral desired = -.05).

Results were impressive, with the initial condition response (Figure B-3) showing little impact from this change. A slight decrease in dutch roll damping is observed when Figures B-2 and B-3 are overlaid. Additional eigenvalues are

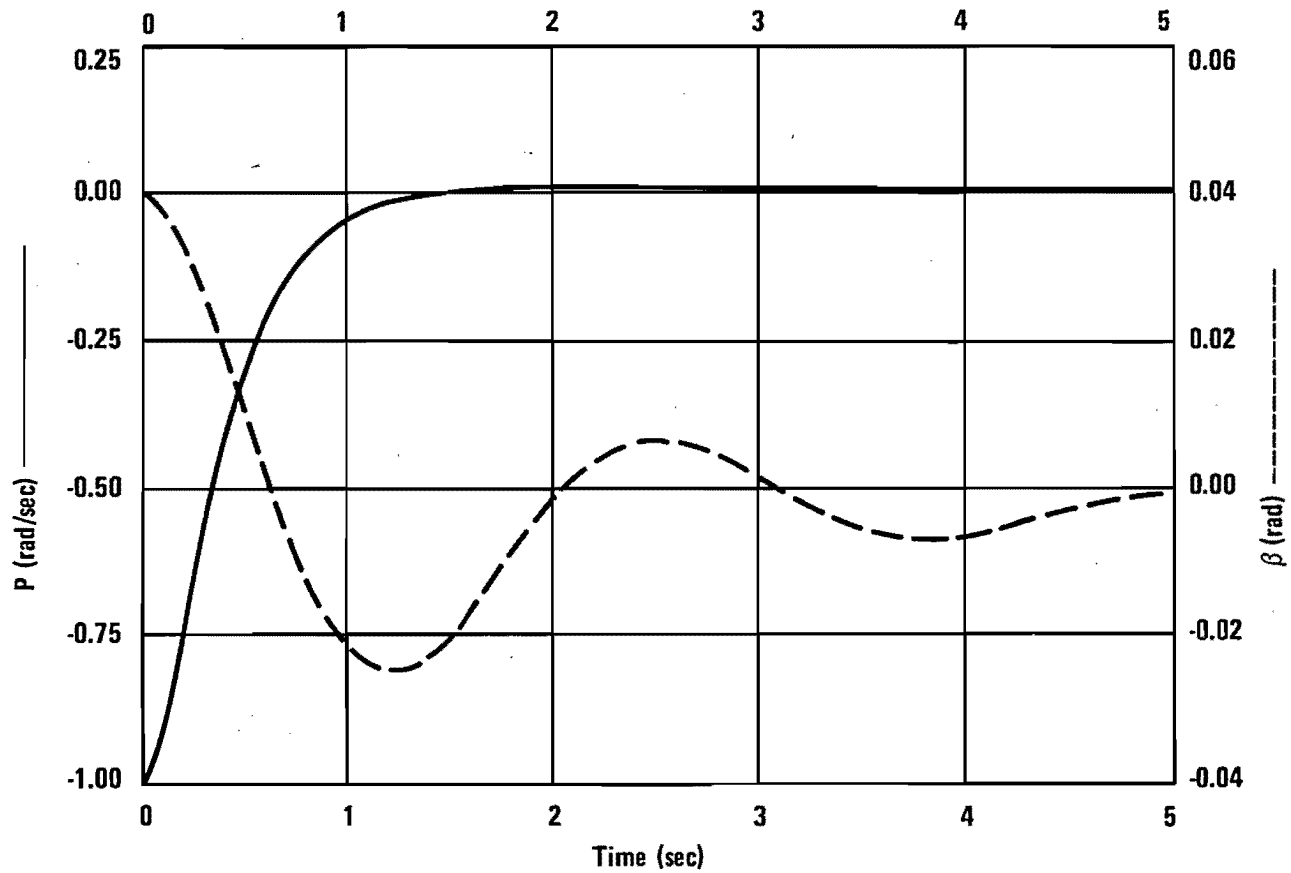

Figure B-3. Closed Loop Design: Case 3

$\lambda_{spiral} = -\ .023$

$\lambda_5 = -15.83$

$\lambda_6 = -\ 5.99$

The spiral root does not meet our objective of -.05; however, it is unlikely that this value would produce significant comments from rating pilots. Even slightly unstable spiral roots are usually acceptable.

Further Measurement Reductions

If our sensor coffer is poor and we need to eliminate yet another measurement (or the last one of a kind fails) let us see what we get.

$$\text{Case IV: } y^T = (r,\ n_y)$$

In this case the logical design goal to eliminate is the roll subsidence mode, since we are no longer using the roll rate gyro to measure p_s.

Design results place the dutch roll pair exactly and produce the following remaining poles:

$\lambda_{roll\ subsidence} = -\ 2.54$ (-4.0 was our earlier goal)

$\lambda_{spiral} = -\ .296$ (-.05 was our earlier goal)

$\lambda_5 = -16.00$

$\lambda_6 = -\ 7.27$

The transient response is shown in Figure B-4. The impact of the roll subsidence and spiral modes on the dutch roll is obvious (decreased damping). The important factors are:

1. The dutch roll oscillation is not contained in the roll response because the dutch roll eigenvector placements preclude this.

2. The response is still a vast improvement over the open loop case.

$$\text{Case V: } y^T = (p_s, r_s)$$

This case is much more difficult because no logical fallback on our design goals exist, that is, we cannot place half of a complex pair. Therefore, it was decided to try and place the dutch roll mode (as in Case IV).

Modal control guarantees the prescribed pole and eigenvector placement (since our earlier analysis showed it was feasible). Other results, however, demonstrate the disadvantages of this:

$$\lambda_{3,4} = -4.62 \pm j19.63$$

$$\lambda_5 = -.0047$$

$$\lambda_6 = -20.47$$

The transient response is not shown because the design is obviously unacceptable. The point here is that an unreasonable task was required, given the current sensor/hardware configuration. (We actually got what we asked for, but should we have asked?)

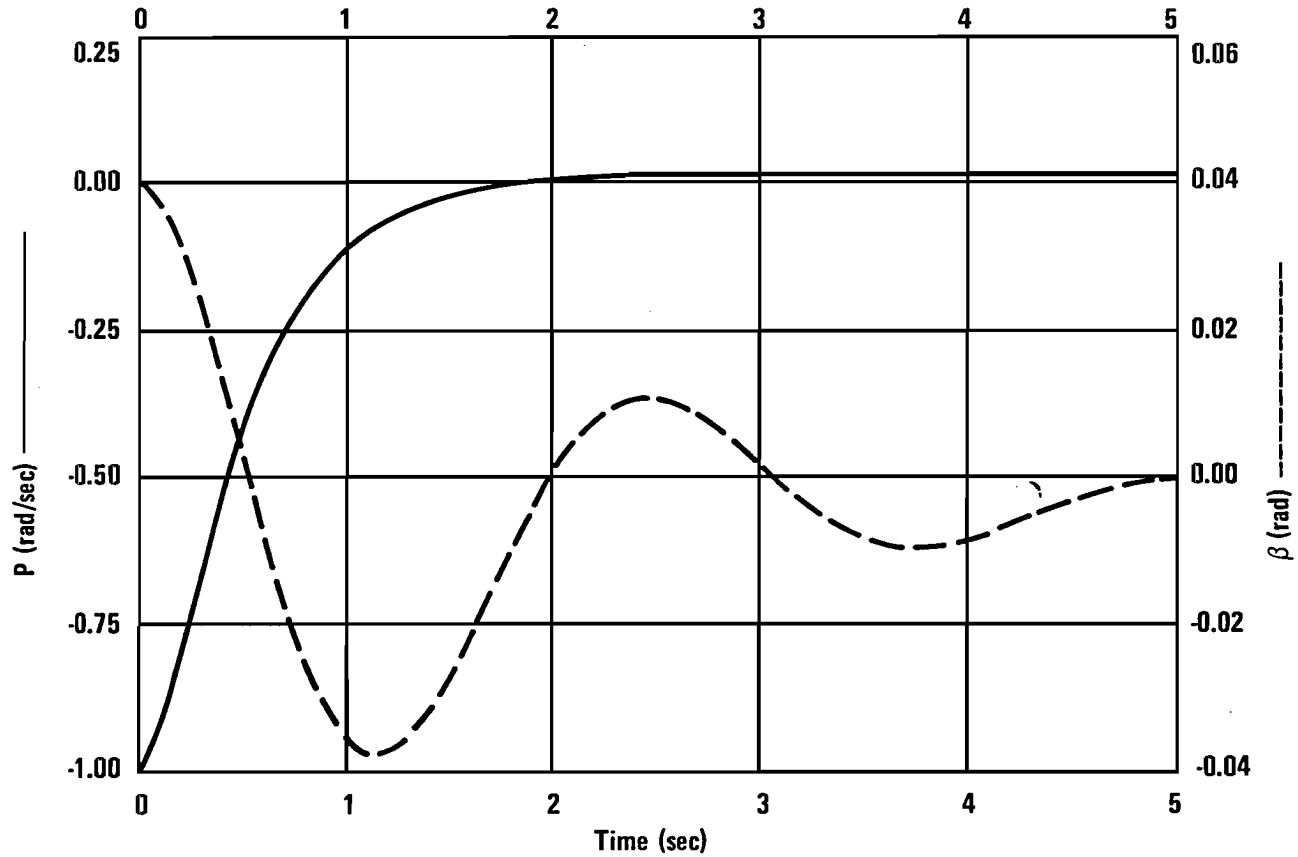

Figure B-4. Closed Loop Design: Case 4

Conclusions

In this appendix modal control is developed from its conceptual foundation (provided in Reference 6) to a practical design tool through partial eigenvector placement techniques (developed in Reference 7). The F-4 lateral-directional axis design example demonstrates the usefulness of this design method to perform precision mode shaping and tradeoff studies.

APPENDIX C

CH-47 MODEL TESTS

Introduction

This appendix contains results of the control systems tests conducted on the NASA-Langley research vehicle CH-47B. Included are static and dynamic tests conducted in the hangar plus results of tests conducted in hover and cruise flight.

The purpose of these tests was to provide a check on the dynamics of various control system elements, including the presence of any nonlinearities. A reasonably accurate model of the control system is needed to permit continuing investigation into ways and means of improving the gain and bandwidth capabilities of the system.

Static and dynamic measurements on some portions of the system could be conducted in the hangar with hydraulic and electric power-on but rotors stationary. A function generator (sine, square, or triangle) was used to introduce signals of appropriate amplitude and frequency into the ECS servo. A seven-channel strip chart recorder was used to record ECS servo position and/or upper boost actuator position, as well as the forcing function. For the hysteresis tests, an X-Y recorder was used.

It was not possible to measure the frequency response to include the upper boost actuators in the hangar because of the excessive flopping of the rotor blades produced in the non-rotating, unloaded condition. These were obtained under hover and cruise flight conditions, with the results recorded by the

special on-board instrumentation and magnetic tape recording system. Static control system perturbation gains were obtained from the low frequency response data at hover and corrected for hysteresis.

During all tests, the normal ships SAS system was disabled to prevent interference with the measurements. This was accomplished by making changes to the SAS servo wiring so that one servo was caused to go hardover in the fully extended position while the other servo was fully retracted. They therefore cancelled one another in the linkage while each still acted as a rigid link, with no affect on the control system dynamics.

CH-47B Control Characteristics

Nominal Control Characteristics

The CH-47 flight control system uses mechanical linkages, hydraulic boost actuators, and complex mechanical mixers to transmit pilot control motions to the rotor swash plates. The resulting control system model can be represented by a relatively simple block diagram, as shown in Figure C-1. This diagram includes effects of backlash in the linkage and presents the static and dynamic relationships and scale factors determined in this investigation.

The ECS servo is not part of a normal CH-47 control system but was added to this research vehicle in a prior program. It permits the introduction of electrical commands from whatever source desired into the control system. It operates as a parallel servo with the safety pilot's manual controls when a connecting clutch is engaged. This enables the safety pilot to quickly regain control by de-clutching the ECS servo when conditions warrant.

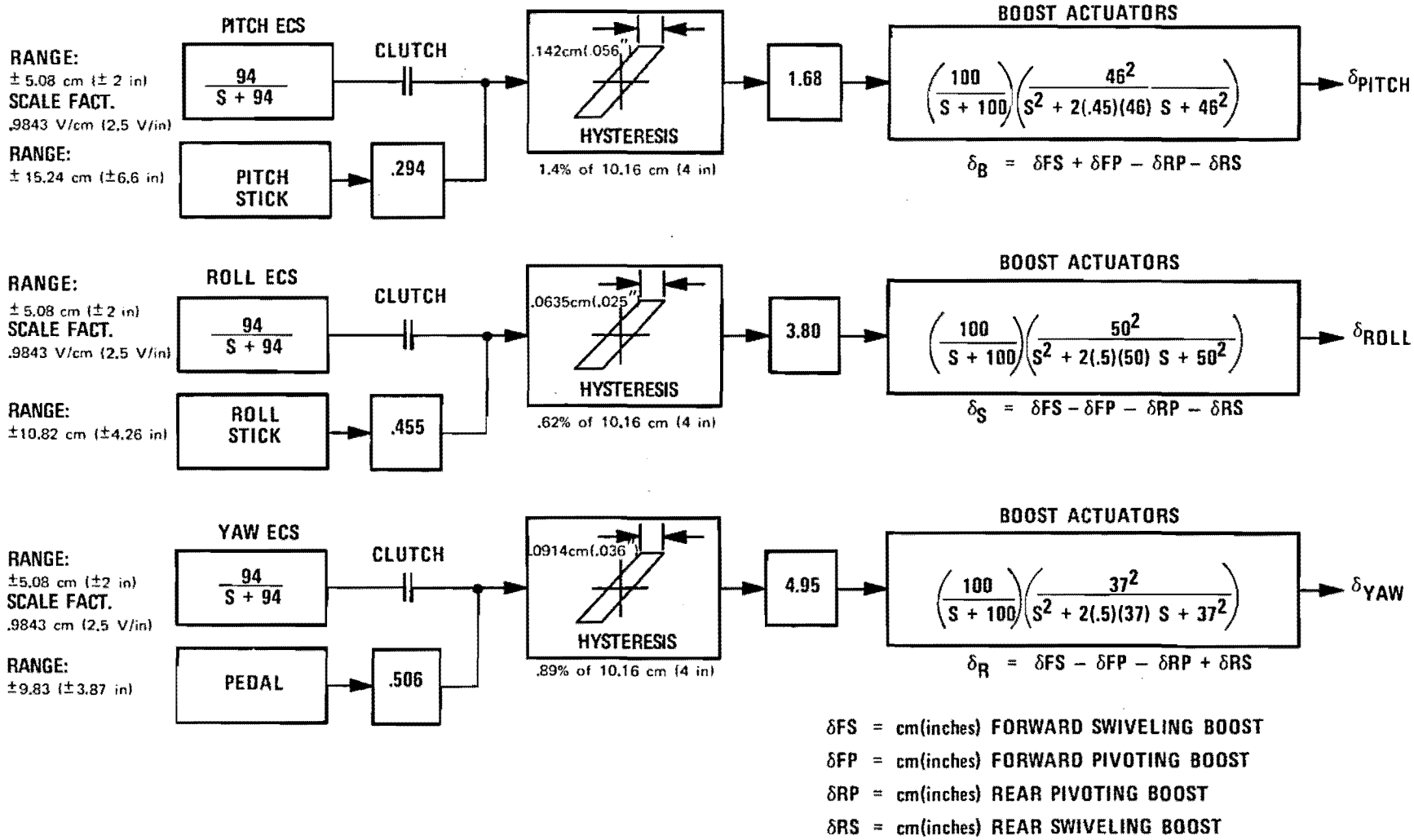

Figure C-1. CH-47B System Block Diagrams

The gains shown relate ECS or safety pilot control stick motion to the net sum of the upper boost actuator motions by axis. For example, 1 cm roll ECS servo motion produces 3.9 cm of delta roll; this is the summation, as is shown in Figure C-1 of the four upper boost actuators in response to roll commands.

ECS Servo Characteristics

The ECS servos in the pitch, roll, and yaw axes were each checked at three amplitudes for frequency response, rate limits, and nonlinearities. The ECS was de-clutched from the rest of the control system during these tests.

Measured Frequency Responses. - Frequency response data was recorded for the range 0.25 to 20 Hz and at peak amplitudes of ±2.5%, ±5%, and ±10% of the servo stroke of ±5.08 cm (±2 inches). Rate limiting was encountered at the higher frequencies, depending upon stroke amplitude. The results of these measurements are presented in Table C-1.

No Linearities. - Linearity and backlash of the ECS servo was evaluated by driving it with a 0.1 Hertz triangle wave and recording input vs. output on an X-Y recorder. The results are presented in Figures C-2 and C-3. It should be noted that the transfer is essentially a straight line with negligible gap between the forward and return stroke.

Rate Limits. - During the frequency response tests, rate limiting was encountered at the 5% and 10% strokes at the higher frequencies. Analysis of these conditions revealed the rate limits shown in Table C-2.

TABLE C-1. ECS SERVO FREQUENCY RESPONSE DATA

INPUT		PITCH		ROLL		YAW	
Frequency Hertz	Amplitude % Stroke	Amplitude DB	Phase Deg.	Amplitude DB	Phase Deg.	Amplitude DB	Phase Deg.
.25	2.5	0	0	0	0	0	0
.5		0	0	0	0	0	0
1		0	0	0	0	0	0
2.5		-.2	-10	-.2	-5	-.2	-10
5.		-.2	-20	-.28	-15	-.36	-20
10.		-1.1	-35	-.98	-30	-.64	-25
20.		-4.4	-55	-3.6	-55	-3.4	-50
.25	5	0	0	0	0	0	0
.5		0	0	0	0	0	0
1.		0	0	0	0	0	0
2.5		0	-5	-.2	-5	-.1	-5
5.		0	-15	-.2	-15	-.18	-15
10.		-3.3	-55	-3.0	-55	-2.9	-55
		rate limit		rate limit		rate limit	
2.5	10	0	0	0	0	0	0
.5		0	0	0	0	0	0
1.		0	0	0	0	0	0
2.5		0	-5	-.2	-5	0	-5
.5		-3.1	-45	-2.7	-45	-3	-45
		rate limit		rate limit		rate limit	

Notes: Amplitude ratios and phase read from strip chart recordings. Phase stated to nearest 5 deg.

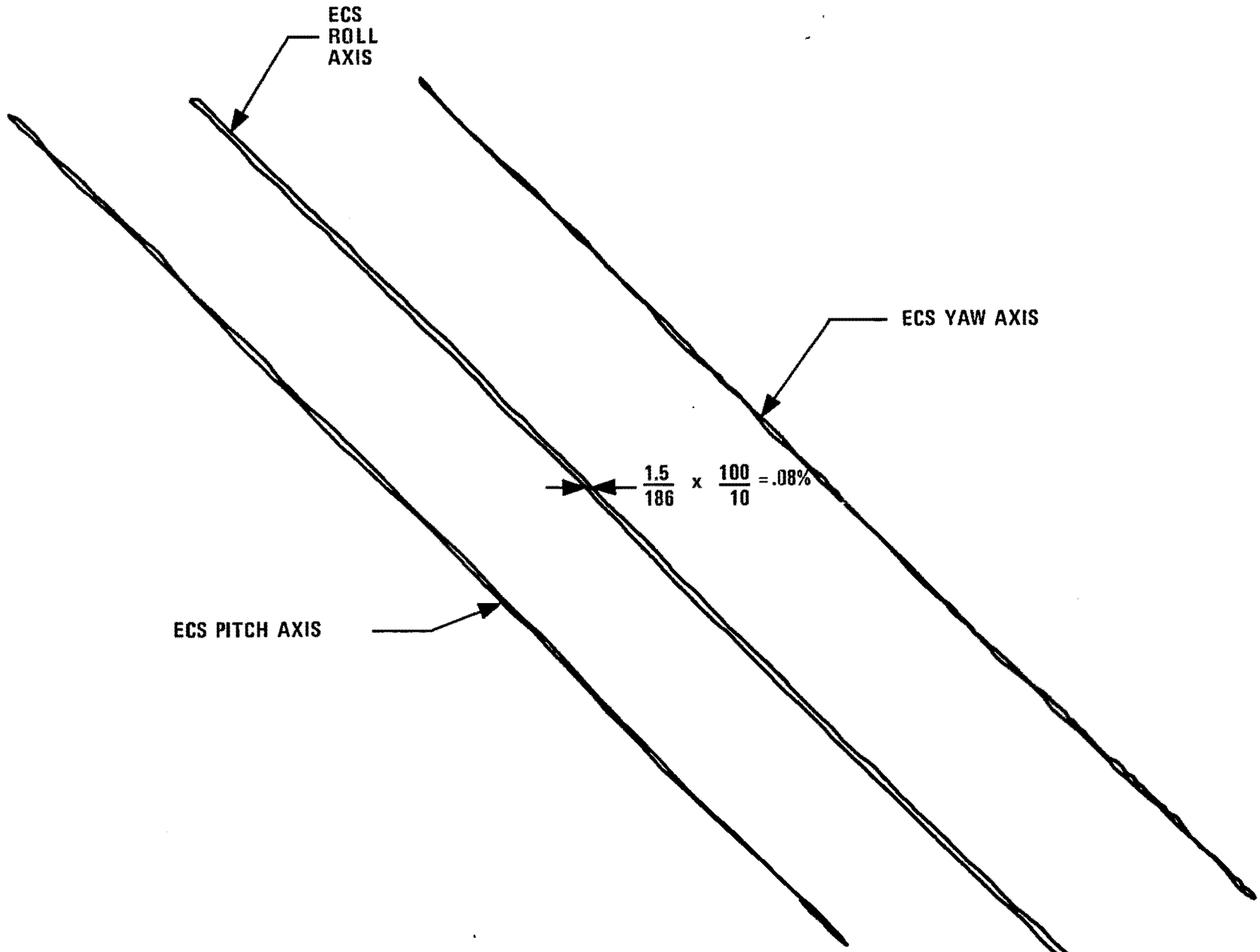

Figure C-2. ECS Servo Non-Linearities

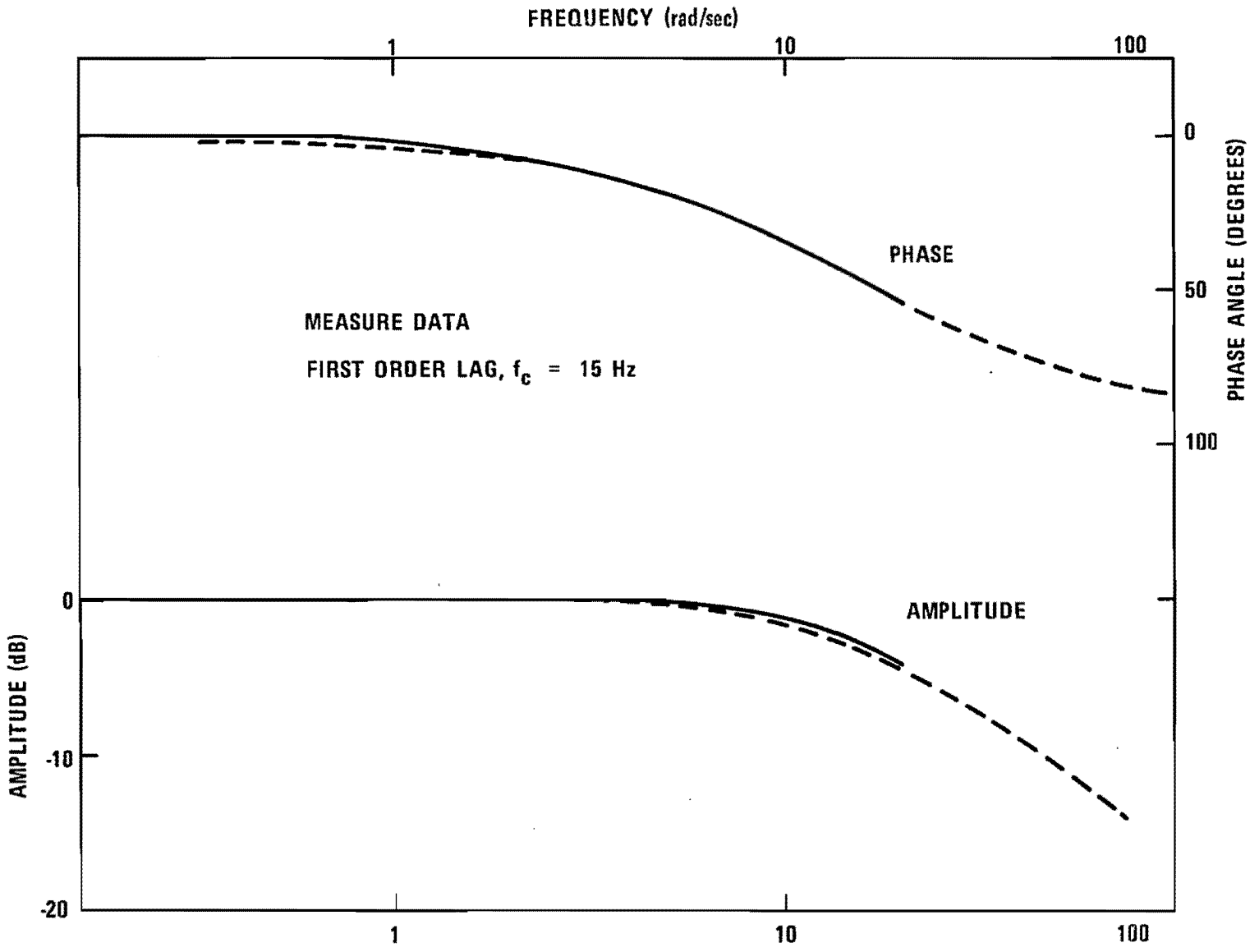

Figure C-3. ECS Pitch Servo Response

TABLE C-2. ECS RATE LIMITS

Amplitude	Rate Limit, cm/sec (in/sec)		
%	Pitch	Roll	Yaw
2.5	7.62 (3.0)	7.62 (3.0)	7.62 (3.0)
5	7.37 (2.9)	7.62 (3.0)	7.62 (3.0)
10	7.11 (2.8)	7.87 (3.1)	7.87 (3.1)

Math Model.-From the foregoing results we conclude that the ECS servo can be represented by a first-order lag with a corner frequency of approximately 15 Hz. This appears to be valid up to a frequency of 20 Hz, the highest frequency investigated. As an illustration, the data from Table C-2 for the pitch servo at 2.5% stroke is plotted in Figure C-3. Also included are the phase and amplitude curves for a true first-order lag with a corner frequency of 15 Hz.

Primary Control System Characteristics

The primary control system evaluated here includes that portion from the output of the ECS servos to the output of the upper boost actuators, which drive the swash plate. Included between these limits are the lower boost actuator and the mechanical linkages and mixers.

It was not possible to conduct frequency response tests on the primary control system in the hangar. This was because the oscillatory motion of the upper boost actuators tended to start the stationary rotor blades bouncing, creating a condition possibly hazardous to blades or personnel. Therefore, frequency response data was only obtainable during flight. However, it

was possible to obtain some data, including nonlinearities, step responses, and rate limits, in the hangar.

Measured Frequency Response.-Frequency response data was recorded in flight on magnetic tape by the on-board instrumentation system. The frequency range investigated was 0.25 to 8 Hz and the amplitude $\pm 10\%$ of ECS stroke, except at the higher frequencies of 4 and 8 Hz, where amplitudes of $\pm 5\%$ and $\pm 2.5\%$ respectively were used to avoid rate limiting in the ECS actuator. The four upper boost actuators were added algebraically according to the formulas given in Figure C-1. This gave the net pitching, rolling, or yawing output from the control system. The digitized data was then subjected to a Fourier analysis program which was able to provide the amplitude and phase shift of the funamental forcing frequency as well as the noise frequency components in the sensor outputs.

Fourier analysis was then used to determine the transfer function of the control system from ECS servo output to the summation of the upper boost actuators on a per-axis basis. The results of this analysis are presented in Table C-3.

Nonlinearities.-Linearity and hysteresis of the primary control system were checked by driving the ECS servo with a 0.1 Hertz triangle wave and recording the ECS servo output and the summation of the upper boost actuator outputs on an X-Y recorder. The proper summations are listed in Figure C-1. These tests were conducted at three ECS servo output amplitudes, $\pm 2.5\%$, $\pm 5\%$, and $\pm 10\%$ of full stroke. The results for the pitch, roll, and yaw axes, respectively, are shown in Figures C-4, C-5, and C-6.

TABLE C-3. CH-47B CONTROL SYSTEM TRANSFER FUNCTION

Flight Condition	Axis	Frequency Hz	ECS Amplitude ± %	Ratio - Delta Boost*/ECS	
				Gain	Phase, Deg.
Hover	Pitch	.5	10	1.56	- 14
		1	10	1.57	- 22
		2	10	1.59	- 37
		4	5	1.67	- 64
		8	2.5	.69	-175
	Roll	.25	10	3.72	- 4
		.5	10	3.76	- 8
		1	10	3.81	- 16
		2	10	4.01	- 27
		4	10	4.11	- 53
		8	2.5	2.77	-132
	Yaw	.25	10	4.75	- 8
		.5	10	5.1	- 12
		1	10	4.44	- 28
		2	10	4.67	- 38
		4	5	4.2	- 78
		8	2.5	1.98	-174
80kt Cruise	Pitch	.5	10	1.52	- 11
		1	10	1.51	- 21
		2	10	1.49	- 35
	Roll	.25	10	3.47	- 4
		.5	10	3.41	- 8
		1	10	3.55	- 18
		2	10	3.68	- 26
	Yaw	.25	10	4.25	- 8
		.5	10	4.25	- 12
		1	10	4.38	- 23
		2	10	4.42	- 44

*Delta pitch = Delta (FS + FP - RP - RS)
Delta roll = Delta (FS - FP + RP - RS)
Delta yaw = Delta (FS - FP - RP + RS)

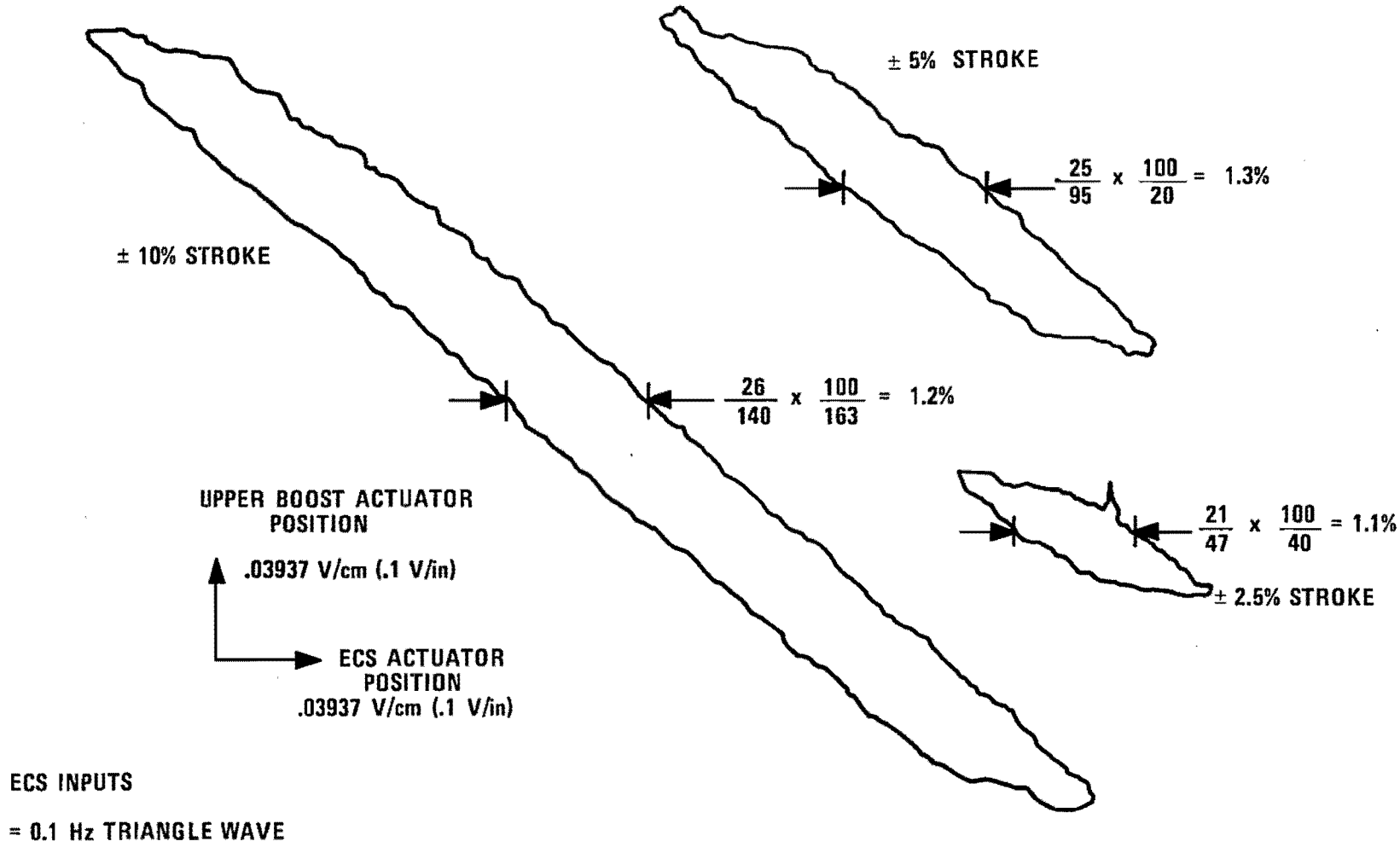

Figure C-4. Pitch Axis Hysteresis

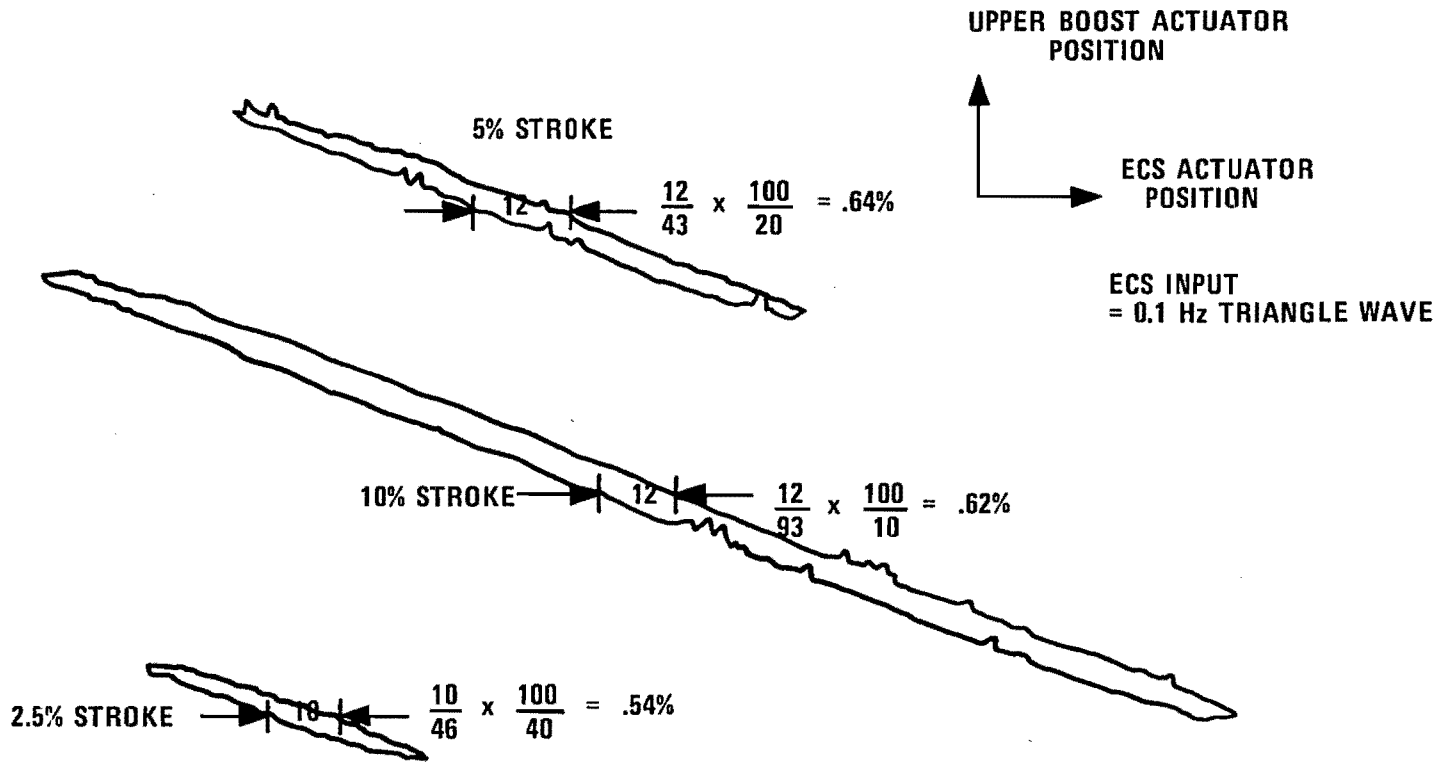

Figure C-5. Roll Axis Hysteresis

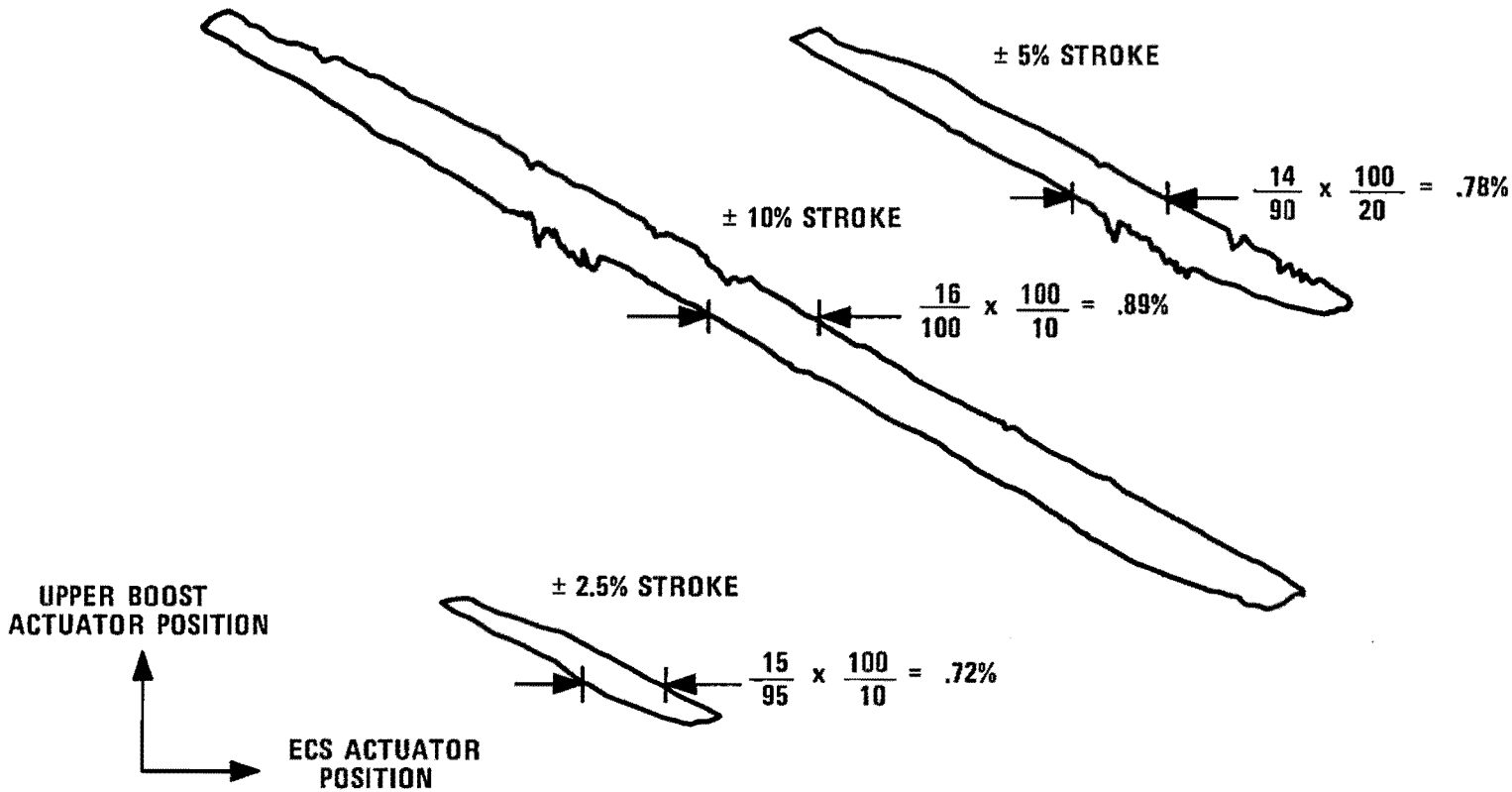

Figure C-6. Yaw Axis Hysteresis

The figures show that there is considerable hysteresis in all three axes, with pitch exhibiting the most. The magnitudes of the hysteresis as a percentage of full ECS servo stroke have been extracted from the figures and listed in Table C-4.

It should be noted that, at least over the range of control system motion induced by ECS servo strokes up to ±10%, the system is quite linear, that is, linear in the sense that the graphs have very little curvature. They were also quite repeatable since several traces of the hysteresis loop fell on top of each other.

To test for control system linearity at positions other than control stick dead center, the roll stick was moved off center about 50% of its travel and the roll hysteresis loop repeated. The results were very close to the results obtained for a zero centered stick.

To check for frequency-dependent effects in the hysteresis loops (for example, spring-dashpot effect), the roll axis tests were repeated using other velocities for the forcing function triangle wave. The frequency of the

TABLE C-4. HYSTERESIS (% of full travel)

ECS Stroke	Pitch	Roll	Yaw
± 2.5%	1.1	.54	.72
± 5.0%	1.3	.64	.78
± 10%	1.4	.62	.89

wave was varied from 1/5 Hz to 1/30 Hz tests. It is concluded, therefore, that the hysteresis is due primarily to simple mechanical backlash or compliance plus friction.

Step Response.-Since no frequency response tests of the control system were possible in the hangar, as explained earlier, a step response measurement of the pitch axis was substituted. A manual transient input was applied to the pitch stick, using an improvised solid stop to control the amplitude. The summation yielding pitch was recorded on the strip chart recorder. The result of this measurement is replotted as the solid curve in Figure C-7. The dashed curve is a plot of a pure second-order lag with a natural frequency of 50 rps and a damping ratio of 0.65. It should be noted that this is very close to the transfer function of the upper boost actuators given in Reference 1. This was 50 rps and damping of 0.55. It also approximates the third-order model obtained by frequency response testing discussed later (and included in the pitch block diagram of Figure C-1).

Rate Limits.-The rate limits of the combined lower boost and upper boost actuators were determined by applying step inputs to the control stick and yaw pedals, one axis at a time, and measuring the resulting upper boost actuator position with time on the strip chart recorder. From the slope of the curve, the maximum rate was calculated. While that was not considered to be a sophisticated measurement, the purpose was to determine the lower and upper boost actuator combination rate compared with the previously determined value of 7.62 cm/s (3 in/s) for the ECS servo. This would determine which element was controlling in terms of rate limiting. The results of this test are tabulated in Table C-5.

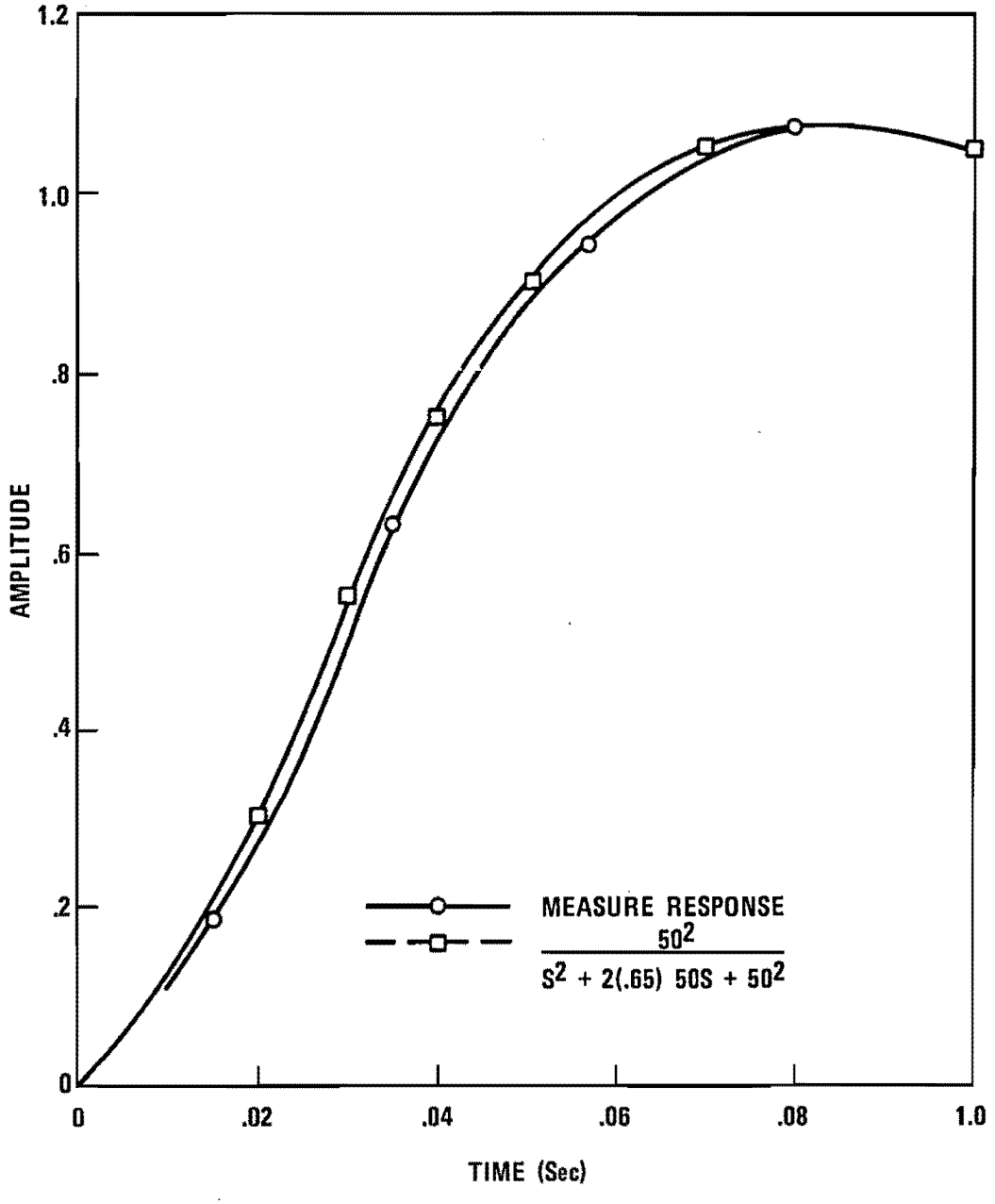

Figure C-7. Pitch Actuator Step Response

TABLE C-5. UPPER BOOST ACTUATOR RATE LIMITS

	Rate Limit, cm/s (in/s)		
	Pitch	Roll	Yaw
At boost output	23.4 (9.2)	71.4 (28.1)	57.9 (22.8)
Equiv. ECS axis	14.0 (5.5)	18.8 (7.4)	11.7 (4.6)

In each case the equivalent ECS servo rate limit of the lower and upper boost actuator combination exceeded the actual ECS rate limit of 7.62 cm/s (3 in/s). Therefore, the ECS servo is the rate limiting element in the system.

Math Model.-From the results of the hysteresis and frequency response tests, a model for the control system was derived in terms of idealized elements.

The hysteresis values determined from the 10% amplitude tests were applied to the 5% and 2.5% amplitudes as well, since the best measurement was obtained at the largest amplitude. Also, from other tests it was known that a second-order lag at approximately 50 rad/sec with damping about 0.6 could be expected. The results of synthesizing the control system with these elements are presented in Table C-6. It was necessary to include a first-order lag at 100 rad/sec to provide a reasonably good match of the recorded data. This must represent the dynamics of the lower boost actuator. In order to provide the best curve fit, the natural frequency and damping ratio of the second-order lag were varied somewhat from axis to axis. No explanation is available for this discrepancy, since the same upper boost

TABLE C-6. CH-47B CONTROL SYSTEM RESPONSE CURVE FITTING (Hover Data)

Freq. Hz	ECS Amp. ±%	Hysteresis Gain	Hysteresis Phase Deg.	Second Order Gain	Second Order Phase Deg.	First Order Gain	First Order Phase Deg.	Total Gain Relative	Total Gain Normalized	Total Phase Deg.	Flight Test Measurement Normalized Gain	Flight Test Measurement Phase Deg.
Pitch		1.4% of	4 inches	Wn = 46 rps	ζ = .45	Wc =	100 rps					
.5	10	.93	-10	1	- 4	1	- 2	.93	1	- 16	1	- 14
1	10	.93	-10	1.01	- 7	1	- 4	.94	1.01	- 21	1	- 22
2	10	.93	-10	1.04	- 15	.99	- 8	.96	1.03	- 33	1.02	- 37
4	5	.83	-20	1.17	- 35	.97	-15	.94	1.01	- 70	1.07	- 64
8	2.5	.47	-40	.99	-102	.89	-27	.41	.44	-171	.44	-175
Roll		.62% of	4 inches	Wn = 50 rps	ζ = .50							
.25	10	.98	- 4	1	- 2	1	- 1	.98	1	- 7	1	- 4
.5	10	.98	- 4	1	- 4	1	- 2	.98	1	- 10	1.01	- 8
1	10	.98	- 4	1.01	- 7	1	- 4	.99	1.01	- 15	1.02	- 16
2	10	.98	- 4	1.03	- 15	.99	- 8	1.0	1.02	- 27	1.08	- 27
4	10	.98	- 4	1.11	- 34	.97	-15	1.06	1.08	- 53	1.1	- 53
8	2.5	.85	-16	1.0	- 90	.89	-27	.75	.77	-133	.74	-132
Yaw		.89% of	4 inches	Wn = 27 rps	ζ = .50							
.25	10	.96	- 6	1	- 2	1	- 1	.96	1	- 9	1	- 8
.5	10	.96	- 6	1	- 5	1	- 2	.96	1	- 13	1.07	- 12
1	10	.96	- 6	1.01	- 10	1	- 4	.97	1.01	- 20	.93	- 28
2	10	.96	- 6	1.05	- 21	.99	- 8	1.0	1.04	- 35	.98	- 38
4	5	.91	-12	1.15	- 51	.97	-15	1.01	1.06	- 78	.88	- 78
8	2.5	.76	-24	.63	-121	.89	-27	.43	.44	-172	.42	-174

actuators enter into the composite axis displacement. If it had been possible to use larger amplitude displacement at the ECS without encountering rate limiting at the higher frequencies, the quality of the data might have been improved. To average the results obtained, it could be said that a second-order lag at 45 rad/sec and 0.5 damping, plus a first-order lag at 100 rad/sec represent the control system between ECS output and total upper boost actuator displacement, excluding hysteresis.

Airframe/Rotor Characteristics

From the recordings of pitch, roll, and yaw rates plus lateral acceleration, a measure of the airframe transfer function can be obtained. With the Fourier analysis also applied to these sensor outputs, an added bonus is the ability to determine the relative amplitudes of noise components at the control frequencies of interest.

Measure Frequency Responses

From the Fourier analysis of the sensor output data, transfer functions were obtained relating the magnitude and phase with respect to the axis summation of the upper boost actuators. This data is presented in Table C-7. Plots of the data are presented in Figures C-8 through C-11. In addition, these plots include the amplitude and phase of the upper boost actuator summations with respect to their ECS servos, taken from Table C-3. It should be noted that there is good agreement between hover and cruise conditions for the upper boost summations with respect to their ECS and also for the body rate sensors up to 2 Hz. Except for the pitch axis, the body rate data above 2 Hz appear to be unreliable. This is undoubtedly due to the high noise content of the

TABLE C-7. AIRFRAME FREQUENCY RESPONSE DATA

Flight Condition	Forcing Freq. Hertz	q Delta Pitch		p Delta Roll		r Delta Roll		Ny Delta Roll		p Delta Yaw		r Delta Yaw		Ny Delta Yaw	
		Gain	Phase	Gain	Phase	Gain	Phase	Gain	Phase	Gain	Phase	Gain	Phase	Gain	Phase
Hover	.25	NR		.138	- 46	.019	- 35	.138	- 45	.009	-232	.033	- 91	.0089	-14
↓	.5	.18	- 76	.093	- 82	.013	- 88	.027	-154	.006	-255	.017	-124	.011	+ 2
	1	.089	- 94	.042	-106	.005	- 99	.016	-198	.003	-269	.006	-110	.0076	-12
	2	.083	-112	.0076	-105	.0018	-245	.0114	-198	.0054	-223	.0023	- 79	.0085	+34
	4	.04	-199	.032	-151	.0115	-450	.049	-308	.018	-309	.015	-124	.15	-21
41.18 m/s	8	.007	-317	.017	-267	.0038	-483	.134	-535	.0093	-547	.0005	-106	.012	- 9
(80 kn)	.25	NR		.137	- 72	.02	- 62	.035	-122	.035	-132	.028	-115	.0061	
Cruise	.5	.141	- 68	.076	- 79	.0075	- 53	.023	-168	.01	-280	.013	-104	.0084	0
↓	1	.095	- 94	.038	-109	.0033	-107	.02	-198	.0037	-325	.0055	-107	.0099	-14
	2	.064	-114	.012	-157	.0019	-175	.011	-230	.0014	-613	.0029	-160	.0135	-39

Gains in radians/sec per inch or g's per inch

Phase in degrees

NR--not run

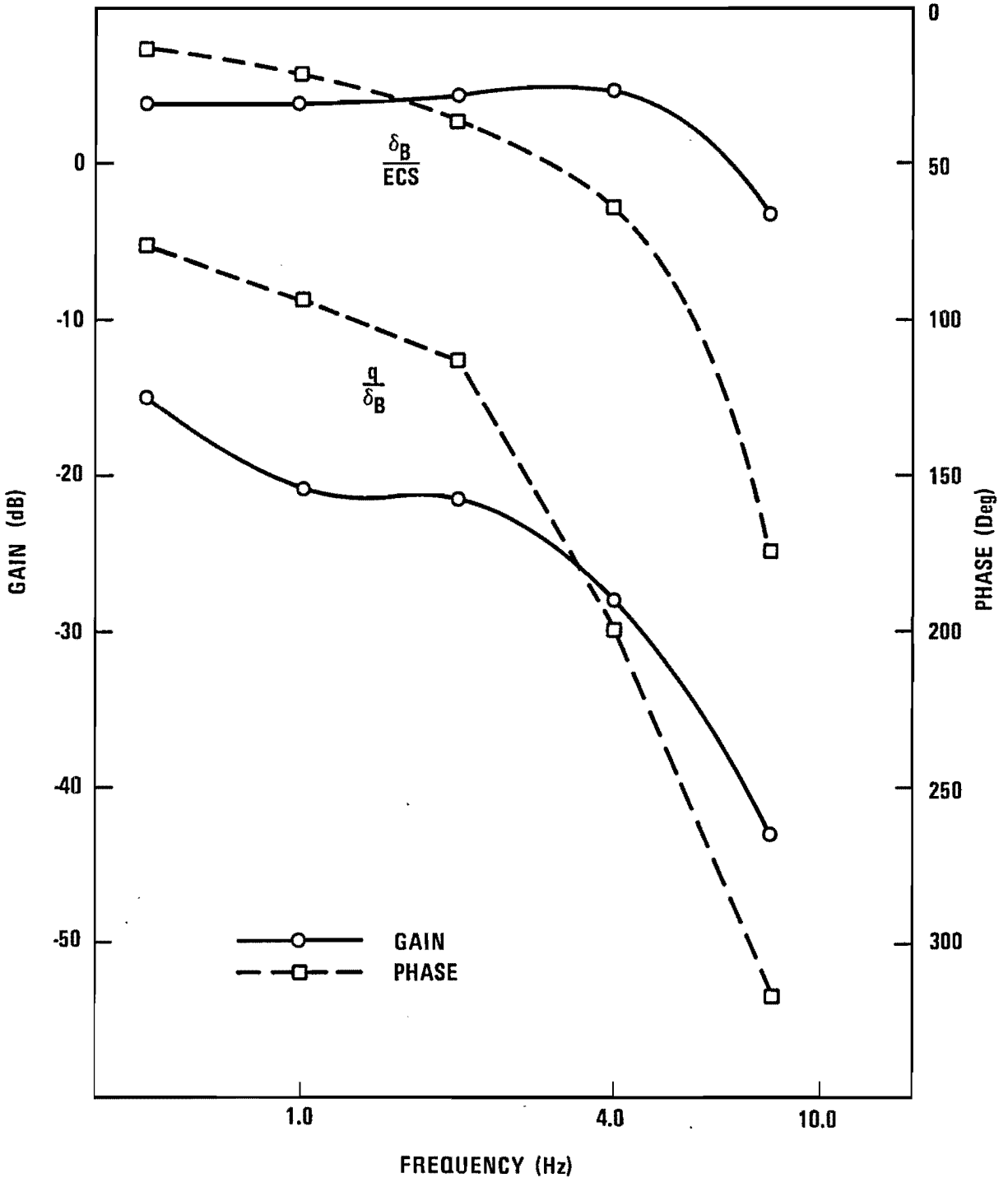

Figure C-8. Pitch Axis Frequency Response (Hover)

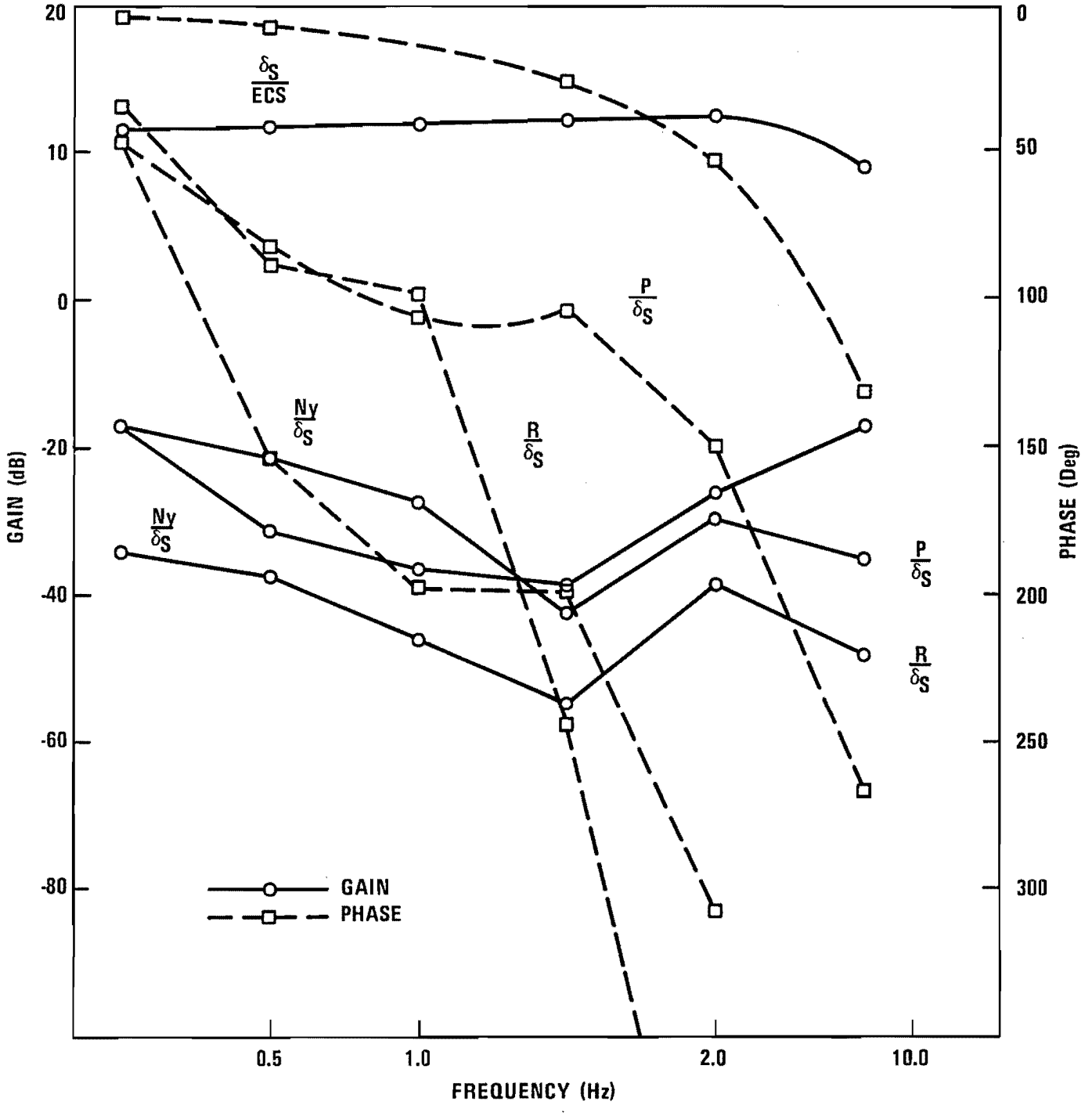

Figure C-9. Roll Axis Frequency Response (Hover)

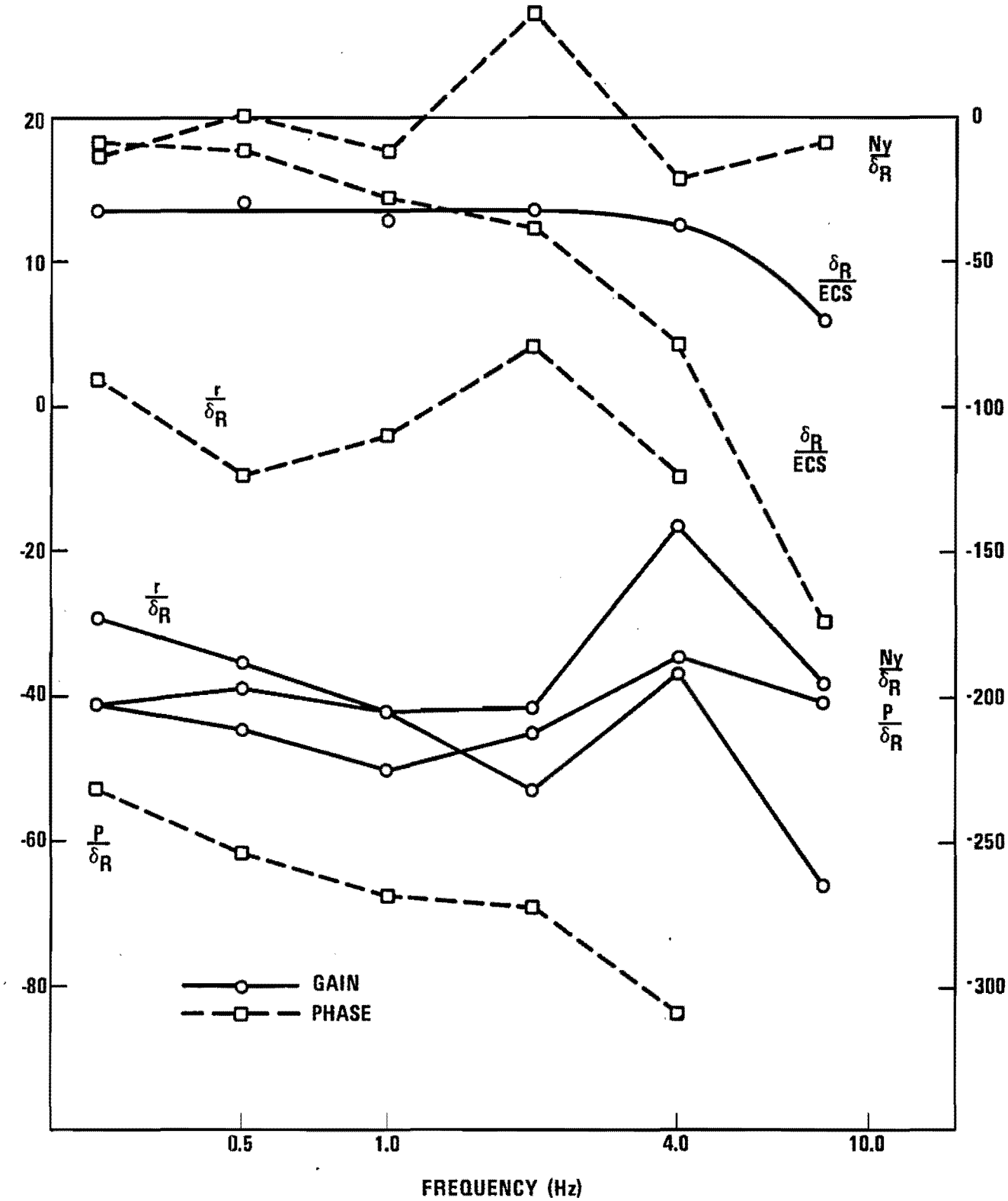

Figure C-10. Yaw Axis Frequency Response (Hover)

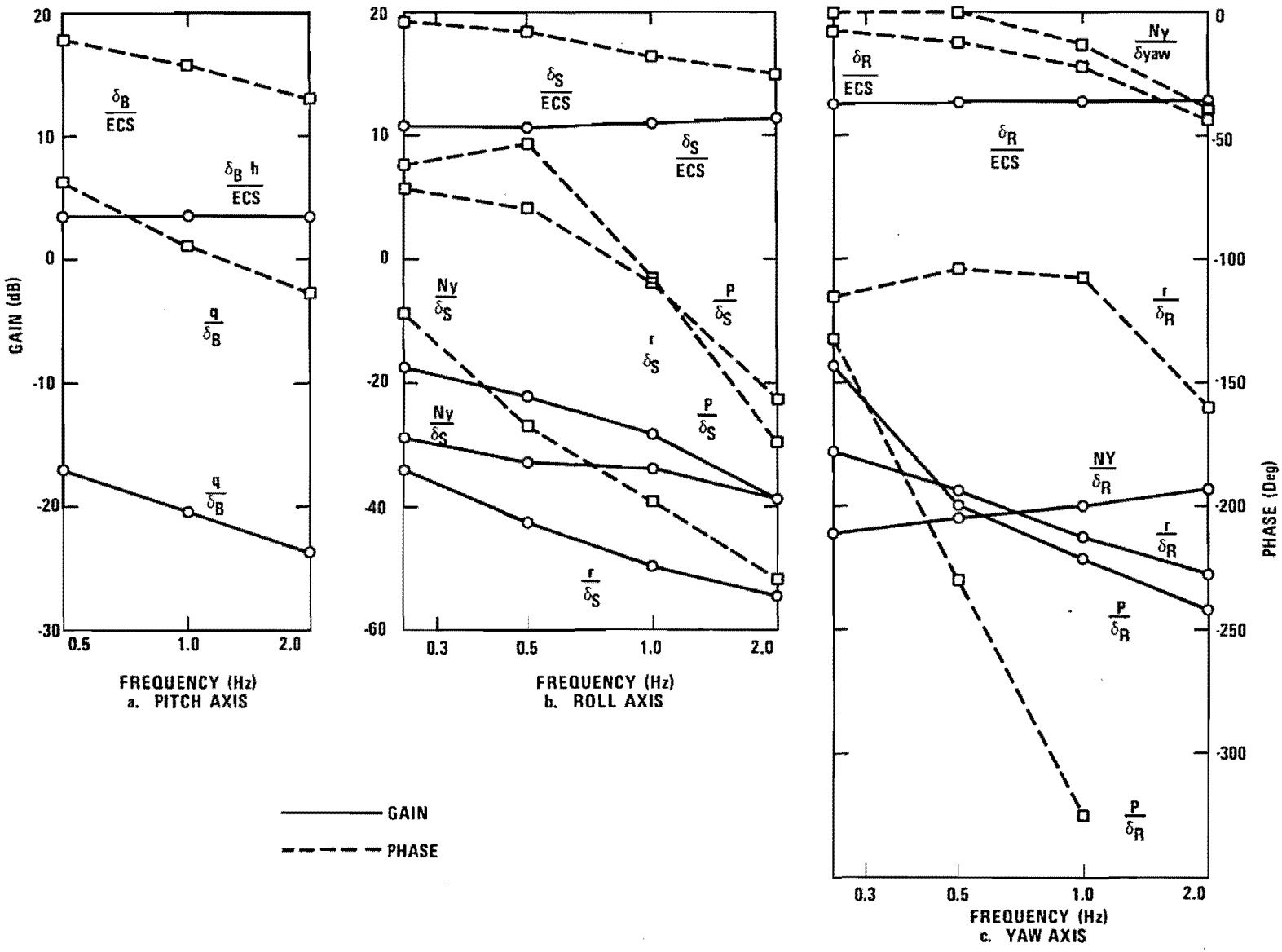

Figure C-11. Frequency Response (Cruise)

sensor outputs at the rotor frequency of 3.75 Hz and multiples thereof, which are close to and influence the data at the forcing frequencies of 4 and 8 Hz. This was not the case in the pitch axis where the pitch rate gyro data follow a more natural trend at 4 and 8 Hz as shown in Figure C-8. Examination of the spectral magnitude plots of the pitch rate gyro output, to be described later, show that the rotor frequency noise is less intense than in the other axes sensors.

It is apparent from the response plots that we would probably have obtained much better data at the higher frequencies if we had chosen forcing frequencies farther away from the known rotor frequencies; in other words, the 4 and 8 Hz values were poor choices.

Sensor Noise Components

The Fourier analysis of the sensor outputs to determine gains and phase shift at the test frequencies also yields all other frequency components present up to and the cut-off frequency used in digitizing the data. This provided an excellent opportunity to assess the absolute magnitudes of the rotor frequency components picked up by the sensors. It has been recognized by various investigators that sensor noise has probably been the limiting factor in obtaining higher gain control loops on this helicopter. Spectrum plots are shown in Figures C-12 through C-15. These all represent the case for a 0.5 Hz forcing frequency into the roll axis, hover condition.

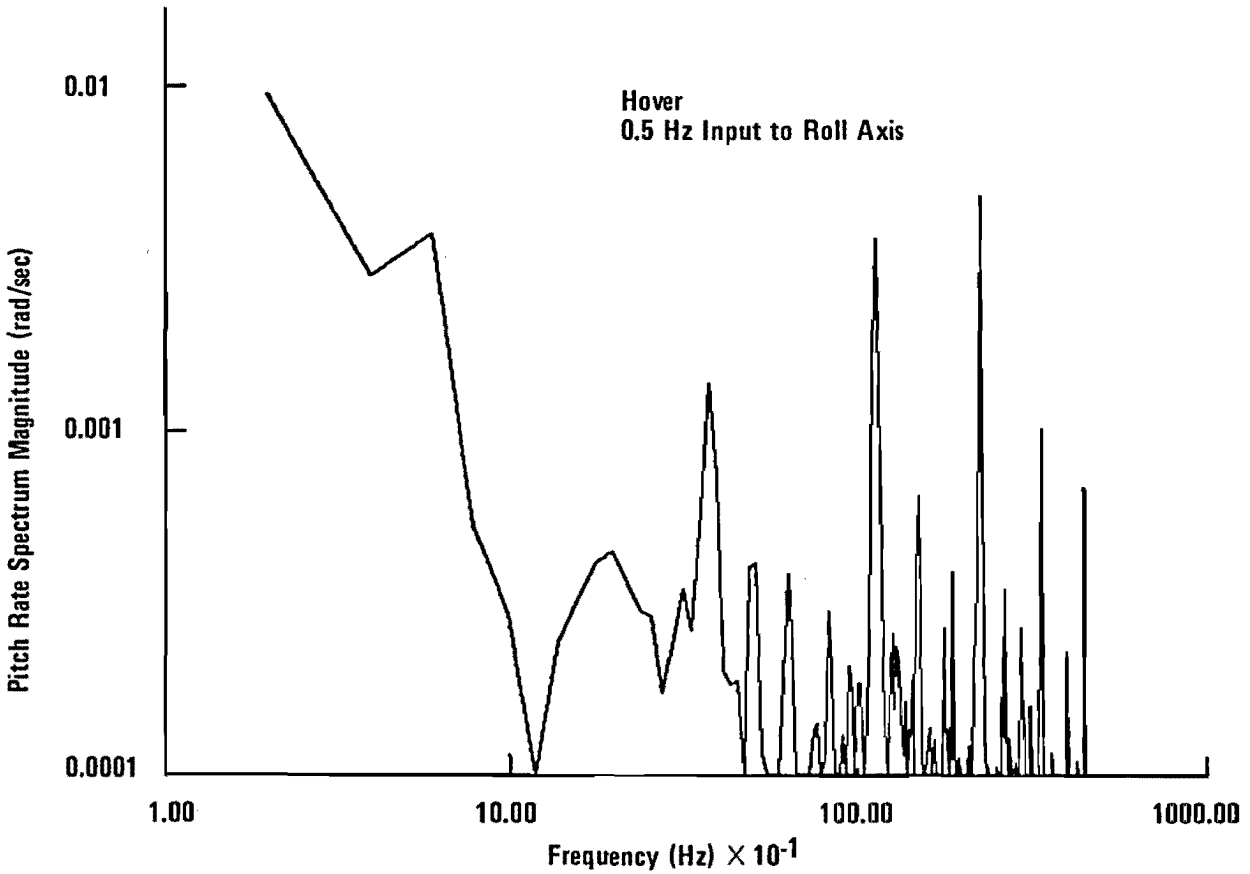

Figure C-12. Pitch Rate Sensor Output Spectrum

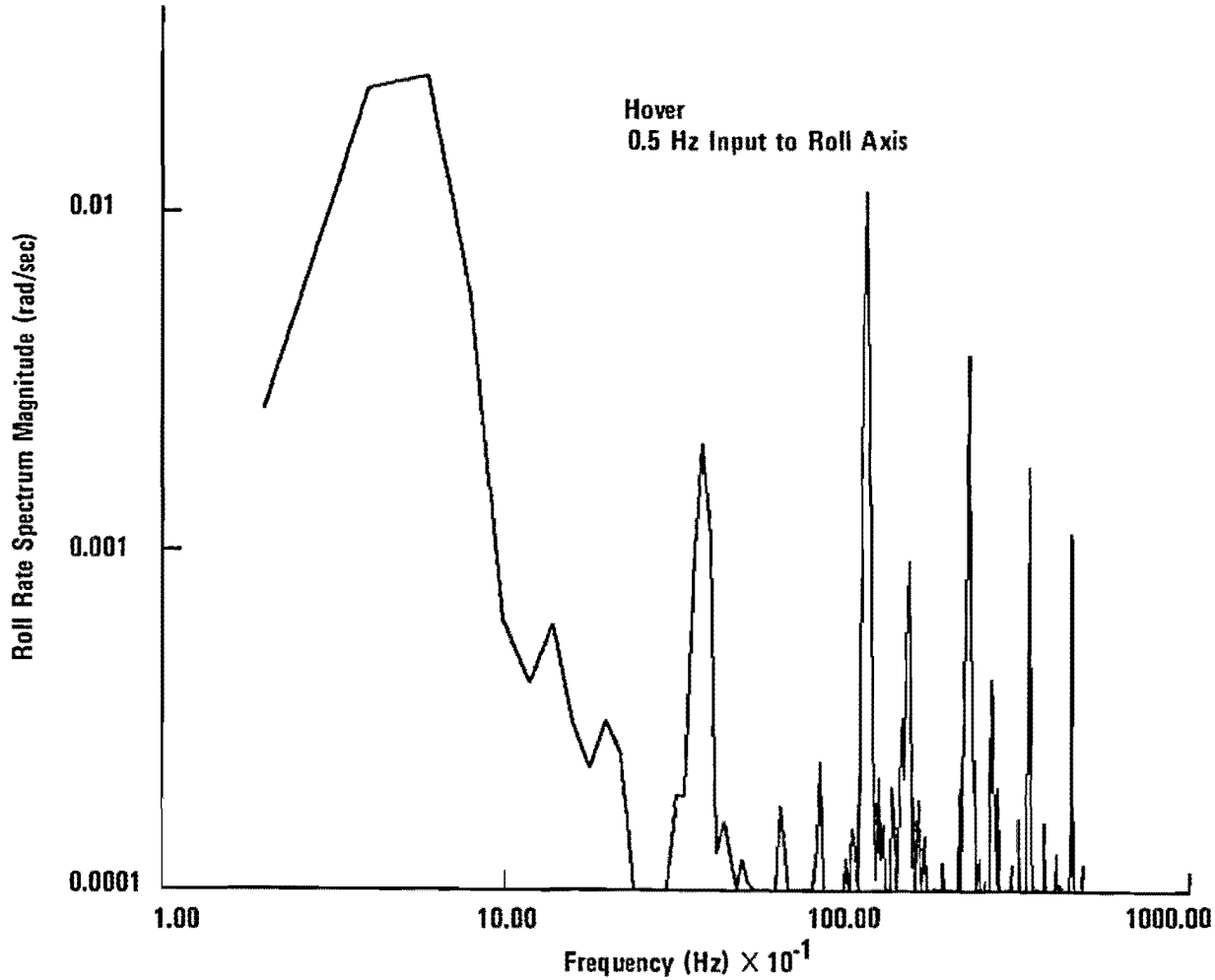

Figure C-13. Roll Rate Sensor Output Spectrum

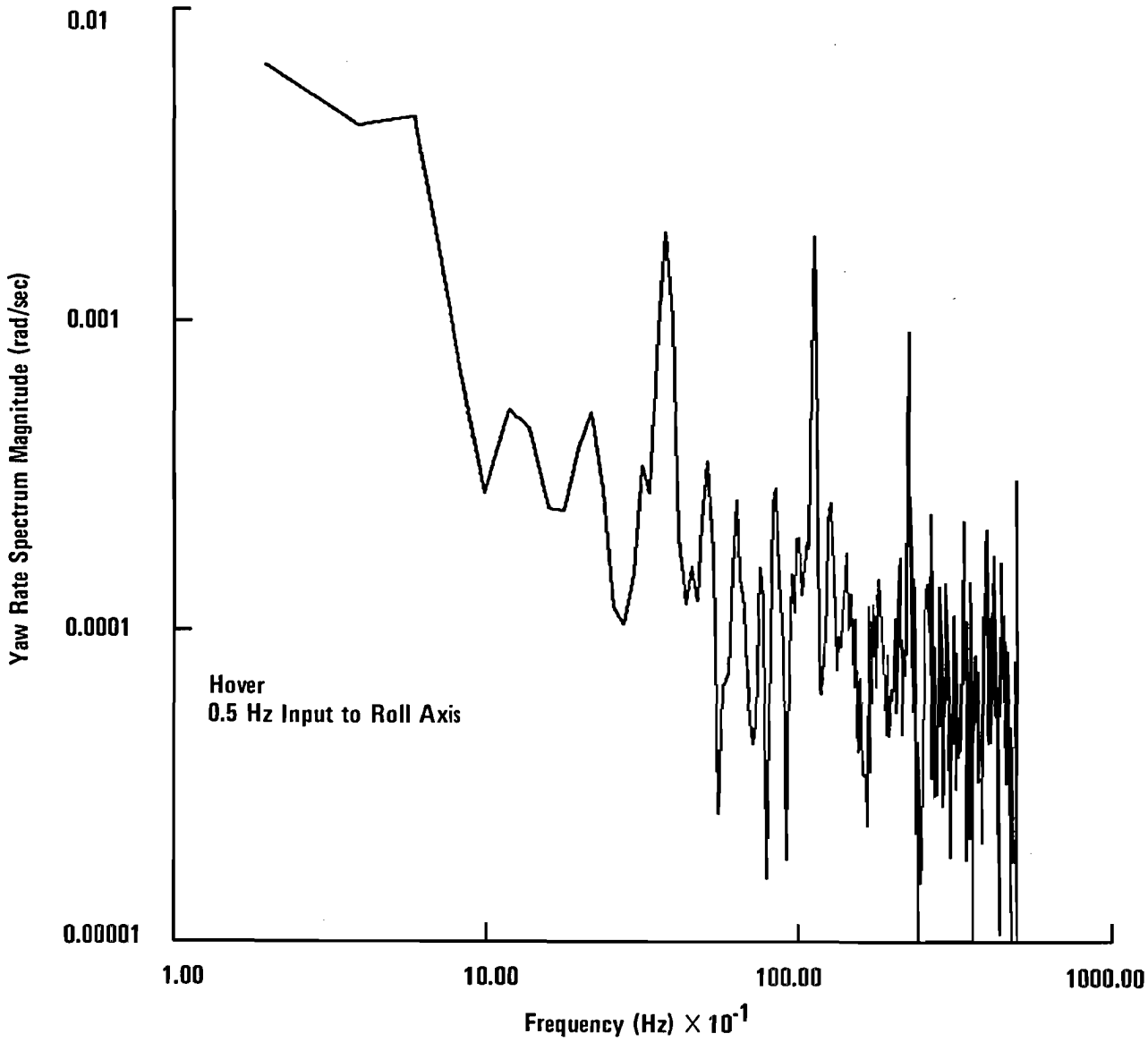

Figure C-14. Yaw Rate Sensor Output Spectrum

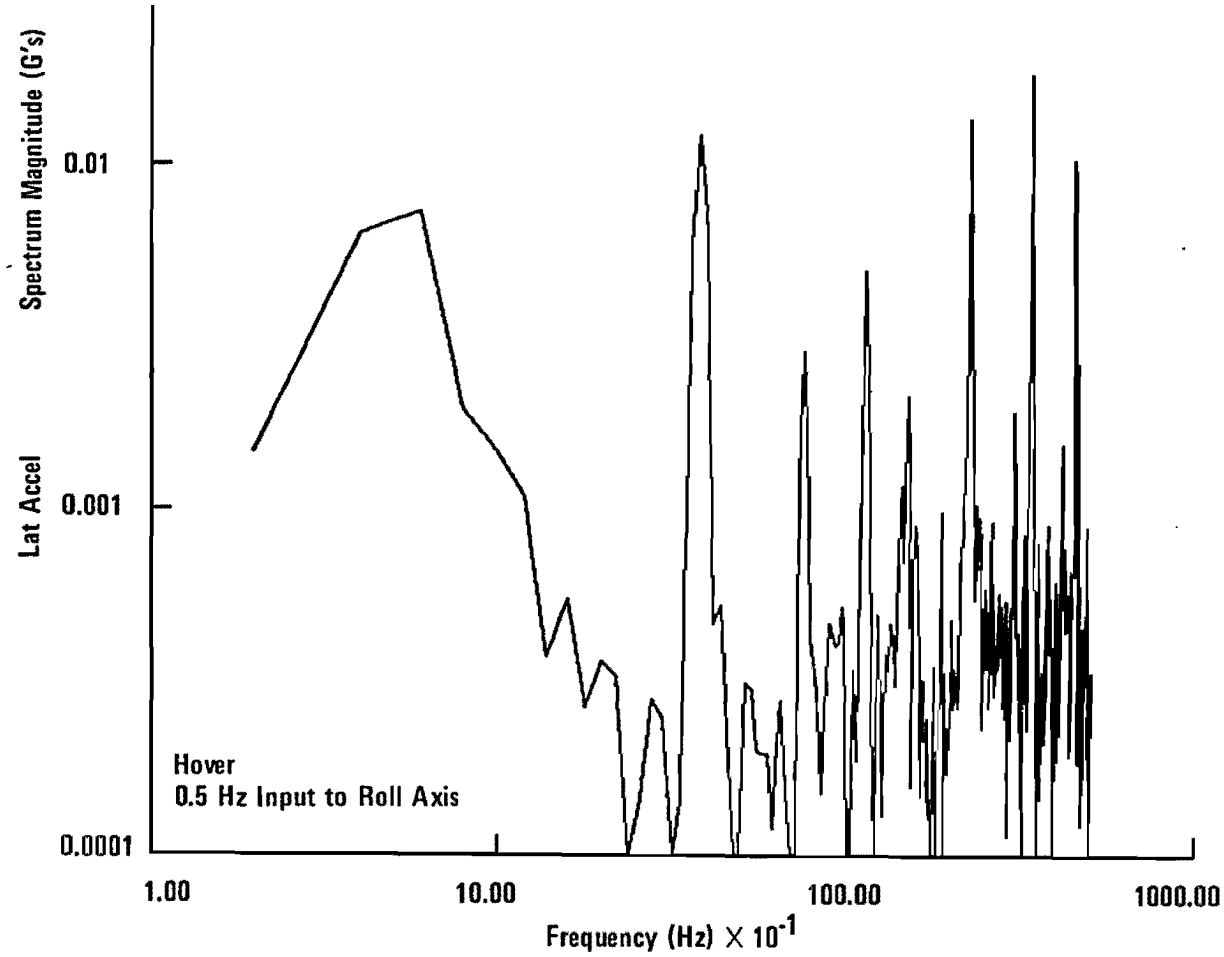

Figure C-15. Lateral Acceleration Sensor Output Spectrum

The four figures represent the pitch, roll, and yaw rate gyro outputs and the lateral accelerometer. It should be noted that the pitch rate is the cleanest of the four signals and the roll rate is probably the noisiest. Also, in some cases, the peaks at frequencies of 3 per rev and 6 per rev exceed those at the fundamental rotor frequency (1 per rev).

REFERENCES

1. Garren, J.F. Jr., Niessen, F.R., Abbott, T.S., and Yenni, K.R., "Application of a Modified Complementary Filtering Technique for Increased Aircraft Control System Frequency Bandwidth in High Vibration Environment," NASA TMX-74004, January 1977.

2. Ostroff, A.J., Downing, D.R., and Rood, W.J., "A Technique Using a Nonlinear Helicopter Model for Determining Trims and Derivatives," NASA TN D-8159, May 1976.

3. Hohenemser, K.H., and Yin, S., "Some Applications of the Method of Multiblade Coordinates, Journal of the American Helicopter Society, Vol. 17, No. 3, July 1972, pp. 3-12.

4. Hall, W. Jr., "Computational Methods for the Synthesis of Rotary-Wing VTOL Aircraft Control Systems," Ph.D Thesis, Stanford University, 1971.

5. "Advanced Flight Control System Concepts for VTOL Aircraft; Phase I Technical Report," R-428, TRECOM 64-50, October 1964.

6. Moore, B.C., " On the Flexibility Offered by State Feedback in Multivariable Systems Beyond Closed Loop Eigenvalue Assignment," IEEE Trans. Auto. Control, Vol. AC-21, No. 5, October 1976, pp. 689-691.

7. Harvey, C.A., Stein, G., and Doyle, J.C., "Optimal Linear Control (Characterization of Multi-Input Systems)", ONR CR 215-238-2, March 1977.

8. Stein, G. and Henke, A.H., "A Design Procedure and Handling Quality Criteria for Lateral-Directional Flight Control Systems," AFFDL-TR-70-152, May 1971.

9. Moore, B.C., "Singular Value Analysis of Linear Systems," University or Toronto, Systems Control Report 7802, July 1978.

10. Hartmann, G.L., et al., "F-8C Adaptive Flight Control Laws," Honeywell Systems and Research Center, 76SRC16, (NASA CR-2880), Minneapolis, Minnesota, June 1976.

11. Hartmann, G.L., and Stein, G., "Digital Adaptive Controllers for VTOL Vehicles," NASA NAS1-14921, March 1979.